UNIVERSITY OF MINNESOTA

This is to certify that I have examined this copy of a doctoral dissertation by

Sujeewa Terasita Kumaratunga

and have found that it is complete and satisfactory in all respects,
and that any and all revisions required by the final
examining committee have been made.

Keith Ruddick

Name of Faculty Adviser

Signature of Faculty Adviser

Date

GRADUATE SCHOOL

Studying Neutrino Oscillations Using Quasi-Elastic Events in MINOS

A DISSERTATION
SUBMITTED TO THE FACULTY OF THE GRADUATE SCHOOL
OF THE UNIVERSITY OF MINNESOTA
BY

Sujeewa Terasita Kumaratunga

IN PARTIAL FULFILLMENT OF THE REQUIREMENTS
FOR THE DEGREE OF
DOCTOR OF PHILOSOPHY

Adviser: Keith Ruddick

February, 2008

Acknowledgments

We are what we are because of the people we met.

My adviser, Prof. Keith Ruddick, you were sometimes a teacher, sometimes a friend but always a role model. At a time when people worry about the lack of role models for women in physics, you broke any such gender barrier to set an example to me. Till the very end, you stunned me with the simplicity with which you attacked seemingly big problems and your ability to do statistical calculations in your head. You knew exactly when to push and when to pull me. Thank you for being such a wonderful mentor in physics and in life, much to the envy of my friends!

This thesis would not have been a possibility if it wasn't for the unofficial co-advising role Minnesota post-doc David Petyt took upon himself. From initially suggesting a thesis topic to sometimes pouring through my code, your invaluable advice made my time as a graduate student so much shorter. Later on as I frantically wrote off chapter after chapter of this manuscript, you were always there for moral support. Thank you for saving me from Austin!

I have always had the good fortune of having wonderful co-workers. But the Minnesota MINOS grad students still stand out from the rest. Doctors Erik Beall, Bernie Becker, Dipu Rahman, Ben Speakman, Aaron McGowan and Jeremy Gogos, thank you for going before me and showing me the way. Ben, you taught me the tools of computing like it was your job to do so, I know it wasn't. Dipu, thanks for introducing me to salsa. Jeremy, thank you for volunteering to teach me to run

atmospheric Monte Carlo when no one else would, for checking on me after I had driven four drunk Minoans from Virginia to Ely, but most of all for never letting me forget how to laugh hysterically; I am at my best when I am happiest! Eric, it was fun sharing an office with the only normal person in 243. Thank you guys for putting up with my many quirks, like zero tolerance for mice! Wherever I may end up, I ask only that I work with people as fun as you were!

Other Minnesota post-docs, Leon Mualem, Sue Kasahara and Kregg Arms, thanks for all your help. Leon, you helped me take my very first steps in MINOS, C++ and Linux. Sue, thanks for patiently explaining the complexities of C++ many times.

The MINOS collaboration, the mine crew in Soudan, Bill, Jerry, Curt, Doug, Brian, Jack and Eileen, I will certainly miss being picked on. Deb and Bill thanks for feeding me whenever I was up there and for being such wonderful hosts to me and my sister.

My teachers in Minnesota, Professors Chuck Campbell, Ron Poling, Mikhail Voloshin, Arkady Vainshtein, Michael DuVernois, Peter Litchfield, I appreciate you spending so much time helping me to understand things. Prof. Voloshin, despite being an amazing theorist, you came down to our level to teach us complicated calculations using basic physics principles - your class was the one that I most looked forward to, here in Minnesota.

The physics department in Minnesota was my home away from home; no, actually it was my home! My first friends: my classmates, Fang Fang, Bei Cai, Yaroslav Lutsyshyn, Byoungsoon Lee, Dat Nguyen, Masaya Nishioka, Hyuk-Jae Jang, Alexander Scott, just to name a few - I am most grateful for the cultural diversity and awareness you brought in to my life. Fang and Bei, it is nice to still be in touch with former office mates. Yaroslav, you are still the biggest fan of my pictures and thanks for teaching me Poisson statistics and the “two-move checkmate”.

Dat, almost two years after you've left, I still miss you. Other physics grad students that I crossed paths with: Alexey, too bad you made a New Year's resolution not to play chess just when I have all the time in the world and a brand new chess set for that. Kostik, thank you for letting me rant on anything and everything and just totally taking my side - you spoiled me like that. Longhua and Kaiyan I appreiciated the way you immediately stopped everything you were doing and helped me make sudden travel plans to China. Maribel, you saw me in more of a positive light than I saw myself sometimes; it helped me out so much at those times! Jun, Laura, Angela, it was fun knowing you. I was never alone in this new country, because of you all!

The few hours spent away from school were made pleasant by my landlord and housemate turned friend for six years now, Patty Seflow. You have influenced my life in more ways than you could ever imagine. Thank you for helping me relax and let go. Sandee thanks for feeding me so many times with your exotic cuisine!

In so many ways my pre-grad school years prepared me for the grueling task of going to physics grad school in a new country. Particular thanks to my first science teacher, Ms. Sagarika Seneviratne for never discouraging me even when I asked difficult questions, to my math teacher, Ms. Neela Ratnayake, for despite being a phenomenal teacher, still letting me go ahead of the rest of the class, learn things myself and do problems my way, and correcting them, even though they employed unpolished long and winding methods. To this day I think you get credit for whatever self learning abilities I've got. Dr. Upali Karunasiri, thank you for actually enjoying teaching me - you were my inspiration to come to grad school.

Many friends in Good Shepherd Convent Kandy, Kandy Girls' High School, Ernst & Young, University of Peradeniya and Virtusa Inc. - I have very fond memories of the good times. Nalaka, you were a good friend in college.

Last but not the least, thank you to my family, Jerry and Therese Fernando,

Waruni and Dinesh Kumaratunga; Januka Attanayake, part of our family for all I know, thank you for at least pretending to follow in my footsteps! Thaththi, you taught me the simple pleasures of life: chess continues to be my second favourite diversion from work, after day dreaming. Ammi, I am yet to see someone as persevering as you. Thank you for your tireless efforts to give us what you didn't have. Didi, we've grown to be good friends over the years. It's fun to have a sister who I can share all the details of my embarrassing moments with; even though, I think your embarrassing moments are way worse than mine! Malli, my longest lasting best friend, you can still be a pain sometimes. But I'll live with that; you are the one person I can share life's deepest secrets with, without being judged! You've taught me so much just by listening and not saying a word. I feel blessed to have siblings like you two! No one really knows my quirks like you two do, and yet you continue to not denounce me; thank you!

To Stephie:

Long after you left us, your memories still continue to teach me life's little lessons.

"Would you tell me, please, which way I ought to go from here?"

"That depends a good deal on where you want to get to," said the Cat.

"I don't much care where – " said Alice.

"Then it doesn't matter which way you go," said the Cat.

" – so long as I get *somewhere*," Alice added as an explanation.

"Oh, you're sure to do that," said the Cat, "if you only walk long enough."

- Lewis Carroll, Alice's Adventures in Wonderland

Studying Neutrino Oscillations Using Quasi-Elastic Events in MINOS

by Sujeewa Terasita Kumaratunga

ABSTRACT

MINOS (Main Injector Neutrino Oscillation Search), is a long baseline neutrino experiment designed to search for neutrino oscillations using two detectors at Fermi National Accelerator Laboratory, IL (Near Detector) and Soudan, MN (Far Detector). It will study $\nu_\mu \rightarrow \nu_\tau$ oscillations and make a measurement on the oscillation parameters, Δm^2_{23} and $\sin^2 2\theta_{23}$, via a ν_μ beam made at Fermilab.

Charge current neutrino interactions in the MINOS detectors are of three types: quasi-elastic scattering (QEL), resonance scattering (RES) and deep inelastic scattering (DIS). Of these, quasi-elastic scattering leaves the cleanest signal with just one μ and one proton in the final state, thus rendering the reconstruction of the neutrino energy more accurate. This thesis will outline a method to separate QEL events from the others in the two detectors and perform a calculation of Δm^2_{23} and $\sin^2 2\theta_{23}$ using those events.

The period under consideration was May 2005 to February 2006. The number of observed quasi-elastic events with energies below 10 GeV was 29, where the expected number was 60 ± 3. A fit to the energy distribution of these events gives $\Delta m^2_{23} = 2.91^{+0.49}_{-0.53}(stat)^{+0.08}_{-0.09}(sys) \times 10^{-3}\ eV^2$ and $\sin^2 2\theta_{23} = 0.990_{-0.180}(stat)_{-0.030}(sys)$.

Contents

List of Tables

List of Figures

Chapter 1

Introduction

Neutrinos are the smallest of fundamental particles and are of three different flavors. Past experiments have shown neutrinos oscillate between these three flavor states. This thesis will describe an experiment, Main Injector Neutrino Oscillation Search (MINOS), to measure parameters of neutrino oscillations.

When neutrinos interact with matter, they do so in two ways, depending on whether charge is exchanged or not. The Feynman diagrams for these two interactions are shown in Figure 1.1:

- Charged Current (CC) interactions in which the neutrino interacts with a nucleon (N) and produces a charged lepton, i.e., $\nu_x + N \rightarrow X + hadrons$, where ν_x denotes the three different flavors of neutrinos and X denotes their corresponding charged leptons.
- Neutral Current (NC) interactions in which the neutrino scatters off a nucleon, i.e., $\nu_x + N \rightarrow \nu_x + hadrons$.

The charged current interactions readily identify the corresponding neutrino flavor, because these lepton number conserving weak interactions are such that ν_e, ν_μ or ν_τ interacting via a charged current reaction produce an e, μ or τ respectively.

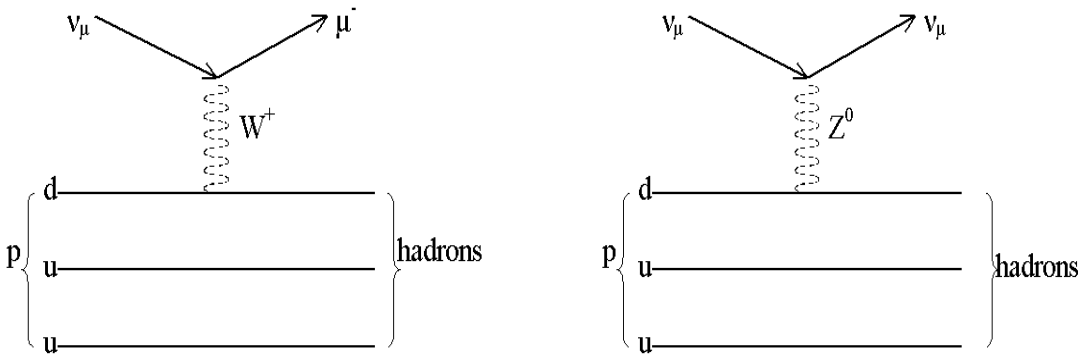

Charged current events Neutral current events

Figure 1.1: Feynman diagrams for neutrino interaction with matter

1.1 Neutrino Charged Current Interactions in MINOS

The CC interactions provide the main signature for the MINOS oscillation analysis. Neutrino-nucleon CC interactions are of three types -

1. Quasi Elastic Scattering (QEL) : $\nu_\mu + n \rightarrow \mu^- + p$

2. Resonance Scattering (RES) : $\nu_\mu + N \rightarrow \mu^- + Resonance \rightarrow N' + m\pi$, where $N \equiv n, p$; $Resonance \equiv \Delta^+, \Delta^{++}$; $m \equiv 1, 2, 3, ...$; and $\pi \equiv \pi^\pm, \pi^0$

3. Deep Inelastic Scattering (DIS) : $\nu_\mu + N \rightarrow \mu^- + X$, where X is a collection of particles resulting from the neutrino inelastically scattering off the nucleus.

The total CC cross section and the contribution from each of the above processes are shown in Figure 1.2.

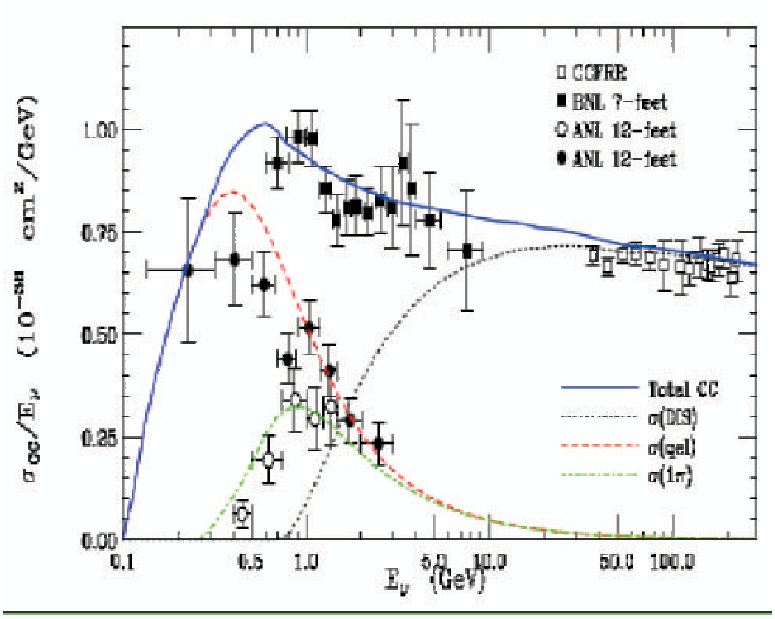

Figure 1.2: Neutrino-nucleon cross section decompositions

The analysis presented in this thesis is based on the separation of QEL events and using those to determine the oscillation parameters.

1.1.1 Why choose Quasi Elastically Scattered Events?

- **Better Reconstruction of Neutrino Energy :** Out of the three types of CC interactions, QEL scattering is the simplest process, giving just a muon and a proton as final state particles. This clean signature makes QEL events readily identifiable and the parent neutrino energy is easily reconstructed as described in Section 4.

- **Dominant Process at Critical Neutrino Energy :** According to our current knowledge in neutrino oscillations, for the MINOS experiment, the probability of ν_μ's oscillating into some other flavor (like ν_e or ν_τ) is maximized at a neutrino energy of $1.0 - 2.0\ GeV$. As can be seen from Figure 1.2, QEL

scattering is the dominant process at this energy.

Throughout the thesis I will use natural units, where $c = \hbar = 1$. So, units of momentum which are normally GeV/c will be written as GeV instead.

Chapter 2

Neutrino Oscillations, an Introduction

2.1 History of Neutrinos

In the 1920's the study of nuclear beta decay brought forth some unanswered questions in physics. In such a decay a radioactive nucleus, A, is transformed into a slightly lighter nucleus, B, with an extra positive charge and an electron, e.

$$A \rightarrow B^{+} + e^{-} \tag{2.1}$$

Provided that the decaying parent nucleus is at rest, the electron's energy, E, should be a constant dependent only on the masses,m_A, m_B and m_e, of A, B and e respectively:

$$E = \frac{m_A^2 - m_B^2 + m_e^2}{2m_A}c^2 \tag{2.2}$$

But experiments by Ellis, Chadwick [1] and others established that the emitted electron had a continuous energy spectrum, with the maximum energy given by

equation 2.2. This implied that some energy was lost or not visible. Attempts to trap this lost energy failed.

In 1934 Pauli first hypothesized a neutral particle to account for this non-conservation of energy and momentum in nuclear beta decay. This particle would be emitted simultaneously with the electron; but, it only interacted weakly, and thus would not leave a direct signal in the detectors.

$$n \rightarrow p + e^{-} + \bar{\nu} \tag{2.3}$$

The next year Fermi developed a quantitative theory of radioactive decays[2], into which he incorporated Pauli's neutral particle and called it the neutrino. Closer studies of the energy spectrum from beta decay showed that the neutrino must have a mass of no more than $\frac{1}{500}$ of the rest mass of an electron.

This theory required that the neutrino carry not only the missing energy and linear momentum from the nuclear beta decay process but also angular momentum. Since the neutron, proton and beta particle all carry half integer spin, it was necessary that the neutrino be assigned a spin of $\frac{1}{2}$ as well.

The very nature of the neutrino that explained beta decay, its ability to carry off energy and momentum without being detected, limited the observation of it. But in the 1950's Cowan and Reines et al. studied fission reactor neutrinos incident on a detector containing cadmium loaded liquid scintillator [3], resulting in the inverse beta decay reaction:

$$\bar{\nu} + p \rightarrow n + e^{+} \tag{2.4}$$

The positron emitted in this reaction quickly annihilated with an electron producing two 0.51 MeV gamma rays. The neutron, after some drifting was captured by cadmium giving out a multiple gamma ray burst. These two spatially separated

signals along together with other controls on the number of target protons, background etc., served as the first discovery of the neutrino for which Reines received the Nobel Prize in 1995.

2.2 Neutrinos in the Standard Model

Studies of Z^0 decays in LEP have shown that there are just three species of neutrinos [4]. After the discovery of the ν_e in 1956 by Reines and Cowan [3], the ν_μ was discovered in 1962 by Lederman, Schwartz, Steinberger et al [5] and finally the ν_τ was discovered by the DONUT collaboration in 2000 [6].

The Standard Model, the current hypothesis for fundamental particles and their interactions, incorporates these three uncharged neutrinos and their charged partners, e, μ and τ, which are collectively known as leptons, in three families of matter. The constituents of the Standard Model are shown in Figure 2.1.

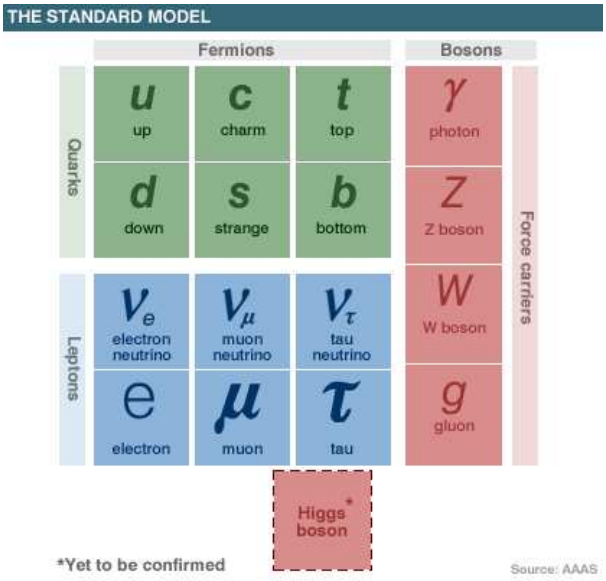

Figure 2.1: Constituents of the Standard Model in Particle Physics

Accordingly, the beta decay process (Equation 2.3) and the reaction that Reines and Cowan studied (Equation 2.4) were correctly, $n \rightarrow p+e^{-}+\bar{\nu_e}$ and $\bar{\nu_e}+p \rightarrow n+e^{+}$ respectively. The subscripts in the neutrinos define the neutrino flavor in these lepton number conserving weak interactions.

Given the reaction 2.4, the reaction $\nu_e + n \rightarrow p + e^{-}$ must also occur. But it was expected that neutrinos and anti-neutrinos were identical, since they were neutral. Then by virtue of replacing the ν_e with the $\bar{\nu_e}$, the inverse beta decay reaction, $\bar{\nu_e} + n \rightarrow p + e^{-}$ should also occur. But Davis found that this reaction did not occur, thus establishing that the neutrino and anti-neutrino are two distinct particles. The neutrinos differ from their anti neutrinos in helicity, the former being left-handed and the latter being right-handed.

The Standard Model incorporates neutrinos as zero-mass particles. These participate only in weak and gravitational interactions.

2.3 Neutrino Anomalies

2.3.1 Solar Neutrino Problem

The reaction that is responsible for the luminosity of the sun also produces neutrinos. Several processes that are also part of the proton-proton chain reaction or the Carbon, Nitrogen, Oxygen cycle, contribute solar neutrinos:

$$p + p \rightarrow e^{+} + \nu_e + d \tag{2.5}$$

$${}^{7}_{4}Be + e^{-} \rightarrow \nu_e + {}^{7}_{3}Li \tag{2.6}$$

$${}^{14}_{7}N \rightarrow {}^{14}_{6}C + e^{+} + \nu_e \tag{2.7}$$

$${}^{15}_{8}O \rightarrow {}^{15}_{7}N + e^{+} + \nu_e \tag{2.8}$$

$$^{8}_{5}B \rightarrow ^{8}_{4} B + e^{+} + \nu_e \tag{2.9}$$

The solar neutrino flux composition by channel, is shown in Figure 2.2.

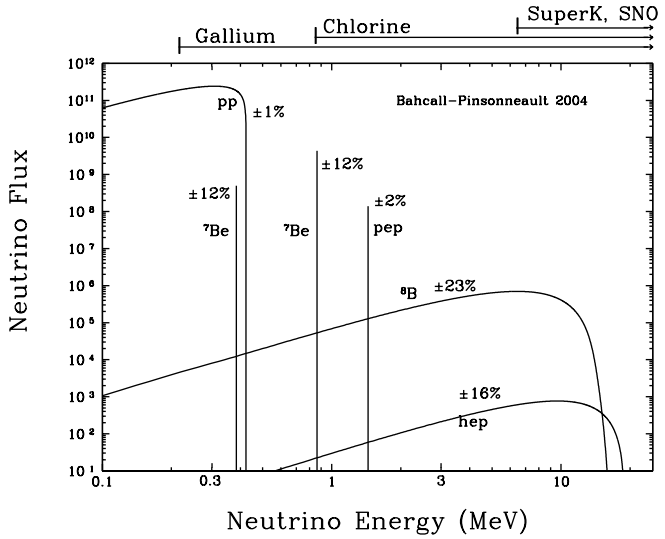

Figure 2.2: Standard Solar Model (SSM) predicted Neutrino Energy Flux. For continuum sources, the neutrino fluxes are given in number of neutrinos $cm^{-2}s^{-1}MeV^{-1}$ at the Earth's surface. For line sources, the units are number of neutrinos $cm^{-2}s^{-1}$. The difficult-to-detect CNO neutrino fluxes have been omitted.

Out of the neutrinos produced by these channels, the $^{8}_{5}B$ solar neutrinos, ν_e's, from reaction 2.9 have sufficient energy to interact with the $^{37}_{17}Cl$ and excite it into $^{37}_{18}Ar$:

$$\nu_e + ^{37}_{17} Cl \rightarrow ^{37}_{18} Ar + e^{-} \tag{2.10}$$

In 1968, Davis[7] used this knowledge together with a neutrino detection technique proposed by Pontecorvo[8] to study solar neutrinos from reaction 2.10. The detector used by Davis was a tank of 3.9×10^5 litres of liquid perchloroethylene (C_2Cl_4), a commonly used dry-cleaning chemical. It was placed $\sim 1600m$ under-

ground in the Homestake mine, so as to shield it from cosmic rays.

The rate of ${}^{37}_{18}Ar$ production in reaction 2.10 as predicted by solar models was $6.0 \pm 1.5 SNU$, but Davis measured only $2.2 \pm 0.4 SNU$ (about one neutrino a day), where $1 SNU = 10^{-36}$ neutrino captures per second per target nucleus [7].

This observation of only approximately one third of the neutrinos predicted by the solar model, implied several possible explanations:

1. Current solar models were wrong, in that they were overestimating the production of ${}^{8}_{5}B$ solar neutrinos.

2. The non-zero magnetic moment of the electron neutrino interacted with the sun's magnetic field to yield right handed neutrinos that did not interact weakly and were thus undetectable by neutrino oscillation experiments [9].

3. The core of the sun was burning at fluctuating temperatures and ${}^{8}_{5}B$ production is sensitive to temperature. Davis's experiment might have been done during a cold phase of the sun.

4. Neutrinos might be oscillating, giving rise to neutrinos changing to something other than the ν_e's that Davis was looking for. This explanation first suggested by Pontecorvo[10], requires that neutrinos have mass.

Several subsequent experiments like GALLEX and Kamiokande revealed the flux of electron neutrinos from the sun to be about 40% lower than that predicted by the Standard Solar Model, but, it was the Sudbury Neutrino Observatory (SNO)[12] that was able to give a definite explanation to this phenomenon in 2001. SNO, a 1000 metric ton heavy water imaging Čerenkov detector was designed to detect the following processes:

$$\nu_e + d \rightarrow p + p + e^- \quad (CC) \tag{2.11}$$

$$\nu_x + d \rightarrow p + n + \nu_x \quad (NC) \tag{2.12}$$

$$\nu_x + e^- \rightarrow \nu_x + e^- \quad (ES) \tag{2.13}$$

For ^8_5B solar neutrino energies (typically $10MeV$), the charged current (CC) reaction 2.11 occurs exclusively for the ν_e's. The neutral current (NC) reaction 2.12 is equally sensitive to all three neutrinos flavors in the Standard Model, ν_e, ν_μ and ν_τ. The elastic scattering (ES) process 2.13, while being sensitive to all three flavors, is more sensitive to ν_e's, because the ν_e ES has both charged and neutral current components. The ν_e flux measured by the CC reaction was $\phi_{CC} = 1.76^{+0.05}_{-0.05} \times 10^6 cm^{-2} s^{-1}$ [13], i.e., $\frac{1}{3}$ of the total Standard Solar Model (SSM) predicted ^8B chain (reaction 2.9) solar ν_e flux of $\phi_{SSM} = 5.05^{+1.01}_{-0.81} \times 10^6 cm^{-2} s^{-1}$ [13]. However, the $\nu_e + \nu_\mu + \nu_\tau$ flux measured by the NC process was $\phi_{NC} = 6.42^{+1.57}_{-1.57} \times 10^6 cm^{-2} s^{-1}$ [13], i.e., the ^8B predicted solar ν_e flux was consistent with the SSM predicted number of $\frac{1}{3}\nu_e + \frac{2}{3}\nu_\mu$. This is shown in Figure 2.3. Thus, the SNO experiment concluded that the solar ν_e's changed flavor into a different type of active neutrinos and not into undetectable right handed neutrinos. It also ruled out other possibilities put forth to explain the ν_e deficiency seen by Davis.

Super-Kamiokande[14], a 50-kton water Čerenkov detector in Kamioka, Japan, made observations consistent with the SNO observations and their results are also shown in Figure 2.12.

2.3.2 Atmospheric Neutrino Anomaly

Atmospheric neutrinos, about 1000 times more energetic than the ν_e's from β decay, are produced by cosmic ray interactions in the terrestrial atmosphere. Cosmic rays are highly energetic sub-atomic particles, mostly protons and helium nuclei, which travel across space at close to the speed of light.

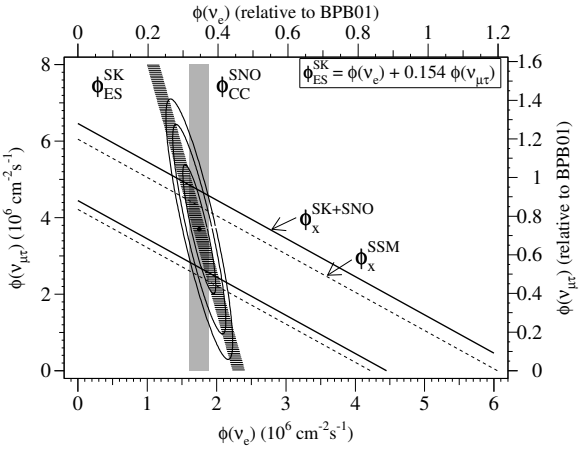

Figure 2.3: Flux of ^8B solar neutrinos which are μ or τ flavor vs. the flux of electron neutrinos as deduced from the SNO and Super-Kamiokande data. The diagonal bands show the total ^8B flux $\phi(\nu_x)$ as predicted by the SSM (dashed lines) and that derived from the SNO and Super-Kamiokande measurements (solid lines). The intercepts of these bands with the axes represent the $\pm 1\sigma$ errors. [12]

The collisions between cosmic rays and atmospheric nuclei produce hadronic showers that are mostly pions and some kaons, which decay into leptons and neutrinos.

$$p + N \rightarrow \pi^{\pm} + \ldots \tag{2.14}$$

$$\pi^{\pm} \rightarrow \mu^{\pm} + \nu_{\mu}(\bar{\nu_{\mu}}) \tag{2.15}$$

$$\mu^{\pm} \rightarrow e^{\pm} + \bar{\nu_{\mu}}(\nu_{\mu}) + \nu_e \tag{2.16}$$

Thus,

$$\frac{(\nu_{\mu} + \bar{\nu_{\mu}})}{(\nu_e + \bar{\nu_e})} \simeq 2 \tag{2.17}$$

The calculation of the total rate of neutrino production has large uncertainties of about 20%, but the observed ratio of $(\nu_{\mu} + \bar{\nu_{\mu}})/(\nu_e + \bar{\nu_e})$ to the expected ratio,

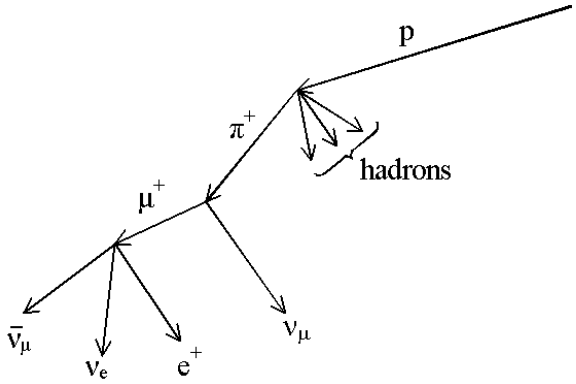

Figure 2.4: Sketch of cosmic ray collisions producing neutrinos

hereafter referred to as ratio of ratios (R), has an uncertainty of only 5%.

$$R = \frac{\left(\frac{(\nu_\mu+\bar{\nu_\mu})}{(\nu_e+\bar{\nu_e})}\right)_{data}}{\left(\frac{(\nu_\mu+\bar{\nu_\mu})}{(\nu_e+\bar{\nu_e})}\right)_{simulated}} = 1 \tag{2.18}$$

Even though this ratio of ratios was expected to be 1.0, data from several experiments gave R values different from this. Soudan 2, a 963 tonne fine grained gas tracking calorimeter measured $R = 0.64 \pm 0.11(stat.) \pm 0.06(syst.)$ [15] in 1999. The Kamiokande detector, a 4.5-kton water Čerenkov detector measured $R = 0.57^{0.08}_{0.07} \pm 0.07$ [16]. Earlier Čerenkov detectors like the Irvine Michigan Brookhaven (IMB)[17] had shown similar results, but with more uncertainty. Such measurements by quite different detector techniques, all yielding a ratio of ratios of less than 1.0 was confirmation that there was a deficit in the number of detected atmospheric neutrinos, which are mostly ν_μ's.

The atmospheric neutrino flux, with energies of about 10^2-10^3 MeV should be up-down symmetrical, making the upward going neutrino flux equal to the downward going one. But in 1998 Super-Kamiokande showed a strong deviation from this symmetry of upward ν_μ and downward ν_μ. Some of their results are shown in figure 2.5. The upward ν_μ events were much fewer than their predicted values whereas for

the downward ν_μ events the predicted and observed values were close.

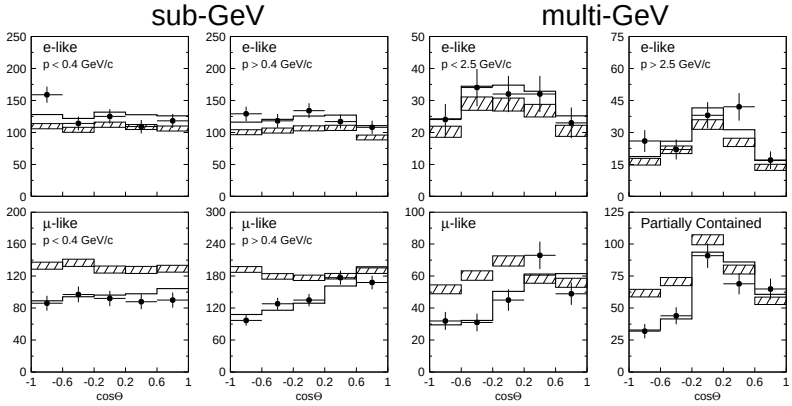

Figure 2.5: Atmospheric neutrino event rates observed by Super-Kamiokande as a function of the cosine of the zenith angle for sub-GeV and multi-GeV events. The hatched lines show the simulated events without oscillation and the black dots show the data.[18]

An obvious explanation was that the ν_μ's decayed into something else during their travel through the atmosphere. But the Super-Kamiokande experiment ruled out this possibility in 1999, by showing that the observations were not consistent with a decay hypothesis [19][20].

The possibility of the detected flavor of neutrinos changing into a different flavor, as in the solar neutrino problem, was again suggested. One of the ways this up-down neutrino anomaly could be explained was by looking at the difference in distances the upward and downward neutrinos traveled as shown in Figure 2.6. The distance the neutrinos traveled before encountering the detector is zenith angle, θ, dependent. It is seen from Figure 2.5 that the difference between the predicted and observed neutrino spectra depend on θ as well. So from Super-Kamiokande's results in that figure, it appeared that the phenomenon of "neutrino flavor change" was dependent on the distance they traveled.

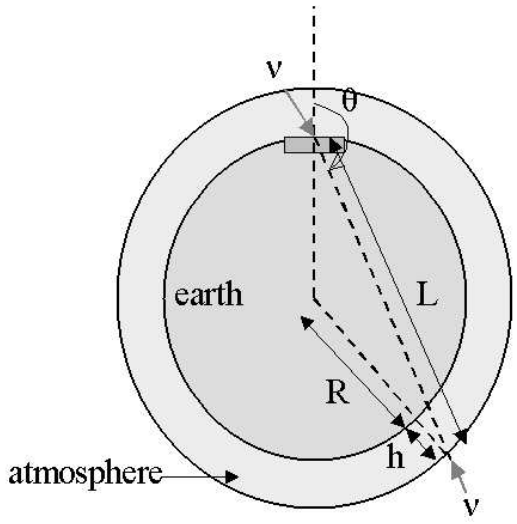

Figure 2.6: Upward and downward neutrinos entering a detector near the earth's surface. Here R is the radius of the earth, h is the height of the atmosphere, θ is the angle of the neutrino with respect to the vertical at the detector and L is the distance the neutrino travels before encountering the detector and is given by $L = \sqrt{R^2 \cos^2\theta + 2Rh + h^2} - R\cos\theta$

2.4 Neutrino Oscillations

In the late 1950s and early 1960s Pontecorvo, Maki, Nakagawa et al.[10] had theorized a phenomenon known as neutrino oscillations. In this theory, neutrinos of a definite flavor were in fact mixtures of different proportions of neutrino mass eigenstates. As neutrinos traveled through vacuum, these mixtures changed in proportionality, which resulted in a different neutrino flavor state than the one they started out with.

Neutrinos (ν_e, ν_μ and ν_τ),participate only in weak and gravitational interactions. If $m_\nu \geq 0$ these weak interaction eigenstates are expressed as combinations of mass eigenstates, ν_1, ν_2 and ν_3, that propagate in time with slightly different frequencies due to their mass differences.

The neutrino states of definite flavor, α, as generated by well defined weak interaction properties, are related to neutrino states of definite mass m_k by,

$$|\nu_\alpha\rangle = \sum_k U_{\alpha k} |\nu_k\rangle \tag{2.19}$$

where U is the Pontecorvo-Maki-Nakagawa-Sakata (PMNS) matrix, and is given by,

$$U = \begin{pmatrix} U_{e1} & U_{e2} & U_{e3} \\ U_{\mu 1} & U_{\mu 2} & U_{\mu 3} \\ U_{\tau 1} & U_{\tau 2} & U_{\tau 3} \end{pmatrix} \tag{2.20}$$

$$= \begin{pmatrix} c_{12}c_{13} & s_{12}c_{13} & s_{13}e^{-i\delta} \\ -s_{12}c_{23} - c_{12}s_{23}s_{13}e^{i\delta} & c_{12}c_{23} - s_{12}s_{23}s_{13}e^{i\delta} & s_{23}c_{13} \\ -s_{13}s_{23} - c_{12}c_{23}s_{13}e^{i\delta} & -c_{12}s_{23} - s_{12}c_{23}s_{13}e^{i\delta} & c_{13}c_{23} \end{pmatrix} \tag{2.21}$$

$$\times \begin{pmatrix} e^{i\alpha_1/2} & 0 & 0 \\ 0 & e^{i\alpha_2/2} & 0 \\ 0 & 0 & 1 \end{pmatrix} \tag{2.22}$$

where $c_{ij} = cos\theta_{ij}$ and $s_{ij} = sin\theta_{ij}$.

Then re-writing equation 2.19,

$$\begin{pmatrix} \nu_e \\ \nu_\mu \\ \nu_\tau \end{pmatrix} = \begin{pmatrix} U_{e1} & U_{e2} & U_{e3} \\ U_{\mu 1} & U_{\mu 2} & U_{\mu 3} \\ U_{\tau 1} & U_{\tau 2} & U_{\tau 3} \end{pmatrix} \begin{pmatrix} \nu_1 \\ \nu_2 \\ \nu_3 \end{pmatrix} \tag{2.23}$$

The PMNS matrix is unitary, so $U^\dagger U = I \Rightarrow U^{-1} = U\dagger = (U^*)^T$, which yields

$$\begin{pmatrix} \nu_1 \\ \nu_2 \\ \nu_3 \end{pmatrix} = \begin{pmatrix} U^*_{e1} & U^*_{\mu 1} & U^*_{\tau 1} \\ U^*_{e2} & U^*_{\mu 2} & U^*_{\tau 2} \\ U^*_{e3} & U^*_{\mu 3} & U^*_{\tau 3} \end{pmatrix} \begin{pmatrix} \nu_e \\ \nu_\mu \\ \nu_\tau \end{pmatrix} \tag{2.24}$$

Also the PMNS matrix yields several useful unitary relations -

$$\begin{pmatrix} U_{e1} & U_{e2} & U_{e3} \\ U_{\mu 1} & U_{\mu 2} & U_{\mu 3} \\ U_{\tau 1} & U_{\tau 2} & U_{\tau 3} \end{pmatrix} \begin{pmatrix} U^*_{e1} & U^*_{\mu 1} & U^*_{\tau 1} \\ U^*_{e2} & U^*_{\mu 2} & U^*_{\tau 2} \\ U^*_{e3} & U^*_{\mu 3} & U^*_{\tau 3} \end{pmatrix} = \begin{pmatrix} 1 & 0 & 0 \\ 0 & 1 & 0 \\ 0 & 0 & 1 \end{pmatrix} \tag{2.25}$$

$$U_{e1}U^*_{e1} + U_{e2}U^*_{e2} + U_{e3}U^*_{e3} = 1$$

$$U_{\mu 1}U^*_{\mu 1} + U_{\mu 2}U^*_{\mu 2} + U_{\mu 3}U^*_{\mu 3} = 1$$

$$U_{\tau 1}U^*_{\tau 1} + U_{\tau 2}U^*_{\tau 2} + U_{\tau 3}U^*_{\tau 3} = 1$$

$$U_{e1}U^*_{\mu 1} + U_{e2}U^*_{\mu 2} + U_{e3}U^*_{\mu 3} = 0$$

$$U_{e1}U^*_{\tau 1} + U_{e2}U^*_{\tau 2} + U_{e3}U^*_{\tau 3} = 0$$

$$U_{\mu 1}U^*_{\tau 1} + U_{\mu 2}U^*_{\tau 2} + U_{\mu 3}U^*_{\tau 3} = 0$$

If we start off with a neutrino of pure flavor of, say μ, i.e., ν_μ,

$$|\Psi(t=0)\rangle = |\nu_\mu\rangle = U_{\mu 1}|\nu_1\rangle + U_{\mu 2}|\nu_2\rangle + U_{\mu 3}|\nu_3\rangle \tag{2.26}$$

The time evolution of the neutrinos will be given by,

$$|\Psi(t)\rangle = U_{\mu 1}|\nu_1\rangle e^{-ip_1.x} + U_{\mu 2}|\nu_2\rangle e^{-ip_2.x} + U_{\mu 3}|\nu_3\rangle e^{-ip_3.x} \tag{2.27}$$

where, four-momentum $p_i = (E_i, \vec{p_i})$ and $x = (t, \vec{x})$ with Energy and momentum of i^{th} mass state after the wave function has traveled a x distance in time t, being E_i and p_i respectively.

$$\begin{aligned}
p_i.x &= E_i t - \vec{p_i}.\vec{x} \\
&= E_i t - p_i.x \text{ where, x axis is the direction of propagation of the wave} \\
&= (E_i - p_i)L \text{ for a distance L traveled, with c=1} \\
&= \frac{m_i^2}{2E_i}L \\
&\quad \text{since } E_i = (p_i^2 + m_i^2)^{\frac{1}{2}} = p_i(1 + \tfrac{1}{2}\tfrac{m_i^2}{p_i^2} + ...) \text{ and } E_i \simeq p_i \text{ for neutrinos}
\end{aligned}$$

Let $p_i.x = \frac{m_i^2}{2E_i}L = \phi_i$,

$$\begin{aligned}
|\Psi(L)\rangle &= U_{\mu 1}(U^*_{e1}|\nu_e\rangle + U^*_{\mu 1}|\nu_\mu\rangle + U^*_{\tau 1}|\nu_\tau\rangle)e^{-i\phi_1} \\
&+ U_{\mu 2}(U^*_{e2}|\nu_e\rangle + U^*_{\mu 2}|\nu_\mu\rangle + U^*_{\tau 2}|\nu_\tau\rangle)e^{-i\phi_2} \\
&+ U_{\mu 3}(U^*_{e3}|\nu_e\rangle + U^*_{\mu 3}|\nu_\mu\rangle + U^*_{\tau 3}|\nu_\tau\rangle)e^{-i\phi_3}
\end{aligned}$$

re-arranging,

$$\begin{aligned} |\Psi(L)\rangle &= (U_{\mu 1}U^*_{e1}e^{-i\phi_1} + U_{\mu 2}U^*_{e2}e^{-i\phi_2} + U_{\mu 3}U^*_{e3})|\nu_e\rangle \\ &+ (U_{\mu 1}U^*_{\mu 1}e^{-i\phi_1} + U_{\mu 2}U^*_{\mu 2}e^{-i\phi_2} + U_{\mu 3}U^*_{\mu 3}e^{-i\phi_3})|\nu_\mu\rangle \\ &+ (U_{\mu 1}U^*_{\tau 1}e^{-i\phi_1} + U_{\mu 2}U^*_{\tau 2}e^{-i\phi_2} + U_{\mu 3}U^*_{\tau 3}e^{-i\phi_3})|\nu_\tau\rangle \end{aligned}$$

Then, the probability, $P(\nu_\mu \rightarrow \nu_\mu)$, of finding a neutrino of flavor type μ after having started off with a beam of pure flavor μ neutrinos that has traversed a distance L;

$$\begin{aligned} P(\nu_\mu \rightarrow \nu_\mu) &= \mid \langle \nu_\mu | \Psi(L) \rangle \mid^2 \\ &= \mid (U_{\mu 1}U^*_{\mu 1}e^{-i\phi_1} + U_{\mu 2}U^*_{\mu 2}e^{-i\phi_2} + U_{\mu 3}U^*_{\mu 3}e^{-i\phi_3}) \mid^2 \end{aligned}$$

Using $\mid z_1 + z_2 + z_3 \mid^2 = \mid z_1 \mid^2 + \mid z_2 \mid^2 + \mid z_2 \mid^2 + 2\Re(z_1 z_2^* + z_1 z_3^* + z_2 z_2^*)$ for complex numbers, and a result from the unitary identities of the matrix U, $\mid U_{\mu 1}U^*_{\mu 1} \mid^2 + \mid U_{\mu 2}U^*_{\mu 2} \mid^2 + \mid U_{\mu 3}U^*_{\mu 3} \mid^2 = 1$,

$$\begin{aligned} P(\nu_\mu \rightarrow \nu_\mu) &= 1 + 2 \mid U_{\mu 1} \mid^2 \mid U_{\mu 2} \mid^2 \Re(e^{-i(\phi_1 - \phi_2)} - 1) \\ &+ 2 \mid U_{\mu 1} \mid^2 \mid U_{\mu 3} \mid^2 \Re(e^{-i(\phi_1 - \phi_3)} - 1) \\ &+ 2 \mid U_{\mu 2} \mid^2 \mid U_{\mu 3} \mid^2 \Re(e^{-i(\phi_2 - \phi_3)} - 1) \end{aligned}$$

Simplifying for the real part of the complex number,

$$\begin{aligned}\Re(e^{-i(\phi_1-\phi_2)}-1) &= cos(\phi_2-\phi_1)-1 \\ &= -2sin^2\left(\frac{\phi_2-\phi_1}{2}\right) \\ &= -2sin^2\left(\frac{(m_2^2-m_1^2)L}{4E}\right) \text{ since } \phi_i \simeq \tfrac{m_i^2}{2E_i}L\end{aligned}$$

and converting back from natural units,

$$\Re(e^{-i(\phi_1-\phi_2)}-1) = -2sin^2\left(1.27\frac{\Delta m_{12}(eV^2)L(km)}{E(GeV)}\right) \tag{2.28}$$

$$P(\nu_\alpha \to \nu_\alpha) = 1 - 4\sum_{i<j} \mid U_{\alpha i} \mid^2 \mid U_{\alpha j} \mid^2 sin^2\left(1.27\frac{\Delta m_{ji}(eV^2)L(km)}{E(GeV)}\right) \tag{2.29}$$

The PMNS matrix in Equation 2.22, can also be expressed in terms of three rotation angles θ_{12}, θ_{13} and θ_{23} and a complex phase δ,

$$\begin{aligned}\begin{pmatrix} U_{e1} & U_{e2} & U_{e3} \\ U_{\mu 1} & U_{\mu 2} & U_{\mu 3} \\ U_{\tau 1} & U_{\tau 2} & U_{\tau 3} \end{pmatrix} &= \begin{pmatrix} 1 & 0 & 1 \\ 0 & c_{23} & s_{23} \\ 0 & -s_{23} & c_{23} \end{pmatrix} \\ &\times \begin{pmatrix} c_{13} & 0 & s_{13}e^{-i\delta} \\ 0 & 1 & 0 \\ -s_{13}e^{-i\delta} & 0 & c_{13} \end{pmatrix} \\ &\times \begin{pmatrix} c_{12} & s_{12} & 0 \\ -s_{12} & c_{12} & 0 \\ 0 & 0 & 1 \end{pmatrix}\end{aligned}$$

where $c_{ij} = cos\theta_{ij}$ and $s_{ij} = sin\theta_{ij}$.

Current experimental evidence suggests that $|\Delta m^2_{23}| >> |\Delta m^2_{12}|$ and $\theta_{13} \simeq 0$[28]. This allows the three flavor oscillation mechanism to be reduced to a two flavor one, coupled to just two mass states.

Then the ν_μ survival probability is dominated by the term,

$$\begin{pmatrix} 1 & 0 & 1 \\ 0 & c_{23} & s_{23} \\ 0 & -s_{23} & c_{23} \end{pmatrix} \tag{2.30}$$

and the ν_e survival probability is dominated by the term,

$$\begin{pmatrix} c_{12} & s_{12} & 0 \\ -s_{12} & c_{12} & 0 \\ 0 & 0 & 1 \end{pmatrix} \tag{2.31}$$

We can then consider a two-flavor oscillation scheme for simplicity. Any given two flavors could be expressed as a linear combination of the two mass eigenstates say ν_i and ν_j, through a unitary transformation involving an arbitrary mixing angle θ_{ij}:

$$\begin{pmatrix} \nu_a \\ \nu_b \end{pmatrix} = \begin{pmatrix} \cos\theta_{ij} & \sin\theta_{ij} \\ -\sin\theta_{ij} & \cos\theta_{ij} \end{pmatrix} \begin{pmatrix} \nu_i \\ \nu_j \end{pmatrix}$$

$$\begin{aligned} |\nu_a\rangle &= \cos\theta_{ij}|\nu_i\rangle + \sin\theta_{ij}|\nu_j\rangle \\ |\nu_b\rangle &= -\sin\theta_{ij}|\nu_i\rangle + \cos\theta_{ij}|\nu_j\rangle \end{aligned}$$

The time evolution of the neutrinos will be given by,

$$\begin{aligned}
|\nu_a(t)\rangle &= \cos\theta_{ij} e^{-iE_i t}|\nu_i\rangle + \sin\theta_{ij} e^{-iE_j t}|\nu_j\rangle \\
&= \left(\cos^2\theta_{ij} e^{-iE_i t} + \sin^2\theta_{ij} e^{-iE_j t}\right)|\nu_a(0)\rangle + \sin\theta_{ij}\cos\theta_{ij}\left(e^{-iE_j t} - e^{-iE_i t}\right)|\nu_b(0)\rangle \\
|\nu_b(t)\rangle &= -\sin\theta_{ij} e^{-iE_i t}|\nu_i\rangle + \cos\theta_{ij} e^{-iE_j t}|\nu_2\rangle \\
&= \left(\sin^2\theta_{ij} e^{-iE_i t} + \cos^2\theta_{ij} e^{-iE_j t}\right)|\nu_b(0)\rangle + \sin\theta_{ij}\cos\theta_{ij}\left(e^{-iE_j t} - e^{-iE_i t}\right)|\nu_a(0)\rangle
\end{aligned}$$

From this we obtain the probability of finding a neutrino of flavor type b after having started off with a beam of pure flavor a neutrinos, $P(\nu_a \rightarrow \nu_b)$;

$$\begin{aligned}
P(\nu_a \rightarrow \nu_b) &= |\ \langle\nu_b(t)||\nu_a(0)\rangle\ |^2 \\
&= \sin^2\theta_{ij}\cos^2\theta_{ij}\left(1 + 1 - e^{i(E_j - E_i)t} - e^{i(E_i - E_j)t}\right) \\
&= 2\sin^2\theta_{ij}\cos^2\theta_{ij}\left(1 - \cos\left(E_i - E_j\right)t\right)
\end{aligned}$$

Re-writing,

$$\begin{aligned}
E_i - E_j &= \left(p + \frac{{m_i}^2}{2p}\right) - \left(p + \frac{{m_j}^2}{2p}\right) \qquad \text{for } m^2 << p \\
&= \frac{{\Delta m_{ij}}^2}{p} \qquad \text{where } {\Delta m_{ij}}^2 = {m_i}^2 - {m_j}^2
\end{aligned}$$

For ultra-relativistic neutrinos with $t = L/c$,

$$\begin{aligned}
P(\nu_a \rightarrow \nu_b) &= 2\sin^2\theta_{ij}\cos^2\theta_{ij}\left(1 - \cos\frac{{\Delta m_{ij}}^2}{2p}\frac{L}{c}\right) \\
&= \sin^2 2\theta_{ij} sin^2\left(\frac{{\Delta m_{ij}}^2}{4E}L\right) \qquad \text{since } E = pc \text{ with } m << p \text{ for neutrinos}
\end{aligned}$$

Finally we convert to natural units to yield the probability, $P(\nu_a \rightarrow \nu_b)$, of finding a neutrino of flavor type b after having started off with a beam of pure flavor a neutrinos that has traversed a distance L;

$$P(\nu_a \rightarrow \nu_b) = \sin^2 2\theta_{ij} \sin^2 \left(1.27 \Delta {m_{ij}}^2 (eV^2) \frac{L(km)}{E(GeV)} \right) \tag{2.32}$$

and the probability, $P(\nu_a \rightarrow \nu_a)$, of finding a neutrino of flavor type a after having started off with a beam of pure flavor a neutrinos;

$$P(\nu_a \rightarrow \nu_a) = 1 - \left(\sin^2 \ 2\theta_{ij} \sin^2 \left(1.27 \Delta {m_{ij}}^2 (eV^2) \frac{L(km)}{E(GeV)} \right) \right) \tag{2.33}$$

where θ_{ij} is the mixing angle, $\Delta {m_{ij}}^2$ is the mass squared difference between the said neutrino types i and j $(in\ eV^2)$, L is the distance traveled $(in\ km)$ and E is the neutrino energy $(in\ GeV)$.

For muon neutrinos, the probability of survival is given by,

$$P(\nu_\mu \rightarrow \nu_\mu) = 1 - \sin^2 2\theta_{23} \sin^2 \left(1.27 \Delta {m^2_{23}}^2 \frac{L}{E} \right) \tag{2.34}$$

Figure 2.7 shows how this probability changes with the neutrino energy.

Thus if neutrinos were to have nonzero mass differences, given that θ_{23} is nonzero and the distance traveled L is comparable to

$$L_{osc} = 2.48 \times \frac{E/(GeV)}{\Delta m^2/(eV^2)} km \tag{2.35}$$

then the probability that one flavor of neutrinos will oscillate into a different flavor would be non-zero too.

The atmospheric neutrino anomaly observed in Super-Kamiokande can be ex-

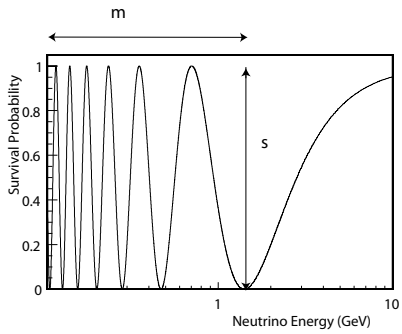

Figure 2.7: Muon neutrino survival probability as a function of the neutrino energy, for $(\Delta m^2_{23}{}^2, \sin^2 2\theta_{23}) = (2.38 \times 10^{-3}, 1.0)$. The position of the oscillation minimum, m, dictates Δm^2_{23} and the amplitude, s, dictates $\sin^2 2\theta_{23}$

plained by looking at the distance the neutrinos travel before encountering the detector as shown in figure 2.6. The upward going neutrinos that travel a much greater distance ($\sim 12,000km$) than the downward going ones ($\sim 20km$), will have a higher probability of oscillation. This results in a smaller than predicted number for the upward going ν_μ flux as shown in Figure 2.5.

Also since Super-Kamiokande does not see the upward ν_e flux increase over its predicted value, it must be that the oscillating upward ν_μ's are doing so into a flavor other than ν_e's. The CHOOZ reactor experiment shows that the mixing angle $sin2\theta_{12}$ for the $\nu_\mu \rightarrow \nu_e$ oscillations is small [23]. This leads us to perceive that ν_μ's oscillate into ν_τ's or possibly $\nu_{sterile}$'s.

The Super-Kamiokande experiment's data were fit to obtain $\nu_\mu \rightarrow \nu_\tau$ oscillation parameters of $\sin^2 2\theta_{23} > 0.92$ and $1.5 \times 10^{-3} < \Delta m^2_{23} < 3.4 \times 10^{-3} eV^2$ at a 90% confidence level.[21] They also ruled out $\nu_\mu \rightarrow \nu_{sterile}$ oscillations at a 99% confidence level.[22]

2.5 Neutrino Knowledge by the Early 2000's

Neutrino experiments in the latter half of the 20th century led to many exciting observations. By the 2000's three of the neutrino flavors had been directly observed and other physical properties like the neutrino helicity was determined. A number of physics Nobel Prizes recognized these discoveries.

Most experiments were looking at nature-made neutrinos such as those from the sun and those produced in the atmosphere, while others were looking at reactor neutrinos, both with the goal of testing previous oscillation measurements. The former relied on solar and atmospheric cosmic ray flux models and the latter relied on neutrino-nucleon cross-section calculations and were affected by the fact that neutrino scattering cross-sections at low energies, were not well understood.

The few accelerator based experiments such as NOMAD[24] and CHORUS studied high energy muon neutrinos and they were short baseline experiments, where the baseline is the distance the neutrinos travel.

In light of the results from these neutrino oscillation experiments the need for a new experiment with fewer uncertainties became more and more evident. Since the Standard Model of Particle Physics incorporates neutrinos as massless particles but the neutrino oscillation hypothesis requires neutrinos to have mass, such an experiment would open a window into physics beyond the Standard Model.

Chapter 3

The MINOS Experiment

3.1 Introduction and Motivation

By the late 1990's such experimental evidence as the solar neutrino deficit and the atmospheric neutrino anomaly had led to the conclusion that neutrinos oscillate. But the uncertainties in the oscillation parameters, namely Δm^2 and $sin^2 2\theta$, remained high due to the uncertainties in the neutrino fluxes, their energies and the distances they travel.

Around this same time, Fermilab completed its Main Injector (MI). The MI is an accelerator of protons up to an energy of 120GeV, built to increase the beam intensity for collider experiments. The same set of reactions (equations 2.14, 2.15 and 2.16) that produced atmospheric neutrinos from cosmic ray protons could now be used to make a beam of neutrinos from the Main Injector protons: If very high energy protons are made to collide with nuclei of some material, then that will produce pions which in turn decay into neutrinos. Such a neutrino beam will yield more precise measurements of the oscillation parameters, since the energy of the neutrinos and the distance they travel will be known to a higher precision. In this case the energy of the proton beam, together with pion focusing magnets, will

dictate the energy of the neutrino beam and the distance the neutrinos travel can be controlled by how far away from the proton target the neutrino detector is placed.

An experiment to study such beam neutrinos was conceived in 1990 and was named the Main Injector Neutrino Oscillation Search (MINOS). This experiment utilizes two detectors : a Near Detector that measures the neutrino beam right after they are produced, before they have had time to oscillate and a Far Detector that measures the neutrino beam after they are given enough time to develop oscillations.

The goal of the MINOS experiment was to make a precision measurement of θ_{23} and Δm^2_{23} under controlled conditions[25]. This thesis will describe the study of QEL scattering events in the MINOS experiment to measure Δm^2_{23} and $sin^2 2\theta_{23}$.

MINOS uses an almost pure muon neutrino ν_μ beam of average energy about 3 GeV. The neutrinos are made by protons from the Fermilab Main Injector hitting a graphite target, producing pions that decay into neutrinos. The experiment uses two detectors to minimize systematic uncertainties: A Near Detector, near the neutrino source at Fermilab measures the neutrino interaction rate right after the neutrinos are produced, before they have oscillated. A Far Detector, 734km away from the neutrino source, measures the rate after they have had time to oscillate. The Far Detector, situated in the University of Minnesota Soudan Underground Laboratory in Soudan MN, is shielded from cosmic rays in an old iron mine 710m below ground level. Both detectors are made of alternating steel and scintillator planes, the steel providing the mass for the neutrino interactions and the scintillator detecting the charged particles resulting from neutrino interactions.

MINOS is a disappearance experiment, i.e., it looks for a deficit in the ν_μ flux after they have traveled 734km. To understand why this is a disappearance experiment instead of an appearance one, we will have to understand neutrino interactions with matter.

As mentioned in Section 1, neutrinos interact with matter in two ways: charged

current interactions and neutral current interactions. The MINOS oscillation analysis will be based primarily on charged current interactions, in which the neutrino is identified by the charged lepton partner it produces.

Due to energy limitations, not all neutrinos interact via the easy-to-identify charged current process. For a charged current neutrino interaction given by

$$\nu_X + N \rightarrow X + N \tag{3.1}$$

where $X = e, \mu$ or τ and $N = p$ or n, the energy threshold $E_{\nu_X}(thresh)$ (Appendix A.1) is,

$$E_{\nu_X}(thresh) = \frac{m_X(m_X + 2m_N)}{2m_N} \tag{3.2}$$

where m_X is the mass of the relevant charged lepton and m_N is the mass of the neutron or proton involved in the interaction.

$$\begin{aligned} \text{threshold for } \nu_\mu \text{ CC process : } E_{\nu_\mu}(thresh) &\sim 0.1 GeV \\ \text{threshold for } \nu_\tau \text{ CC process : } E_{\nu_\tau}(thresh) &\sim 3.5 GeV \end{aligned}$$

But MINOS operates at an average neutrino energy of 3 GeV. So if the ν_μ's had oscillated into ν_τ's (as was deduced from Super-Kamiokande), most of those ν_τ's will not interact via charged currents. The few that interact will each produce a τ that quickly decays, producing small showers that are difficult to distinguish from other hadronic showers. The muon produced by the ν_μ CC interaction, however, gives an easily identifiable long muon track. For these reasons MINOS has been designed as a disappearance experiment, i.e., it detects the ν_μ's via the muons, and looks for a deficit in the expected number of ν_μ's.

3.2 The NuMI Beam

The Neutrinos at Main Injector (NuMI) facility delivers an intense tertiary beam of ν_μ's to MINOS. Protons of energy 120GeV extracted in 8.6μsec long spill cycles with a frequency of 0.53Hz from the Main Injector are bent 58 $mrad$ downward to aim at Soudan, MN and are incident on a $6.4\times15\times940mm^3$ longitudinally segmented graphite target. The target is segmented into 47 parts that are 2.0 cm long, shorter than the hadronic interaction length of 38cm for carbon, so that secondary pions and kaons have a greater chance to escape before interacting with the target. The schematics of the neutrino beam is shown in Figure 3.1. These secondary pions and kaons decay into neutrinos and muons, where the muons again decay into neutrinos, just as for the atmospheric neutrinos, shown in Equations 2.15 and 2.16.

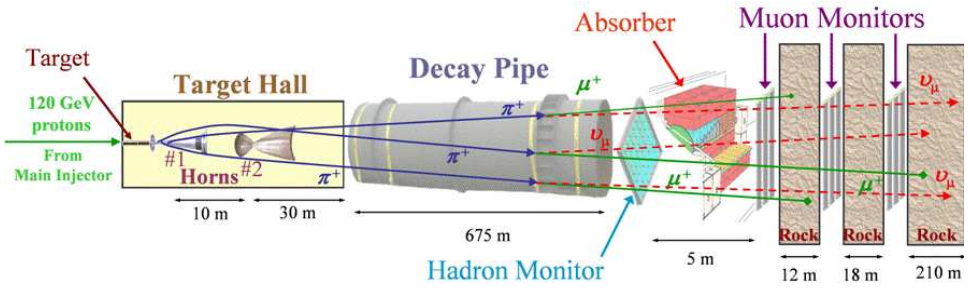

Figure 3.1: Protons extracted from the Main Injector at Fermilab are incident on a graphite target, giving out pions and kaons. These secondary pions and kaons are energy selected and directed by two magnetic horns into a 675m long decay pipe, where they decay to produce a ν_μ's and μ's. The μ's and any undecayed hadrons are absorbed by absorbers between the end of the decay pipe and the near detector, thus producing a pure neutrino beam.

The choice of the energy of the neutrino beam is dependent on the survival probability of the ν_μ's. From Equation 2.32, the probability of ν_μ survival is $P(\nu_\mu \rightarrow \nu_\mu) = 1 - \sin^2 2\theta_{23} \sin^2\left(1.27\Delta {m_{23}}^2(eV^2)\frac{L(km)}{E(GeV)}\right)$. It can be seen that amplitude of oscillations will be maximized when $\left(1.27\Delta {m_{23}}^2\frac{L}{E}\right) = \frac{\pi}{2}$. This in turn means that

neutrino flavor oscillations will be maximized for a neutrino energy, E, of,

$$E = 0.81 \times \Delta m^2_{23}(eV^2) \times L(km) \tag{3.3}$$

The best estimate of Δm^2_{23} at the time of the experiment's design was $\sim 10^{-2}\ eV^2$, corresponding to a neutrino energy of $3GeV$. These neutrinos are decay products of pions from $\pi \rightarrow \nu_\mu + \mu^+$ and the neutrino energy E_ν (Appendix A.2) for small production angles is given by,

$$E_\nu = \frac{0.43 E_\pi}{1 + \gamma^2\theta^2} \tag{3.4}$$

where γ is the pion relativistic boost and θ is the neutrino emission angle at decay. Then, for neutrinos of $3GeV$ that are produced along the direction of the pions, the parent pion will have about $7GeV$ in energy. To increase the flux of muons, the secondary pions and kaons escaping the target are focused by two magnetic horns that carry a 200kA current in parabolic shaped conductors making a 30kG toroidal magnetic lens that selects and focuses pions of the desired energy of about $7GeV$. The target is mounted on a rail-drive system, allowing it to be moved closer or further away from the horns, thereby selecting lower or higher energy secondaries respectively, resulting in lower or higher energy neutrino beam. Figure 3.2 shows three neutrino energy spectra, low energy (LE), Medium Energy (ME) and High Energy (HE) that can be obtained by moving the target as such. The analysis presented in this thesis is based on the LE energy configuration.

The pions and kaons produced enter a 675m long 2m diameter vacuum pipe at a pressure of $1Torr$. The length of this pipe is roughly 1.5 times the decay length of a $7GeV$ pion. The pions and kaons decay into ν_μ via $\pi^+ \rightarrow \mu^+ + \nu_\mu$ and $K^+ \rightarrow \mu^+ + \nu_\mu$. The μ's, together with any remaining pions, are absorbed by a metal absorber at the end of the decay pipe and 240m of rock between the end of the decay pipe and

the Near Detector.

The neutrino beam made as such has a composition of 98.5% ν_μ and $\bar{\nu_\mu}$ (only 6.5% of this 98.5% are $\bar{\nu_\mu}$'s) and 1.5% $\nu_e + \bar{\nu_e}$ [26]. The pure neutrino beam, with more than 98% ν_μ and $\bar{\nu_\mu}$'s thus obtained, is analyzed at the Near Detector $1km$ away from the NuMI target.

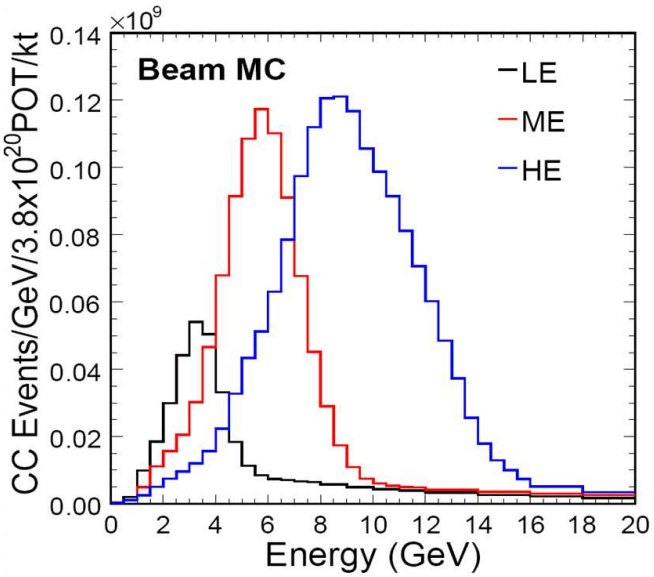

Figure 3.2: The three different NuMI Beam energy spectra, low energy (LE), Medium Energy (ME) and High Energy (HE) that can be obtained by moving the target[26]

3.3 MINOS Detectors

Both the MINOS Near Detector and the Far Detector are magnetized and are made of alternating steel and scintillator planes.

Neutrinos are weakly interacting particles with the cross section for a neutrino-nucleon scattering, $\sigma(\nu_\mu + N \rightarrow \mu^- + p)$, is such that $\sigma(\nu_\mu + N \rightarrow \mu^- + p) \simeq E_\nu \times 10^{-38} cm^2$ for neutrinos of energies above $0.5GeV$. That is, about one in every

3×10^{13} of the $3GeV$ neutrinos will interact within 1 m steel. Because of this low cross section it is important to have a large target mass of the detector, thereby increasing the number of nucleons they can scatter off. The steel in the detectors provides the mass required for these scarce neutrino interactions.

Since 6.5% of the muon neutrinos are $\bar{\nu_\mu}$'s, it is important to be able to distinguish the ν_μ's from the $\bar{\nu_\mu}$'s, i.e., to separate μ^-'s from the μ^+'s. For this purpose both MINOS detectors use a magnetic field. In both detectors a coil is passed through the longitudinal axis of the detector providing a toroidal magnetic field.

A charged particle of momentum p in a magnetic field $B(T)$ will trace a helix with radius $R(m)$ and pitch angle λ, according to $pcos\lambda = 0.3zBR$ [28]. Depending on the charge of the particle, the curvature would be either inward or outward. The magnetic field is oriented in such a way that the μ^-'s are focused to the inside of the detector. This magnetic field also allows the measurement of the muon momentum.

Plastic scintillator planes sandwiched between the steel planes detect the charged particles produced in the neutrino interactions.Each scintillator plane is made of individual strips with a cross section of 4 cm x 1 cm. These scintillator strips are made of polystyrene, infused with fluors and they are TiO_2 clad to maximize internal reflection. Scintillation light produced in the strips are wavelength shifted from blue to green by 1.2 mm [29] wavelength shifting (WLS) fibres glued to a central groove of the scintillator strip (figure3.3) and carried to multi-pixel photomultiplier tubes (PMT's) situated around the edges of the detectors. The light is transmitted to the PMT's at both ends of a strip using clear fibre. Calibration of the light pulses accounting for the attenuation length in the WLS fibers were carried out using LED bulbs [29]. Each pixel in a PMT receives signals from eight such fibers coming from spatially separated strips, in such a way that ambiguities can be resolved when reconstructing the path of the charged particle. This 8-fold multiplexer is shown in Figure 3.4. When a minimum ionizing particle (MIP) goes through the center of

the scintillator strip, it produces on average 10*pe*'s[30] in the summed signal from both ends of the strip.

Scintillator strips are arranged in orthogonal (U and V) directions in alternate planes. This orthogonal arrangement, together with the small width of 4*cm* of the strips, allows for a three dimensional readout of the trajectory of the charged particle.

Figure 3.3: A MINOS scintillator illuminated. The bright center line is the groove in which the WLS fiber is embedded.

3.3.1 Near Detector

The neutrino beam is first analyzed by the Near Detector , shown in Figure 3.5, which is made to look like the Far Detector as much as possible. This is located about 1km downstream of the proton target, a distance short enough that a measurement of the neutrino flux serves as a good indication of the unoscillated neutrino beam. The high neutrino flux at the Near Detector allows for a smaller detector and also for the detector to be located only 100m deep underground, because the neutrino rate during a beam spill ($>$ 30 interactions per 8.6 μs spill) far outnumbers the cosmic ray rate at that depth. The Near Detector is made of 282 steel planes; the upstream 120 planes (calorimeter section) are all instrumented, while only every 5th plane in the downstream 162 planes (the spectrometer section) are instrumented

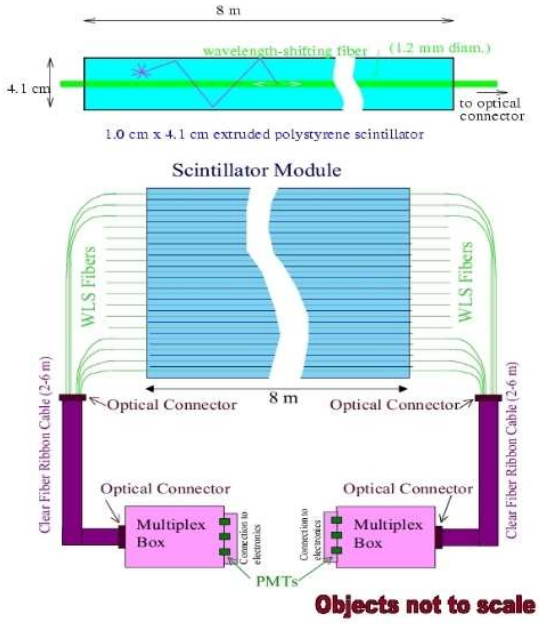

Figure 3.4: Schematics of the scintillator and readout system. Light emitted by a charged particle moving through the scintillator is collected by the WLS fiber and transfered to the PMTs via clear fibers.

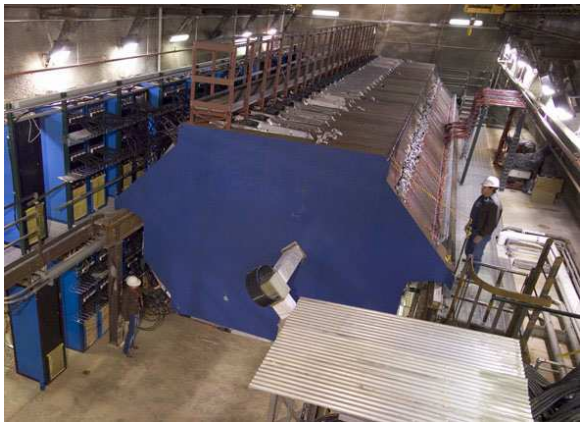

Figure 3.5: The MINOS Near Detector

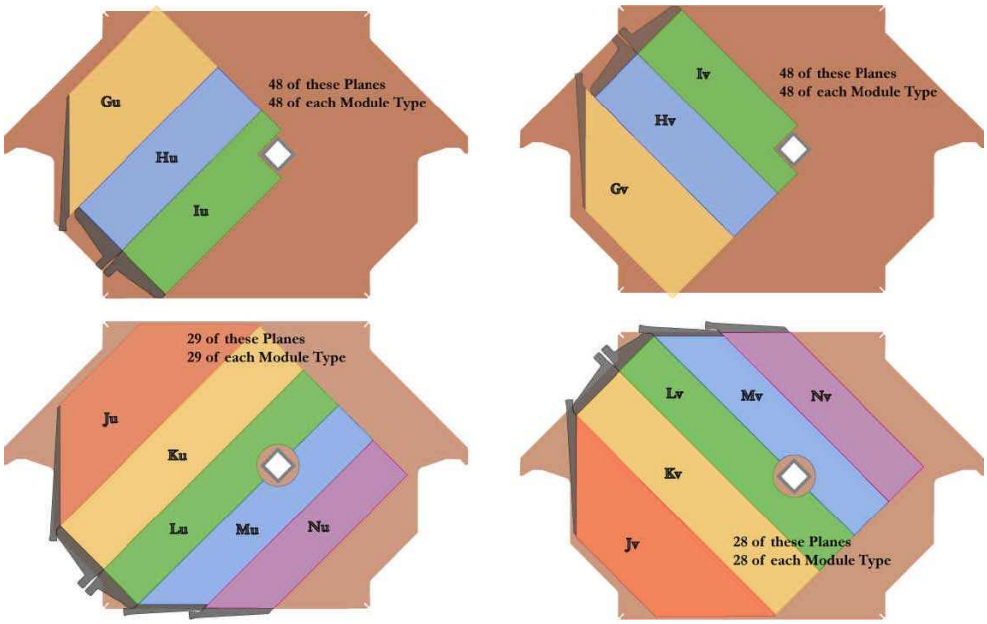

Figure 3.6: The MINOS Near Detector instrumentation. The two top figures are partially instrumented planes and the two bottom figures are fully instrumented planes. Alternating planes have these four configurations. The left two diagrams are scintillator planes oriented in the U direction and the right two are those oriented in the V direction. The letters G-N represent different shapes of the scintillator modules.

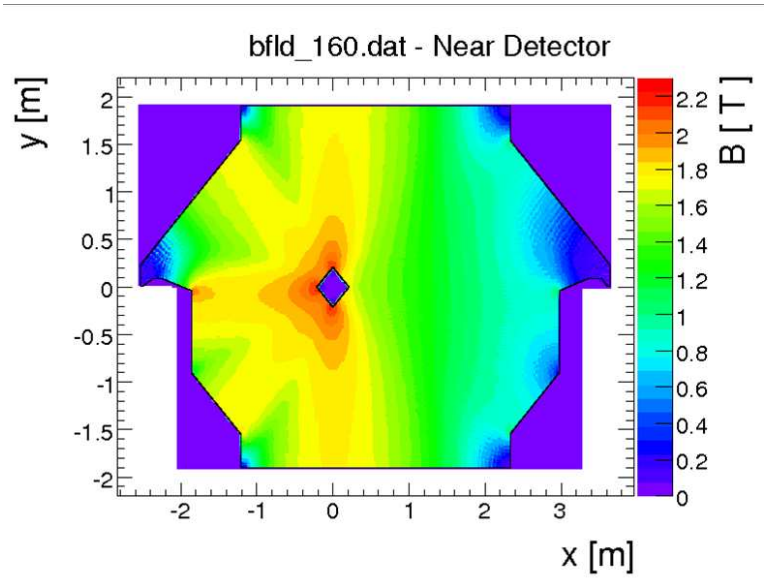

Figure 3.7: The MINOS Near Detector magnetic field map [27].

(Figure 3.6). The Near Detector is a 980 tonne 4.8m x 3.8 m x 16.6m detector. The 1.16T[27] (at the center of the planes) toroidal magnetic field is provided by an 8 turn 40kA-turn coil. A map of the Near Detector magnetic field is shown in Figure 3.7. The Near Detector coil hole is offset from the center of the detector planes by 0.56m and the neutrino beam is aligned such that it is centered between the coil hole and the left vertical edge of the beam. This positioning of the neutrino beam on the detector allows for every other plane to be only partially instrumented as shown in Figure 3.6.

3.3.2 Far Detector

The Far Detector, shown in Figure 3.8, is located 735.3km away from the proton target. It is housed in the University of Minnesota operated Soudan Underground Laboratory, 705m underground in an old iron mine in Soudan, MN. The divergence

of the neutrino beam reduces its central intensity by a factor of about 10^6 when it reaches Soudan, MN. To accommodate this decrease in neutrino intensity, the Far Detector is made to be much larger than the Near Detector, at 5.4 ktonnes of 486, 8m wide octagonal steel planes. To minimize the cosmic ray rate in the Far Detector, it is housed in a cavern 705 m underground, thereby reducing the total cosmic ray rate to $\sim 0.5\ Hz$. The Far Detector consists of two supermodules each magnetized to 1.42 T (at a 2 m radius from the center[27]) using two separate coils carrying a total of 15.2 $kA-turn$ each. A map of the Far Detector magnetic field is shown in Figure 3.10. The Far Detector is fully instrumented with plastic scintillator planes between the steel planes, with the exception of the upstream plane of each supermodule that is not instrumented. In the Far Detector a scintillator plane is made of eight individual scintillator modules, each module made of either 20 or 28 strips as shown in the Figure 3.9. Thus each scintillator plane consists of 192 strips in total, each with a cross section of 4 cm x 1 cm and a length up to 8 m, depending on its position.

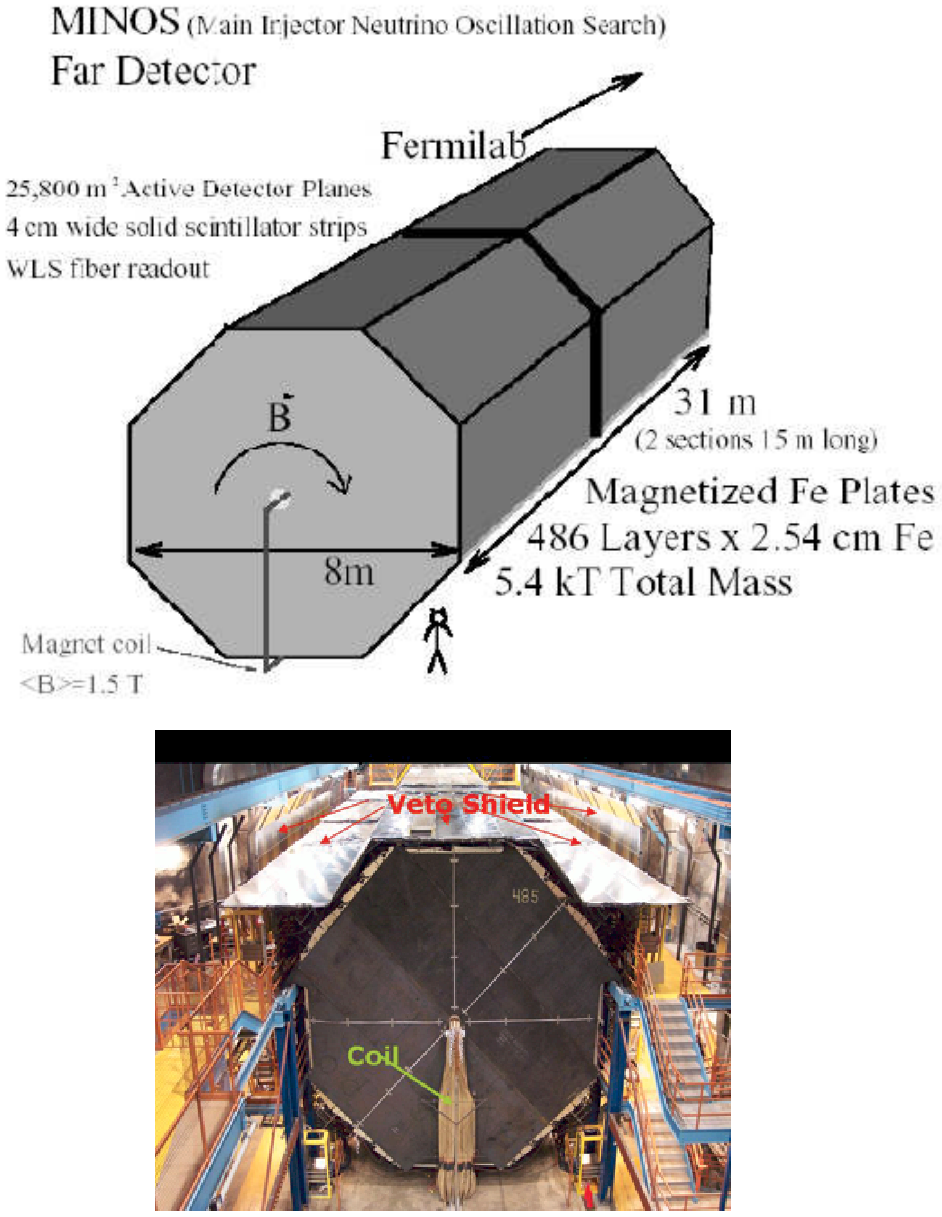

Figure 3.8: MINOS Far Detector

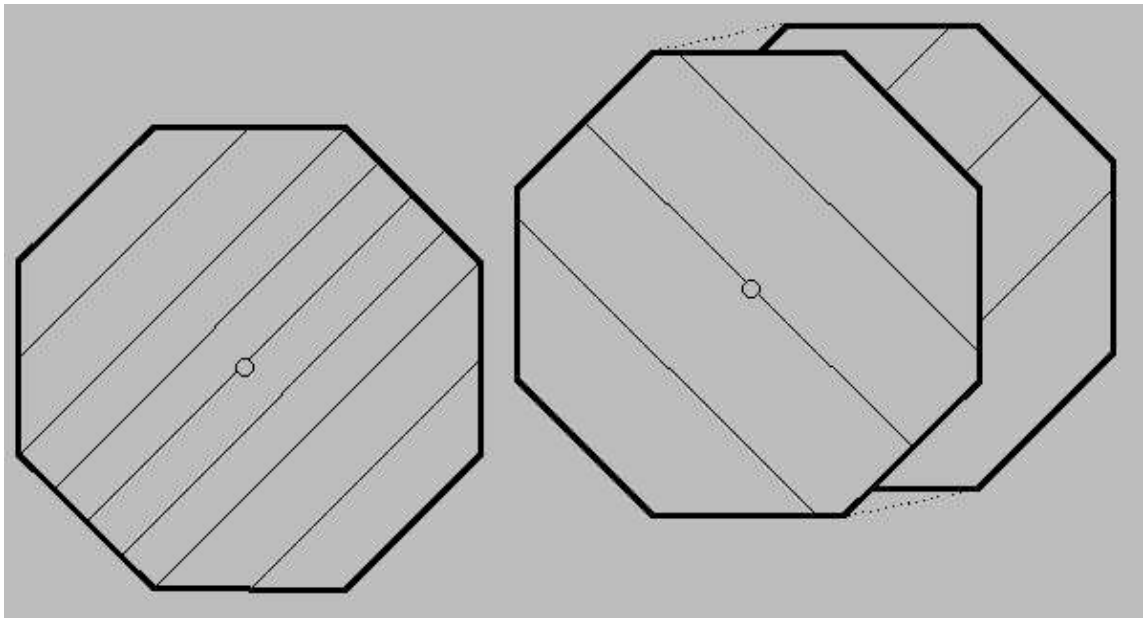

Figure 3.9: The MINOS Far Detector instrumentation showing the alternating U and V readout of the scintillator strips.

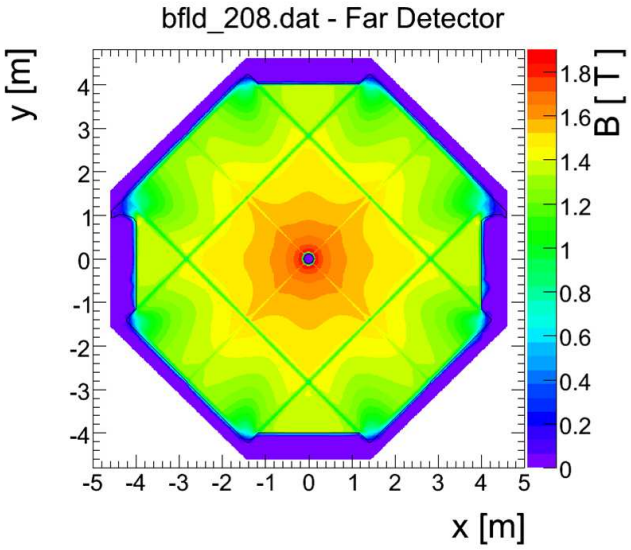

Figure 3.10: The MINOS Far Detector magnetic field map [27].

3.4 Charged Particle Identification in the MINOS Detectors

As described earlier, out of the two ways ν_μ's from the NuMI beam interact with the steel, the charged current interaction ($\nu_\mu + N \rightarrow \mu + ...$) provides a better signature than the neutral current one ($\nu_\mu + N \rightarrow \nu_\mu + ...$), because it emits the charged lepton corresponding to the neutrino flavor. Even though the neutrino beam from NuMI is mostly ν_μ's, there are a few ν_e's as well. MINOS must be able to distinguish between ν_μ's and these ν_e's, i.e., the resulting μ's from the e's .

While muons from the ν_μ charged current events are long and track-like, the electrons from the ν_e CC events and the hadrons from the neutral current events are short and shower-like. The track-like and shower-like nature of ν_μ CC, ν_e CC and NC interactions is explicable by looking at the energy loss of secondary particles, muons, electrons and π^0's produced in these interactions.

There are two main ways charged particles lose energy: ionization and radiation. Which of these processes dominates depends on the energy of the particle. A critical energy, E_{crit} (Appendix A.3), can be defined such that, when the kinetic energy of the moving particle is below E_{crit}, energy loss by ionization dominates and when the particle's kinetic energy is above E_{crit}, energy loss by radiation dominates and grows rapidly with E.

For electrons in iron, this critical energy, E_{crit_e},

$$E_{crite} = 29.4MeV \tag{3.5}$$

Since the electrons that we consider with energies about $1GeV$ are well above their critical energy of $E_{crite} = 29.4MeV$ they lose energy by radiation and initially this loss is $70.2MeVg^{-1}cm^2$ as calculated from equation Equation A.4. Because the

initial energy loss is so rapid, electrons don't travel far before radiating. Furthermore, the photons thus radiated by electrons can create an e^+e^- pair. Each member of that pair can radiate photons which in turn can create more e^+e^- pairs. This resulting cascade of e^+e^- pairs and photons is called an electromagnetic shower.

Since the mean free path of pair production, L_{PP} in iron is $2.26cm$ (from Equations A.5 and A.9), good positional resolution of showers can be achieved, if steel planes of thickness close to that value are used. Also the hadrons (pions etc.) produced in neutrino interactions have an interaction length of $16.7cm$. MINOS steel planes are $2.54cm$ thick, and provide good separation between electron and hadron showers.

The critical energy for muons is E_{crit_μ} (Appendix A.3),

$$E_{crit_\mu} = 1314GeV \tag{3.6}$$

So muons which also have energies in the order of $1GeV$, lose energy by ionization mostly.

3.4.1 Charged Particle Signatures in MINOS

A minimum ionizing muon loses $\frac{1.49MeV}{gcm^{-2}}$, i.e., $\frac{33.2MeV}{plane}$. So, a $1GeV$ muon, is expected to have a track length of 30.1 *planes*.

Since the mean free path of pair production in iron is 2.26 *cm* and MINOS planes are 2.54 *cm* thick, electrons will produce pairs of photons in every plane, creating a cascading shower.

The interaction length for hadrons in iron is 6.0 *planes*. The hadrons produced in neutrino interactions will interact with the steel nuclei and give several other particles, collectively forming a shower.

In these calculations, the density of iron has been taken as $7.9gcm^{-3}$, the length

of a steel plane has been taken as $2.54cm$[27].

In summary charged particle signatures in the MINOS detectors are -

- muon - long track with track length proportional to the energy of the muon. Figure 3.11 shows a muon signature in MINOS.
- electron - electromagnetic shower with a mean free path of pair production of 1 plane. Figure 3.12 shows an electron signature in MINOS.
- hadron - hadronic shower with mean interaction length of 6.0 *planes*. Figure 3.13 shows a π^+ signature in MINOS.

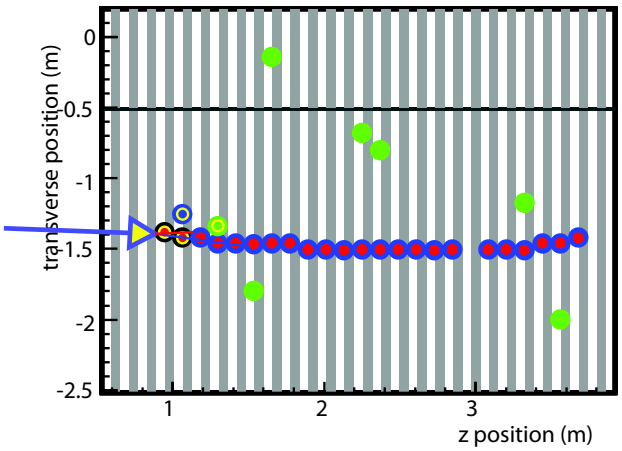

Figure 3.11: A muon signature in the MINOS detectors.

Such signatures make muons readily distinguishable from other possible particles in the MINOS detector, thereby making their parent particle, ν_μ, readily identifiable also.

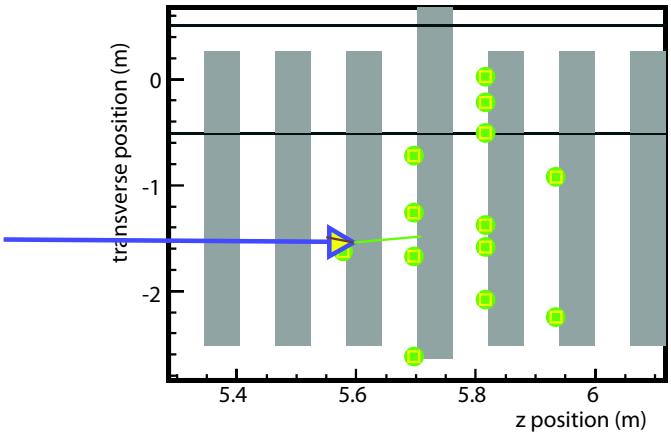

Figure 3.12: An electron in the MINOS detectors.

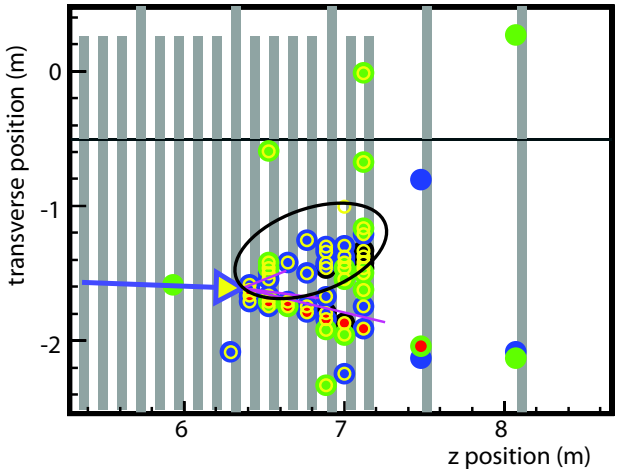

Figure 3.13: A hadron (π^+) in MINOS detectors. The circled area is the π^+.

Chapter 4

Event Selection and Reconstruction: a Monte Carlo Study

This chapter will describe studies on muon and neutrino momentum reconstruction. For this purpose a Monte Carlo generated neutrino sample has been used. All distributions shown in this chapter are for these Monte Carlo events.

4.1 Quasi Elastic Scattering Kinematics

For a quasi-elastic scattering, the neutrino energy can be determined by measuring the momentum and the angle of the resulting muon, if Fermi momentum is ignored. The kinematics of this process is discussed here.

A schematic of a neutrino, ν, scattering off a nucleon, N, at rest and giving a muon, μ, at angle of θ relative to the neutrino and other particles, X, is shown in Figure 4.1.

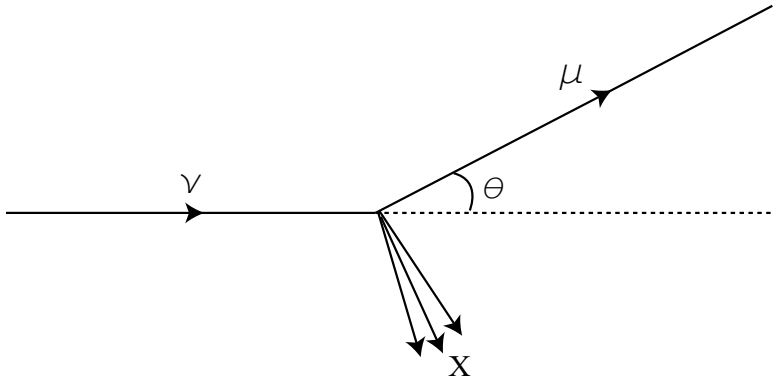

Figure 4.1: Charged current neutrino-nucleon interaction. Neutrino, ν, scatters off a nucleon, N, giving a muon μ and other particles, X.

$$p_\nu + p_N = p_\mu + p_X \text{ in 4 momentum} \tag{4.1}$$

$$\begin{aligned} p_\nu^2 + p_N^2 + p_\mu^2 + 2p_\nu p_N - 2p_\nu p_\mu - 2p_N p_\mu &= p_X^2 \\ m_N^2 + m_\mu^2 + 2E_\nu(m_N - 2E_\mu + |\vec{p_\mu}|cos\theta) - 2m_N E_\mu &= m_X^2 \end{aligned}$$

Assuming no Fermi momentum for N, $\vec{p_N} = 0$, $p_N = m_N$ and $m_\nu = 0$ and $|\vec{p_{nu}}| = E_\nu$,

$$E_\nu = \frac{2m_N E_\mu - m_\mu^2 - m_N^2 + m_X^2}{2(m_N - E_\mu + |\vec{p_\mu}|cos\theta)} \tag{4.2}$$

For QEL events in MINOS, where $\nu_\mu + n \rightarrow \mu^- + p$, since $X \equiv p$, $m_N = m_X = m_p = 0.9396\ GeV$,

$$E_\nu = \frac{2m_N E_\mu - m_\mu^2}{2(m_p - E_\mu + |\vec{p_\mu}|cos\theta)} \tag{4.3}$$

So, for QEL events, the neutrino energy is a function of only the muon momen-

tum, $\vec{p_\mu}$ and the angle of the muon with respect to the neutrino, θ.

4.1.1 Effects of Fermi Momentum

In the derivation of quasi-elastic kinematics above, it has been assumed that the target nucleon is at rest. In reality though, this nucleon has a finite momentum due to the effects of nuclear binding. This momentum known as the Fermi momentum, has a distribution given by [31] :

$$\begin{aligned} |\phi(\vec{p_N})|^2 &= \frac{1}{C}\left[1 - 6\left(\frac{K_F a}{\pi}\right)^2\right] \text{ for } 0 \leq |\vec{p_N}| \leq K_F \\ &= \frac{1}{C}\left[2R\left(\frac{K_F a}{\pi}\right)^2\left(\frac{K_F}{p_N}\right)^4\right] \text{ for } K_F \leq |\vec{p_N}| \leq 4\ GeV/c \\ &= 0 \text{ for } |\vec{p_N}| \geq 4\ GeV/C \end{aligned}$$

with $a = 2(\ GeV/c)^{-1}$, $C = \frac{4}{3}\pi K_F^3$, $R = 1/[1 - K_F/(4\ GeV/c)]$ and for iron the Fermi momentum, $K_F = 0.257\ GeV.c$.

The effects of not including Fermi momentum was studied using Monte Carlo simulations as shown in Figures 4.2 and 4.3. Figure 4.2 shows $\Delta p_\nu\ GeV$ (true p_ν-reconstructed p_ν without Fermi momentum) for different true neutrino energies. From this figure it can be seen that the reconstruction of the neutrino momentum without the Fermi momentum introduces smearing with an offset that is dependent on the neutrino energy and is on average about of $\sim 0.100\ GeV$. In these plots the Fermi momentum of the proton has been randomly assigned according to the Fermi distribution and the proton's angle with respect to the neutrino has been randomly assigned from a uniform distribution from $0 - 2\pi$.

Since I will use the muon momentum and the angle of the muon with respect to

the neutrino, to reconstruct the neutrino momentum via the quasi elastic equation, Equation 4.3, it is important to see what resolution of p_ν can be achieved. Figure 4.3 shows how p_μ varies with $cos\theta_\mu$ for different p_ν's. From that figure it can be seen that for larger angles (i.e., smaller $cos\theta_\mu$ values), p_ν is not well resolved. So for large recoil angles of the muon, the neutrino energy reconstructed without the Fermi momentum is smeared out. This prompts the need for a cut on the muon angle with respect to the neutrino. However, for this we also need to know the reconstructed muon momentum resolution and the angle resolution. The muon momentum resolution (as will be shown in Figure 4.21) is 0.04 GeV at 1σ. In Figure 4.3, the separation between muons resulting from a 2.0 GeV and 2.1 GeV neutrino is 0.04 GeV at $cos\theta = 0.7$. So an angle requirement of $cos\theta > 0.7$ was used in order to better resolve the reconstructed muon.

4.2 Event Reconstruction Overview

All charged particles that pass through the detector and lose energy are recorded via energy depositions within the scintillator strips. These energy depositions are known as 'hits'. The raw hits in both U and V views of the scintillator are analyzed together with timing information to construct "snarls". A "snarl" is a collection of hits that pass several triggers that include a four out of five plane trigger which requires that 4/5 contiguous planes have hits and a timing cut that requires that all hits be within 50 ns before and 500 ns after the earliest hit in the snarl. Theses snarls are again divided into spatially separated clusters of hits, known as "slices". If single strips are hit in adjacent planes and form a continuous line, they are classified as track-like. If multiple strips are hit in adjacent planes, they are classified as shower-like. An "event" is identified then, as a collection of tracks and showers clustered in time. This reconstruction mechanism results in multiple events per

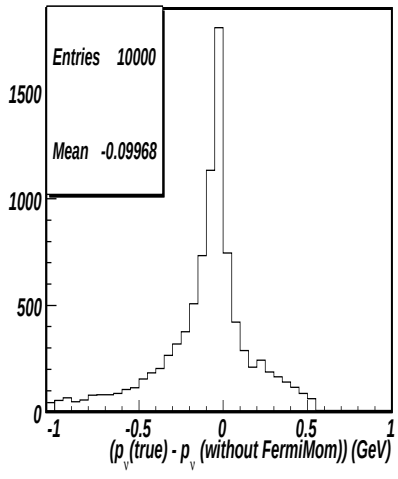

$p_\nu(true) = 1.0\ GeV$

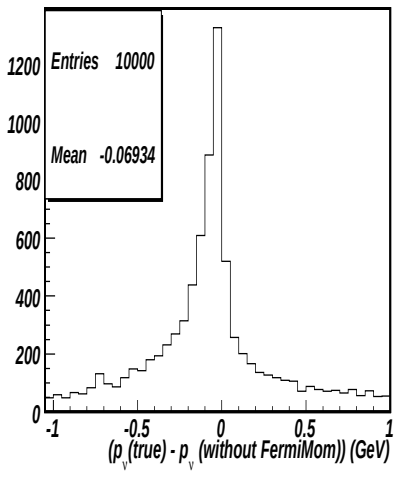

$p_\nu(true) = 2.0\ GeV$

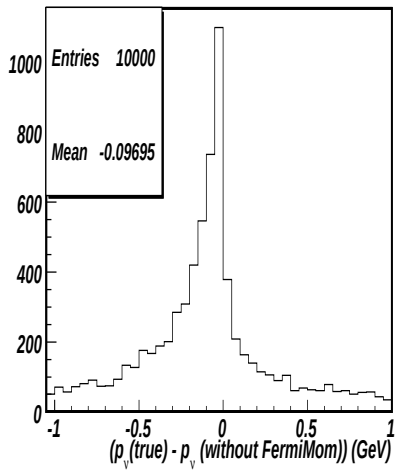

$p_\nu(true) = 3.0\ GeV$

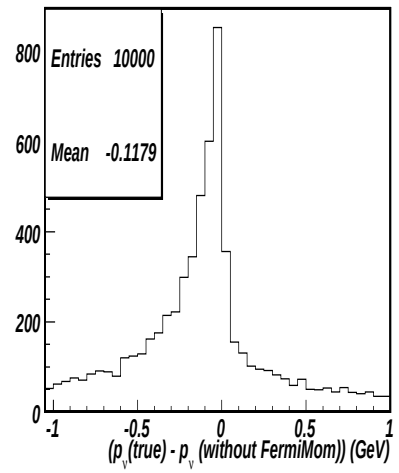

$p_\nu(true) = 5.0\ GeV$

Figure 4.2: Effects of Fermi momentum. Δp_ν(true-reconstructed without Fermi momentum) GeV for different true neutrino energies.

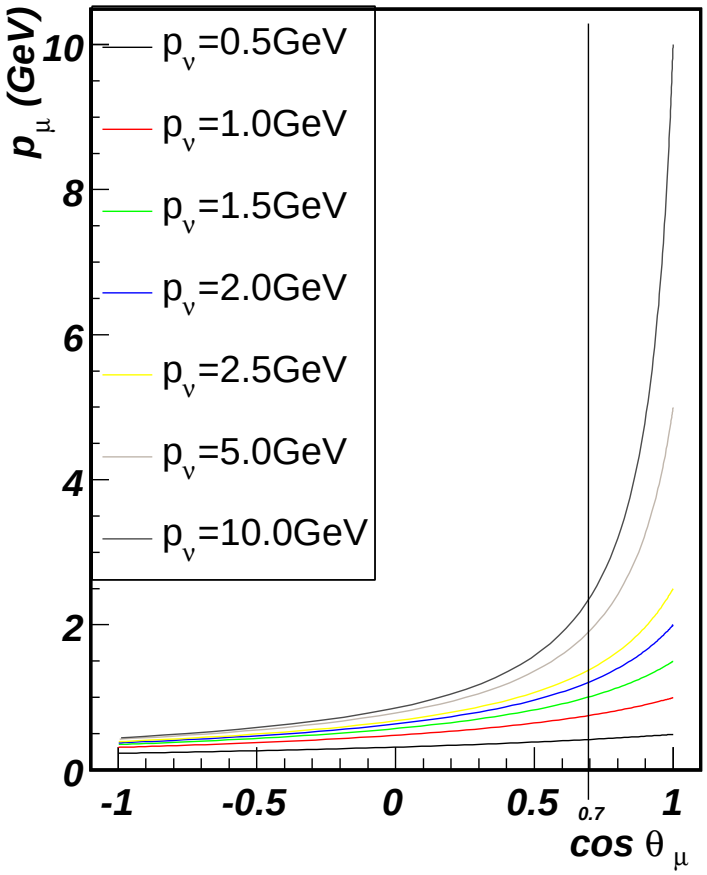

Figure 4.3: $p_\mu(GeV)$ vs $cos\theta_\mu$ for different neutrino momenta in GeV. Here the Fermi momentum of the target nucleus has not been accounted for when calculating the muon momentum, p_μ. As $cos\theta_\mu$ goes from -1.0 to 1.0, the resolution of the neutrino momentum decreases.

snarl in the Near Detector and mostly single (very rarely double) events per snarl in the Far Detector.

In general all hits that have an energy deposition corresponding to a pulse height of 2 photoelectrons or more are used in the event reconstruction. Since the main measurement in MINOS, the $\nu_\mu CC$ interaction, is identified by a muon track, the reconstruction is optimized for tracks. Any hit that has a pulse height of 2 photoelectrons or more and does not get reconstructed as part of a track will likely be incorporated into a shower; so that delta rays produced along the muon track are sometimes reconstructed as showers. Also, sometimes, the high energy deposit (pulse height) of a recoil proton is reconstructed as a shower. When muons reach low energies near the end of their track, their rate of energy loss by ionization, $\frac{dE}{dx}$ increases rapidly thereby depositing a lot of energy that can sometimes be reconstructed as a shower at the end of the track. 'Showers' in all the above three cases is a MINOS specific term and does not refer to hadronic or electromagnetic showers, but merely refers to a collection of hits in space and time as described before. Retaining this hit information in the form of showers is important for establishing the neutrino energy in the main MINOS analysis, where the neutrino energy is reconstructed by summing the track and shower energies. The QEL analysis discussed in this thesis however, does not use shower energy in the reconstruction of the parent neutrino energy.

4.3 Muon Momentum Reconstruction

As previously described in Section 3.4.1, a muon resulting from a neutrino interaction in the MINOS steel is readily identifiable via the long track it creates. These tracks are reconstructed from individual pulses of energy deposition by the muon as it loses energy via ionization in the active detector. A detailed description of track

reconstruction is given in Reference[27]. Once the track is reconstructed, the muon momentum, p_μ, is reconstructed from its range in the detector by integrating over the Bethe-Bloch formula and also from curvature in the magnetic field as explained in Section 3.3.

4.3.1 Muon Momentum Reconstruction: Range vs Curvature

Ideally, the reconstructed $p_\mu(range) = p_\mu(curvature)$. But for the few muons that escape the detector from the edges, the range measurement can not be used and the curvature measurement has to be used. Due to uncertainties in the magnetic field maps $p_\mu(curvature)$ is used with caution.

4.3.1.1 Far Detector

In order to determine which p_μ measurement to use, whether from range or curvature, Monte Carlo generated $\nu_\mu CC$ events were studied and p_μ reconstructed using both range and curvature were compared to the true p_μ for different fiducial criteria. Figures 4.4 and 4.5 show how $\Delta p_\mu = p_\mu(reco) - p_\mu(true)$ varies with the track end point, specifically along the detector axis, Z, and along the radial direction of the detector.

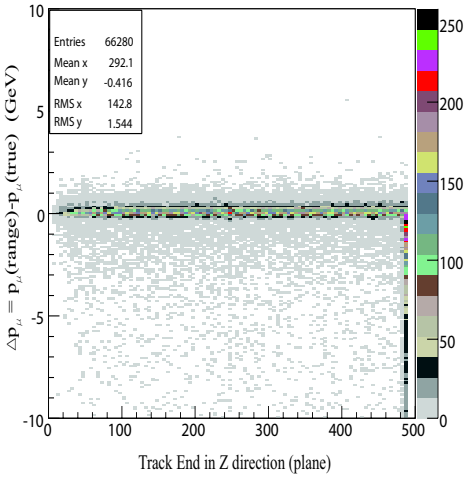

$\Delta p_\mu(range - true)$ vs track end z

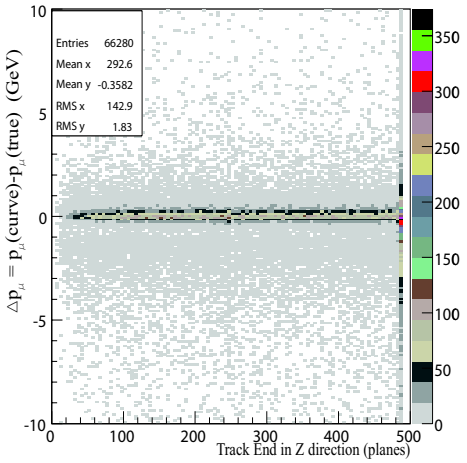

$\Delta p_\mu(curve - true)$ vs track end z

Figure 4.4: The above plots are a first look into the agreement between reconstructed p_μ and true p_μ in the Far Detector. The left plot displays $p_\mu(range)$ and the right plot displays $p_\mu(curvature)$ information. The $p_\mu(range)$ measurement has better resolution than that of $p_\mu(curvature)$, but both fail for tracks that go beyond the detector edges.

From Figure 4.4 which shows Δp_μ vs track end along detector axis, since the range measurement is in better agreement with the true muon momentum, for tracks that end before the 481^{st} plane, the momentum by range will be used and for the others, if $\frac{\sigma(curvature)}{curvature} < 0.1$, the measurement from curvature will be used. Here $\sigma(curvature)$ is calculated from uncertainties in the the magnetic field maps and track fitting. Figure 4.5 which shows Δp_μ vs track end in radial direction shows no abrupt increase in the momentum resolution at specific radial distances, so there will not be a cut based on the track end in r. For the track vertex, I will use a standard

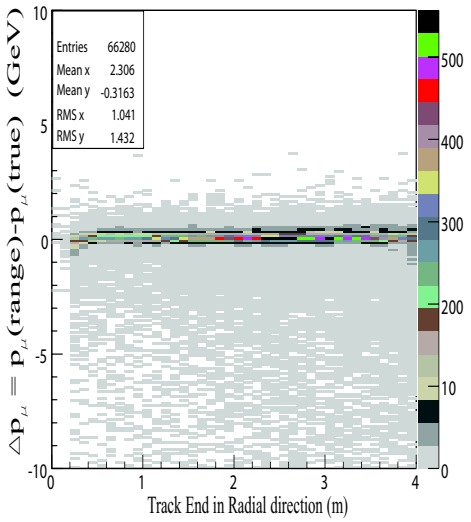

$\Delta p_\mu(range - true)$ vs track end r

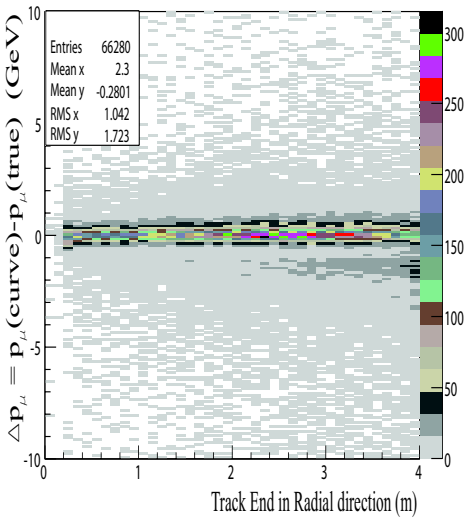

$\Delta p_\mu(curve - true)$ vs track end r

Figure 4.5: A first look into the agreement between reconstructed p_μ and true p_μ in the Far Detector. The left plot displays $p_\mu(range)$ and the right plot displays $p_\mu(curvature)$ information. The $p_\mu(range)$ measurement has better resolution than that of $p_\mu(curvature)$.

fiducial cut of $0.5m \leq$ track vertex z $\leq 14.5m$, $16.5m \leq$ track vertex z $\leq 29.4m$ and $0.4m \leq$ track vertex r $\leq 3.5m$ to avoid detector edges and coil hole.

The agreement between the reconstructed muon momentum and true muon momentum after the above mentioned selection cuts, is shown in Figure 4.6. The muon momentum reconstructed with the above mentioned selection cuts yields a smaller deviation from the true momentum, than the range and the curvature measurements separately. Appendix B.1 shows the muon momentum by range and curvature separately for these same events.

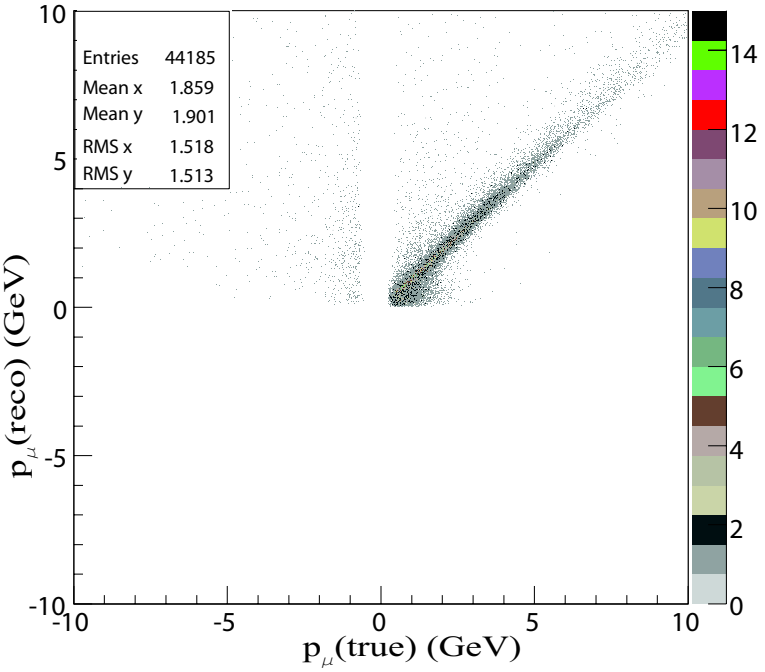

Figure 4.6: $p_\mu(true)$ vs $p_\mu(reco)$ for all true ν_μ events that interact via the CC interaction in the Far Detector. The p_μ reconstruction is obtained as follows: if the tracks end before the 481^{st} plane, the momentum by range has been used; for tracks ending at and beyond the 481^{st}plane, if $\frac{\sigma(curvature)}{curvature} < 0.1$, the measurement from curvature will be used.

4.3.1.2 Near Detector

As in the Far Detector, a Monte Carlo $\nu_\mu CC$ event sample was studied and p_μ reconstructed using range and curvature were compared to the true p_μ for different fiducial criteria. Figures 4.7 and 4.8 show how $\Delta p_\mu = p_\mu(reco) - p_\mu(true)$ varies with the track end point.

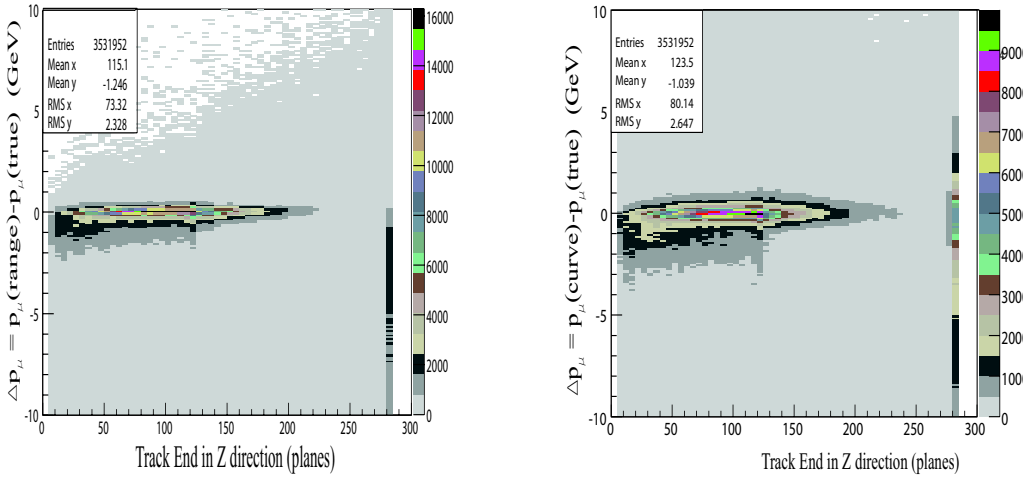

$\Delta p_\mu(range - true)$ vs track end z $\Delta p_\mu(curve - true)$ vs track end z

Figure 4.7: A first look into the agreement between reconstructed p_μ and true p_μ in the Near Detector. The left plot displays $p_\mu(range)$ and the right plot displays $p_\mu(curvature)$ information. The $p_\mu(range)$ measurement has better resolution than that of $p_\mu(curvature)$, but both fail for tracks that go beyond the detector edges.

It is seen in Figure 4.7 which shows Δp_μ vs track end along detector axis, that again, the range measurement is in better agreement with the true muon momentum, for tracks that end before the 280^{th} plane. But since the Near Detector has high statistics and in the spectrometer end the detector is instrumented only 1 in 5 planes,

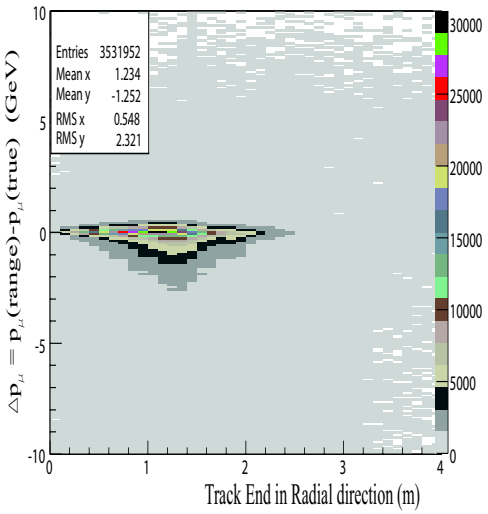

$\Delta p_\mu(range - true)$ vs track end r

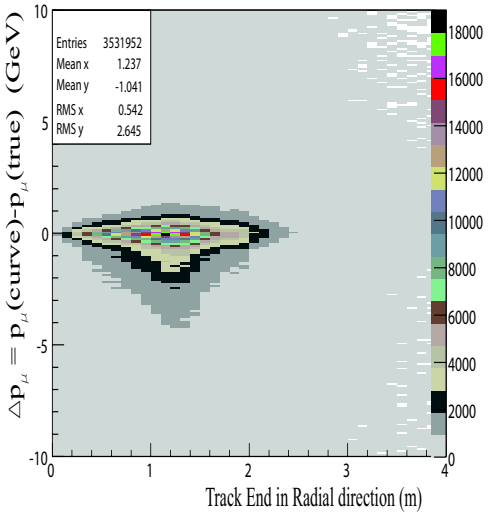

$\Delta p_\mu(curve - true)$ vs track end r

Figure 4.8: The above plots are a first look into the agreement between reconstructed p_μ and true p_μ in the Near Detector. The left plot is for $p_\mu(range)$ and the right plot is for $p_\mu(curvature)$. The $p_\mu(range)$ measurement has better resolution than that of $p_\mu(curvature)$.

I will make a conservative cut at plane 275. So for tracks that end before the 275^{th} plane, the momentum by range will be used and for the others, if $\frac{\sigma(curvature)}{curvature} < 0.1$, the measurement from curvature will be used. Again Figure 4.8 which shows Δp_μ vs track end in radial direction offers no good radial cut, so there will not be a cut on the radial position of the track end. For the track vertex, I will use a standard fiducial cut of $1.0m \leq$ track vertex along Z $\leq 5.0m$ track vertex along radial $\leq 1m$, to avoid calorimeter edges and coil hole.

The agreement between the reconstructed muon momentum and true muon momentum, after the above mentioned selection cuts, is shown in Figure 4.9. Even though less pronounced than the Far Detector, the muon momentum reconstructed with the above mentioned selection cuts yields a smaller deviation from the true momentum, than the range and the curvature measurements separately.

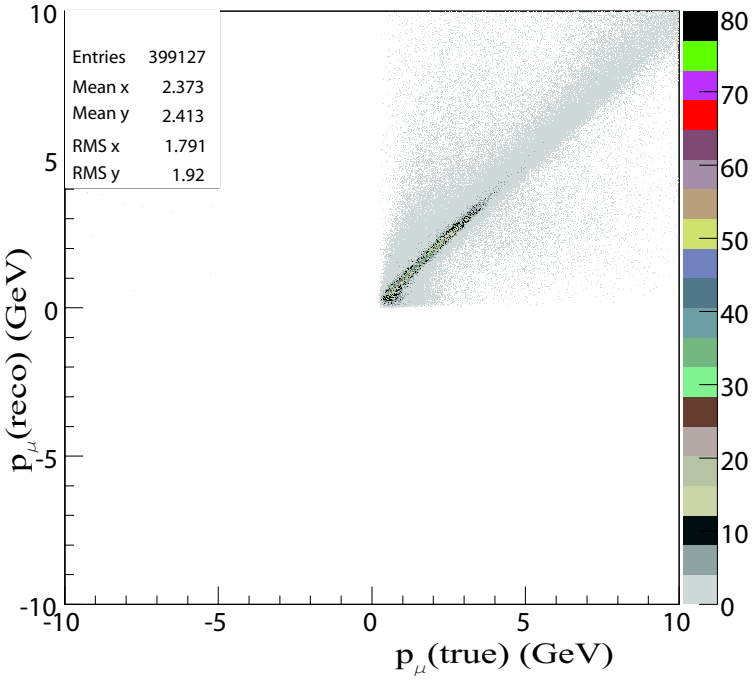

Figure 4.9: $p_\mu(true)$ vs $p_\mu(reco)$ for all true ν_μ events that interact via the CC interaction in the Near Detector. The p_μ reconstruction is obtained as follows: if the tracks end before the 275^{th} plane, the momentum by range has been used; for tracks ending at and beyond the 275^{th}plane, if $\frac{\sigma(curvature)}{curvature} < 0.1$, the measurement from curvature will be used.

4.4 Separation of Quasi Elastic Events

In this section I will outline my study of Monte Carlo simulations to establish a method to separate QEL events.

Before selecting the QEL events I separate the CC events from the NC events as described in Reference [32] (A very brief summary of this method is given in Appendix B.2). Then I study that sample to separate QEL events.

As shown in Section 1.1, QEL events ($\nu_\mu + n \rightarrow \mu^- + p$), in which the resulting particles are just a muon and a proton should be, in theory, easy to separate by looking for just two tracks: the muon track and the proton track. But this is not the case in the MINOS detectors. The steel-scintillator-sandwich design allows detection of the muon track, but the proton resulting from the QEL event is of low energy so that it goes no more than a couple of planes before it loses all its energy via ionization. For example a proton of momentum 0.2 GeV, goes only about 2 planes, in the MINOS detector. As such, looking for a proton track of finite length is impractical.

But since the protons deposit all of their energy within a short distance, looking for a high energy deposit near the vertex of the muon track may be a good way to identify the QEL proton.

QEL events produce no other hadrons other than protons, so there are no hadronic showers from the resulting particles. But not all events without showers are QEL events as seen in Figure 4.10, which shows the total shower breakdown for a sample of events. Low energy RES and DIS events also have no reconstructed showers. But it is virtually impossible to differentiate these events from QEL events, so I will treat them as QEL events.

Also as discussed before, delta rays along the muon track are sometimes reconstructed as showers in MINOS. So simply requiring that the selected sample of

events will have no showers, will not yield all the QEL events (see Section 4.2). Among events that have showers, QEL events can be separated from RES and DIS events by requiring these showers to be a cluster of only a few hits and also requiring them to be further downstream from the muon track vertex. This will separate QEL events from the RES and DIS events that have hadronic showers that occur close to the muon track vertex and are usually clusters of many hits.

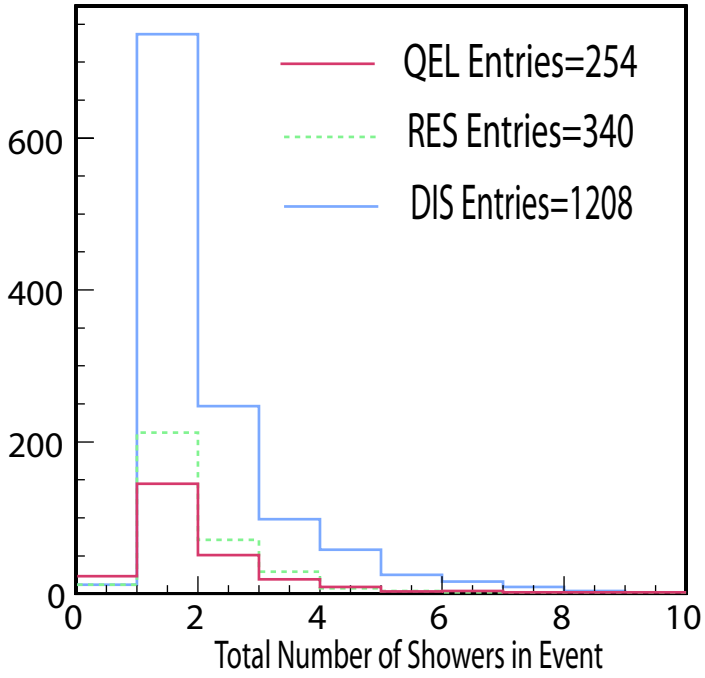

Figure 4.10: Number of showers in all events, based on if they are QEL, RES or DIS events.

With the above in mind, I separated the QEL-like events as follows - in my

Monte Carlo sample, I first took all events with no showers to be QEL-like. Out of the events with one or more showers, I discarded the events with more than one shower, because using more shower reconstruction information defeats the original idea of using only the more complete track reconstruction information to reconstruct the neutrino energy. I then picked several variables, described in Section 4.4.1, that would best distinguish QEL events from non-QEL events in events that have one shower and created probability distribution functions (pdf's) for each one of them based on if they are QEL, RES or DIS. This procedure is described in more detail and examples in Section 4.4.2.

4.4.1 Variables used for QEL separation

The variables used to separate QEL-like events (for events with one shower) are listed below. They are illustrated in Figure 4.11.

1. Distance between the shower vertex and the track vertex: for delta ray induced showers, this distance will be large

2. Distance between shower vertex and end of track: to distinguish delta rays from muons losing large amounts of energy that are reconstructed as showers, towards the end of the track

3. Number of hits in shower: for delta rays and protons reconstructed as showers, this number will be low

4. Maximum pulse height in the event within first five planes of the track vertex : this essentially looks for the proton, which is usually of low momentum so will deposit a large amount of energy

5. Total pulse height in shower: for delta rays and protons reconstructed as showers, this number will be relatively low, compared to DIS events' hadronic showers

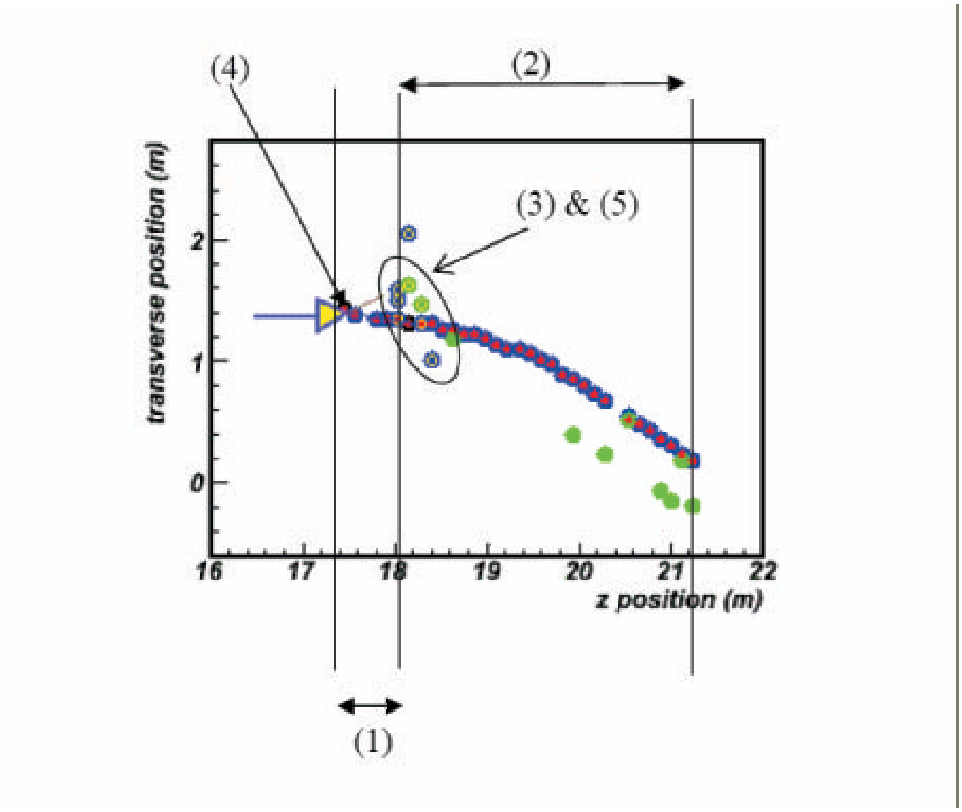

Figure 4.11: A graphical representation of the variables used for the QEL-like event separation. The numbers on the figure correspond to the different variables in Section 4.4.1.

4.4.2 Procedure for QEL separation : Far Detector

The five pdf's corresponding to the five variables listed in Section 4.4.1 are shown in Figure 4.12. For ideal separation, QEL and non-QEL should peak at either ends of a given histogram. But as can be seen, this is not the case and the separation is not very good.

Out of the variables shown in Figure 4.12 maximum pulse height in first five planes (Figure 4.12-4) and specially number of hits in shower (Figure 4.12-3) and total pulse height in shower (Figure 4.12-5) show reasonable separation. Even though it seems appropriate to make a cut based solely on the total shower pulse height (4.12-5) and the number of hits in the shower (4.12-3), and this would yield a high level of purity, a lot of QEL events will be discarded by this method, thereby reducing the efficiency. For example those events that give high energy protons that give several hits and energetic delta rays, will have a high number of shower hits and will not be selected by a low shower hits cut. These same events will escape a low shower pulse height cut. The maximum purity and corresponding efficiency values for these two variables are (64%,25%) for shower hits and (54%,53%) for total shower pulse height. Here purity and efficiency are defined as in Equations 4.5 and 4.5.

$$Purity = \frac{\text{selected QEL}}{\text{selected QEL + selected non-QEL}} \tag{4.4}$$

$$Efficiency = \frac{\text{selected QEL}}{\text{All QEL}} \tag{4.5}$$

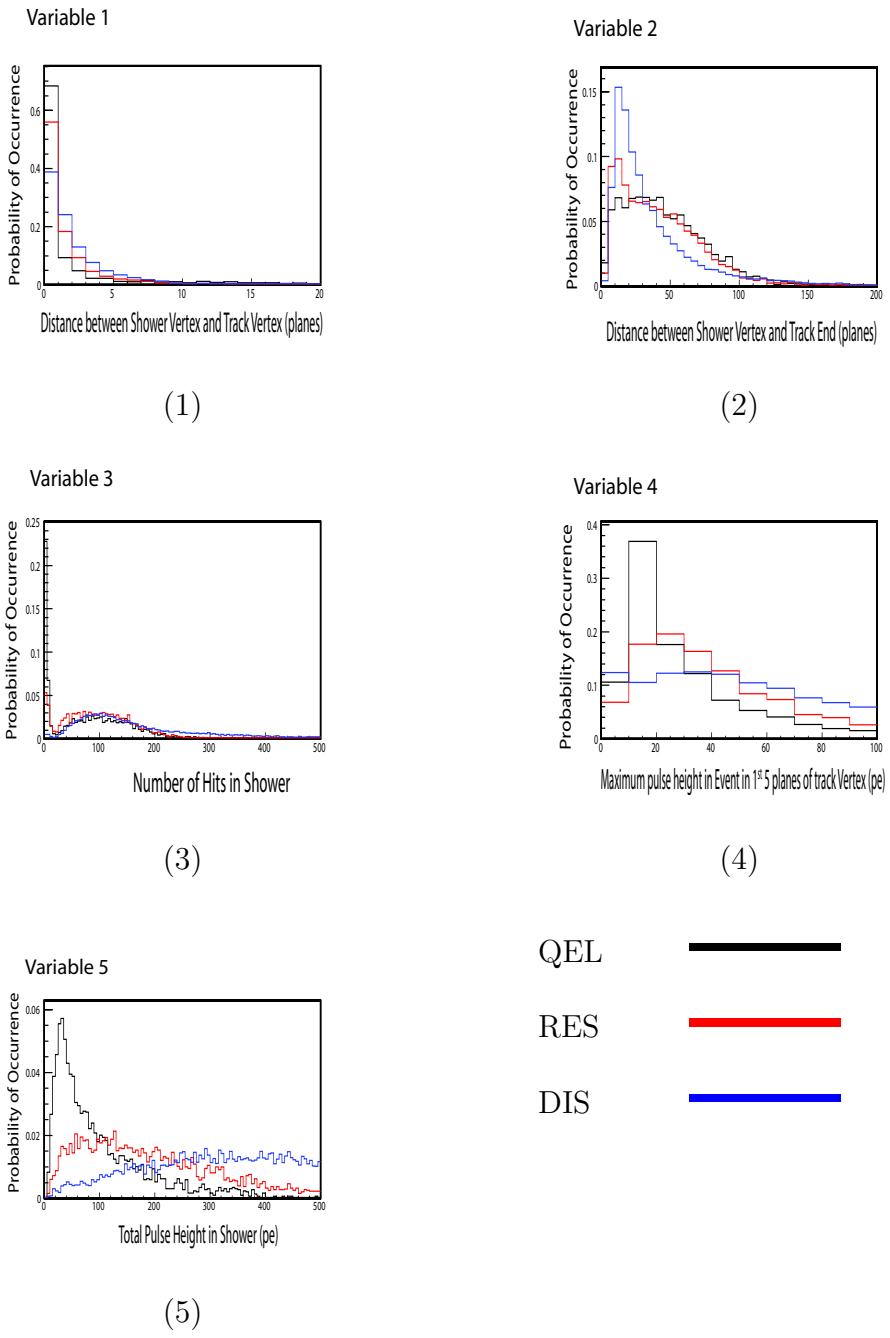

Figure 4.12: Probability distribution functions for variables listed in Section 4.4.1 for the Far Detector. The QEL are in black, the RES are in red and the DIS are in blue. For ideal separation QEL and non-QEL should peak at separate ends of the histogram.

So instead of cuts on individual variables, which don't work very well, it is important to look at these variables relative to each other. To best maintain this relationship between variables, I have used two dimensional probability distribution functions, in essence two-fold combinations of the variables listed in Section 4.4.1. That is on an event by event basis the probability of two variables occurring simultaneously was used to define a new particle identification parameter (PID). This method yields efficiencies significantly higher than the single variable cut.

The total MC sample is taken and divided into two and the first half is used to create these pdf's. For every two variable combination, the events are classified into their QEL, RES or DIS status and the distribution of the relevant two variables is plotted. These plots are then normalized to unity, thereby yielding the pdf's. This yields three different pdf's for the three types of events, QEL, RES and DIS, for each two variable combination from Section 4.4.1.

The second set of Monte Carlos were then used to calculate the probability of every event being either a QEL, RES or DIS. This was done by getting the values of the two variables pertaining to a given set of pdf's and checking their probabilities against the three pdf's for QEL, RES and DIS. Each of these probabilities denoted by q_i, r_i and d_i respectively, were combined as shown in Equation 4.6 to obtain a particle identification parameter (PID). When an n number of two dimensional pdf's are used for the separation, for the i^{th} event,

$$PID_i = \mathscr{L}_i = ln \prod_{j=1}^{n} \left(\frac{r_{ij} d_{ij}}{q_{ij}^2} \right) \tag{4.6}$$

This PID is then plotted separately for true QEL, RES and DIS events, similar to that shown in Figure 4.14.

Once a PID plot is made for a combination of n two-dimensional probabilities, a sliding cut is applied to find out the PID cut that will yield the best selection

of QEL events. Here the best selection is determined by the cut that maximizes a figure of merit (FOM) defined as shown in Equation 4.7.

$$FOM = \frac{(\text{selected QEL})^2}{\text{selected QEL} + \text{selected non-QEL}} \tag{4.7}$$

This is done for all combinations of n two-dimensional probabilities and the maximum FOM values for each n combination is compared to decide how many such two dimensional pdf's should be combined and also to decide which combinations to use.

This study showed that the following three two-dimensional pdf's yielded the highest FOM, where FOM as defined by Equation 4.7 is a measure of how pure a QEL sample can be selected and with what efficiency it could be done. These pdf's are shown in Figure 4.13.

1. Distance between the shower vertex and the track vertex vs Total pulse height in shower

2. Distance between shower vertex and end of track vs Total pulse height in shower

3. Number of hits in shower vs Maximum pulse height in the event within first five planes of the track vertex

The PID is then defined as in Equation 4.6 for just these three (instead of n) variables as,

$$PID_i = \mathscr{L}_i = ln \prod_{j=1}^{3} \left(\frac{r_{ij} d_{ij}}{q_{ij}^2} \right) \tag{4.8}$$

The PID calculated from Equation 4.8 using these three two-dimensional variables only, are plotted separately for the QEL, RES and DIS events as shown in Figure 4.14. This was the final PID that was used in the QEL event separation.

As can be seen from Figure 4.14, there is apparently poor separation between QEL and non-QEL events. But when the contaminating non-QEL events are scanned, it is seen that they look very much like QEL events, with a single track from the muon and no hadronic shower. Examples of such events are shown in Figure 4.15 (contaminating RES events), and Figure 4.16 (contaminating DIS events).

The FOM was maximized at a PID cut of 0.0. That is, the optimum purity-efficiency combination for selecting the QEL like events occurs when events with $PID < 0.0$ is taken as QEL-like events. With this cut QEL events were selected with a purity and efficiency of 48% and 88% respectively.

This combination of two-fold pdf's is more efficient than the single variable cuts as mentioned before. For example, QEL events with high momentum protons like that shown in Figure 4.18 and QEL events with energetic delta rays along the muon track like that in Figure 4.17, that would have not been selected by single cuts, are selected by this method.

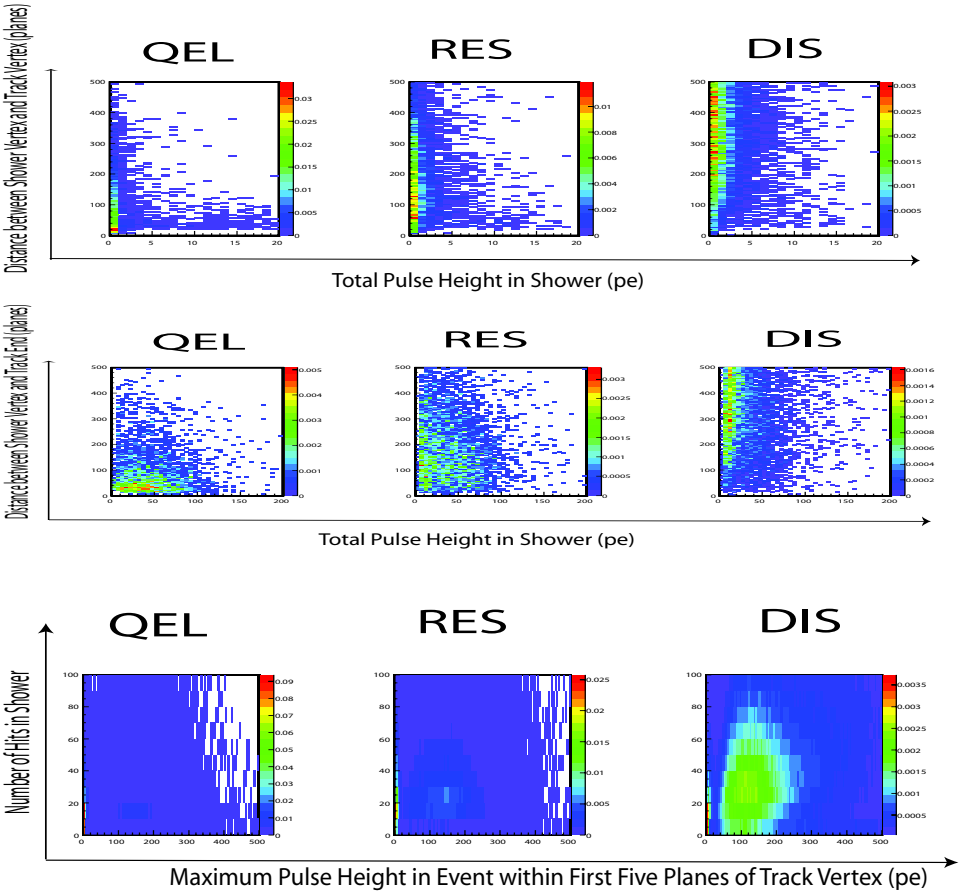

Figure 4.13: Probability distribution functions for two-fold combinations of variables listed in Section 4.4.2 for the Far Detector. The QEL, RES and DIS are in the left, middle and right columns respectively. For ideal separation QEL and non-QEL should peak at separate quarters in each histogram.

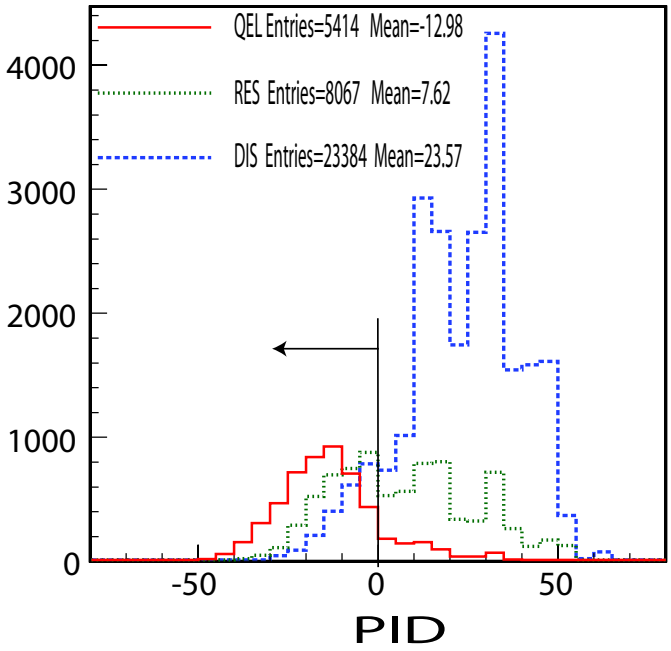

Figure 4.14: PID for true QEL (red), RES (green) and DIS (blue) events in the Far Detector. Here the PID is defined in Equation 4.8. This is for a combination of three two dimensional probabilities, the ones named in Section 4.4.2

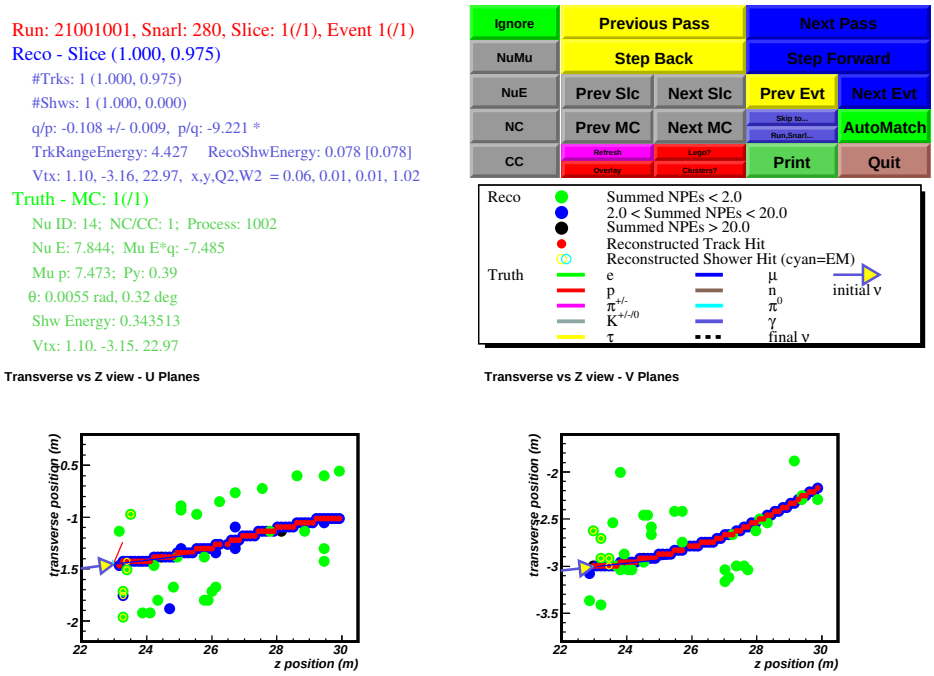

Figure 4.15: A RES event that looks very much like a QEL event.

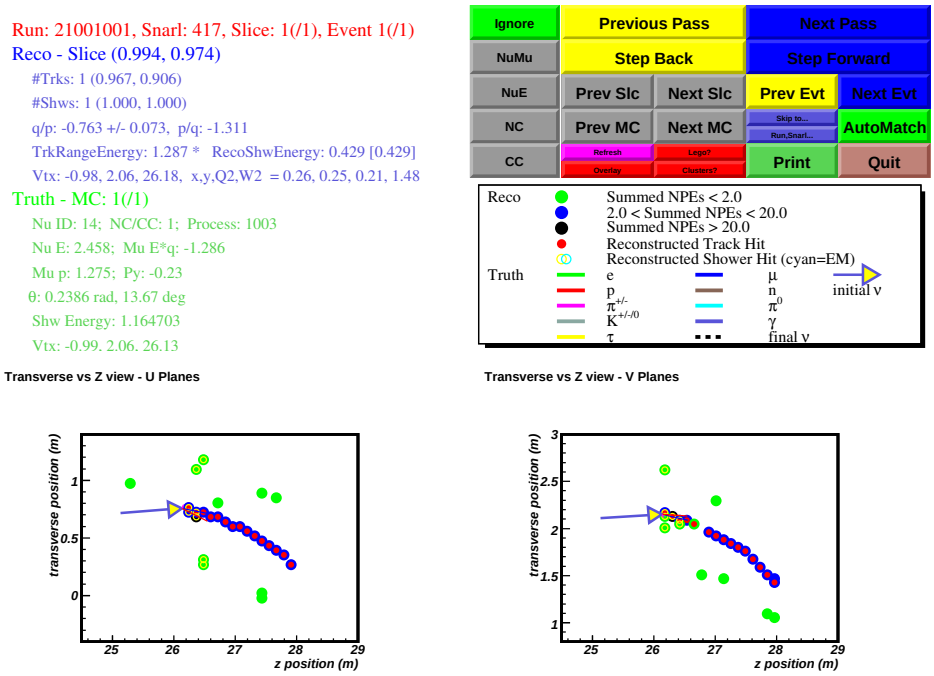

Figure 4.16: A DIS event that looks very much like a QEL event.

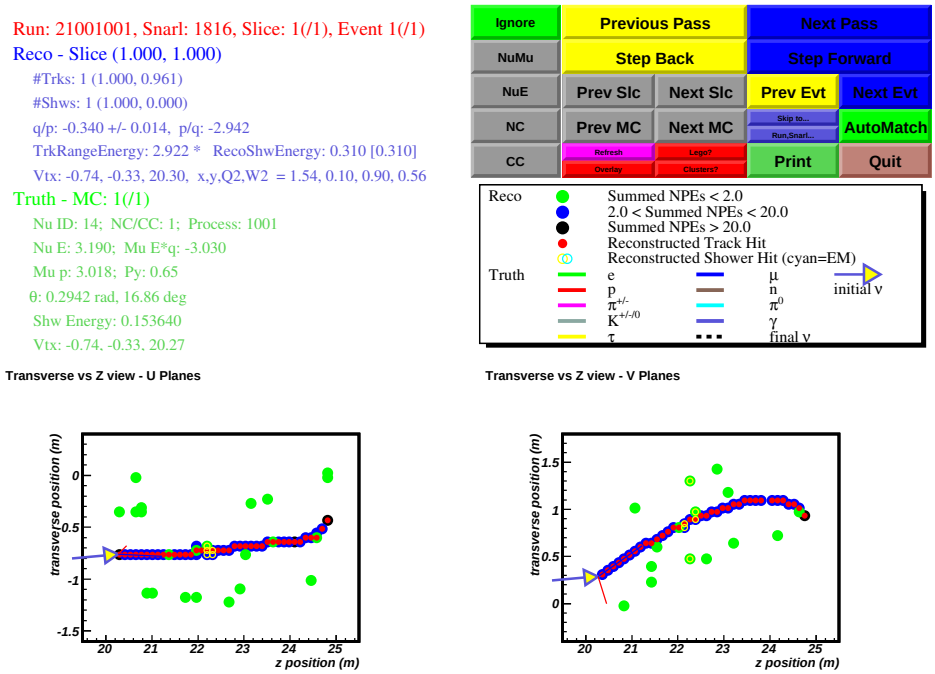

Figure 4.17: A QEL event with a delta-ray reconstructed as a shower. The yellow circles in the middle of the track represents this non-hadronic-delta-ray-shower. This event has 159 non-track-hits and a total shower pulse height of 91 $pe's$, so this would have been discarded by a number of hits in shower or total shower pulse height only cut. As can be seen from Figure 4.12 a good QEL event has showers with less than ten hits and less than 80 $pe's$ of pulse height. But the distance to the shower vertex from the vertex and the end of the track are 31 *planes* and 45 *planes* respectively. These two values separately combined with the total shower pulse height, makes the biggest contribution to the PID parameter of -32, which, with the current cut of $PID < 0.0$, safely filters in as a QEL event. The proton in this event has a momentum of 0.6 GeV and the single hit from the proton is along the muon track.

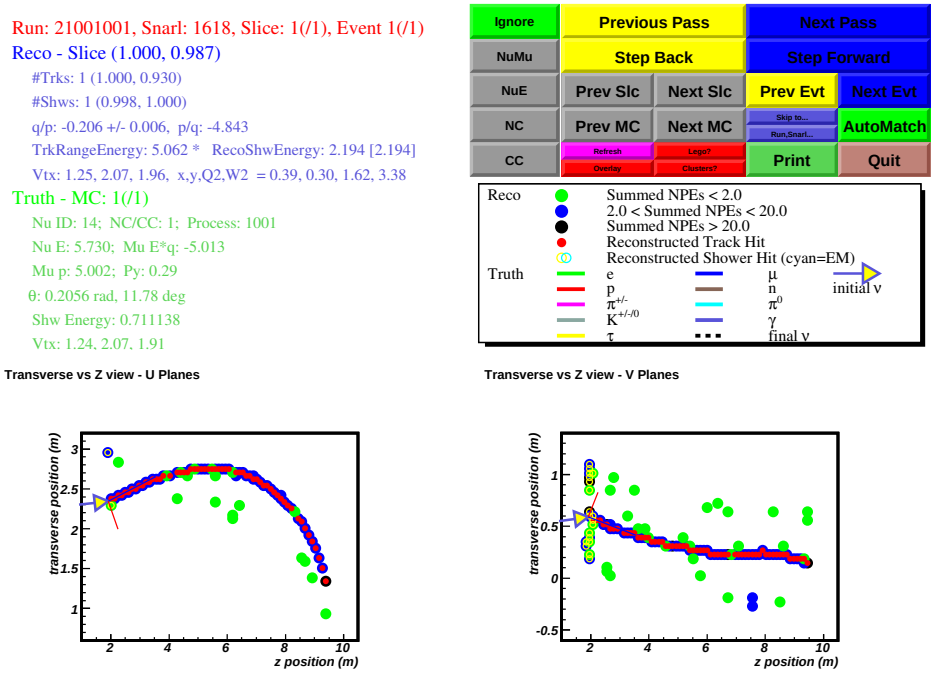

Figure 4.18: A QEL event in which a high momentum recoil proton (1.4GeV) is reconstructed as a shower. The yellow circles at the beginning of the track represents this non-hadronic-shower. This event has 260 non-track-hits and a total shower pulse height of 345 $pe's$, so this would have been discarded by a number of shower hits < 10 or total shower pulse height < 80 pe only cut. But taken together, these two variables provide a pulse height per hit like variable which makes the biggest contribution to the PID parameter of -34, which with the current cut of $PID < 0.0$, safely filters in as a QEL event. The proton in this event enters the scintillator plane and goes about $0.5m$, because of the low density of the scintillator material.

4.4.2.1 Procedure for QEL Event Selection : Near Detector

For consistency, the Near Detector is treated identically to the Far Detector. The same variables (Section 4.4.2) were used to make two dimensional pdf's and the PID parameter was defined in the same manner (Equation 4.8). The one dimensional pdf's for the QEL events from the RES and the DIS is shown in Figure 4.19. The PID values plotted for the QEL, RES and DIS separately, are shown in Figure 4.20. Also, the PID cut was selected such that the Near Detector QEL selection would yield the same (or close) purity and efficiency that the Far Detector, with priority given to the purity. At the PID cut chosen for the Near Detector, $PID < -6$, the purity and efficiency of selecting QEL events was 50% and 71%, respectively. This compared to 48% and 88% in the Far Detector. Since the Near Detector has a lot more events than the Far Detector, it is acceptable to select QEL events at an efficiency lower than that in the Far Detector.

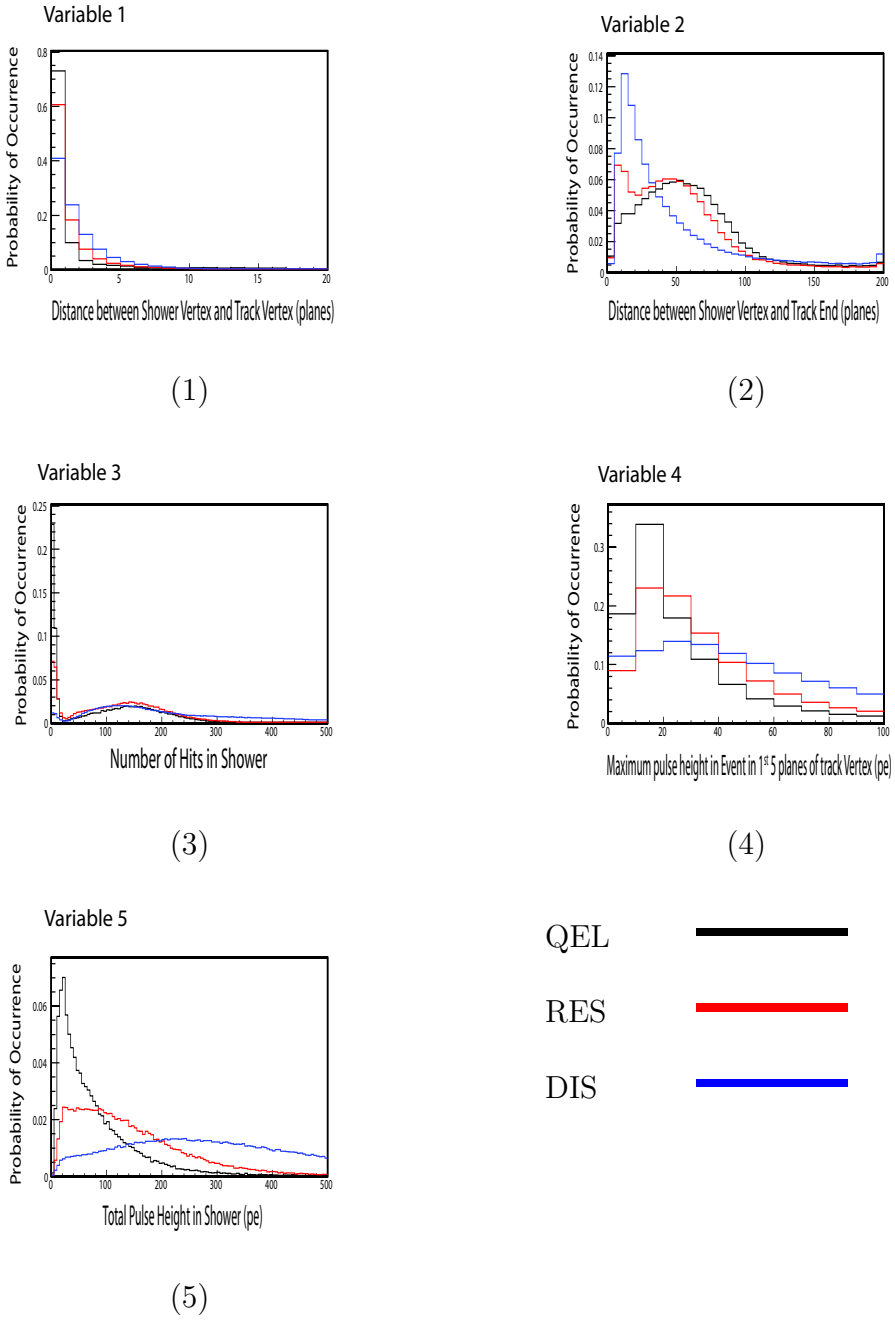

Figure 4.19: Probability distribution functions for variables listed in Section 4.4.1 for the Near Detector. The QEL are in black, the RES are in red and the DIS are in blue. For ideal separation QEL and non-QEL should peak at separate ends of the histogram.

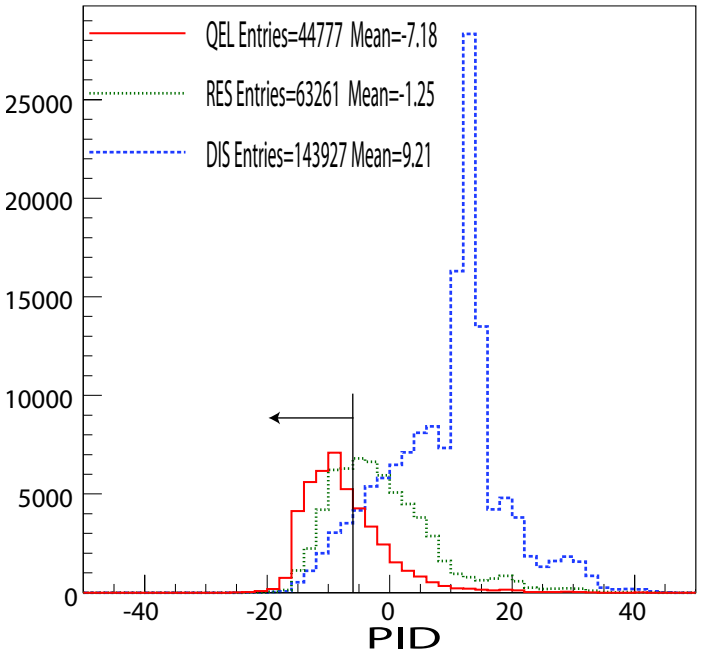

Figure 4.20: PID for true QEL (red), RES (green) and DIS (blue) events in the Near Detector. Here the PID is defined in Equation 4.8. This is for a combination of three two dimensional probabilities, the ones named in Section 4.4.2

4.5 Momentum Reconstruction for QEL-like-selected Events

The QEL-like events were selected as outlined in Sections 4.4.2 and 4.4.2.1. Hereafter these will be referred to as 'QEL-like-selected events'. It should be reiterated that not all these QEL-like-selected events are truly QEL events, only events that filtered through my selection.

In this Section I will compare the muon and neutrino momentum reconstructions for the Near and the Far detectors.

All events were those that filtered through a fiducial function determined by the track vertex as discussed before. Also imposed were the cuts of $0.5\ GeV < p_\mu$ (reconstructed and true), $0.\ GeV < p_\nu < 10.\ GeV$ and $cos\theta > 0.7$ where θ is the muon angle with respect to the neutrino.

Depending on the location track end either the range or curvature measurement was used to determine the muon momentum. For the Near Detector, if track end $< 275 planes$ the range was used, otherwise if $\frac{\sigma_{curvature}}{curvature} < 0.1$ the curvature measurement was used. For the Far Detector, if track end $< 481 planes$ the range was used, otherwise if $\frac{\sigma_{curve}}{curve} < 0.1$ the curvature measurement was used.

4.5.1 p_μ Reconstruction for QEL-like-selected events

All Monte Carlo events that satisfy the fiducial criteria described in Section 4.3 and pass the PID cuts determined in Sections 4.4.2 and 4.4.2.1, were used in this study. The quantity $\Delta p_\mu = p_\mu(true) - p_\mu(reco)$ was plotted for all these QEL-like-selected events and this is shown in Figure 4.21. It is seen that the Near and far detectors have similar distributions.

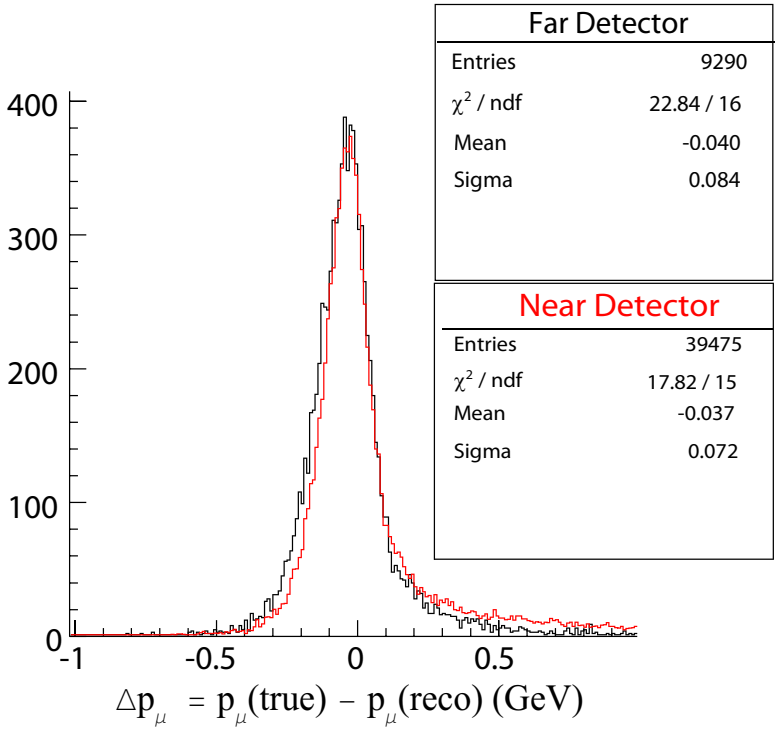

Figure 4.21: $\Delta p_\mu = p_\mu(true) - p_\mu(reco)$ for all selected events, i.e., QEL-like events filtered through the fiducial volume and the PID's discussed in Sections 4.3, 4.4.2 and 4.4.2.1. Monte Carlo for Near and Far Detectors are in red and black respectively. The Near Detector is normalized to the same number of events filtered in the Far Detector.

4.5.1.1 Uncertainties Involved in the p_μ Reconstruction

In the Near and Far Detectors, for 96% and 95% of selected events respectively, the muon momenta were reconstructed using the range measurement. As such, it is noteworthy to look at the uncertainty in the momentum measurement by range.

The main contributions to the uncertainty in the range measurement comes from three things, namely, the uncertainty in determining the track vertex, the uncertainty in determining the track end and that from "straggling", which is due to fluctuations in ionization losses.

The $2.54cm$ thickness of the steel plates, introduces some uncertainty in determining the exact positions of both track vertex and end. This in turn affects the range measurement of the muon thereby introducing an uncertainty to the momentum measurement by range. This becomes especially important in the case of the track end, due to $\frac{dE}{dx}$ increasing rapidly at low energies, near the end of the muon range. This is illustrated in Figure 4.22.

In all the following calculations, the density of iron, steel plate thickness and energy loss by a minimum ionizing particle in iron has been taken to be 7.85 gcm^{-3}, $2.54cm$[27] and $\frac{1.45\ MeV}{gcm^{-2}}$[28] respectively.

4.5.1.1.1 Momentum Uncertainty from Track Vertex

For the track vertex the muon is minimum ionizing, so the energy loss per plane is,

$$\sigma_{vertex} = 2.54cm \times 7.85\ gcm^{-3} \times \frac{1.45\ MeV}{gcm^{-2}} = \frac{29.0\ MeV}{plane} \tag{4.9}$$

This gives uncertainty in momentum from the track vertex, σ_{vtx} [1],

[1] for a square (continuous, step-like) function $\bar{x} = \frac{\int_0^1 x dx}{\int_0^1 dx} = \frac{1}{2}$ and $\sigma^2 = \frac{\int_0^1 (\bar{x}-x)^2 dx}{\int_0^1 dx} = \frac{1}{\sqrt{12}}$

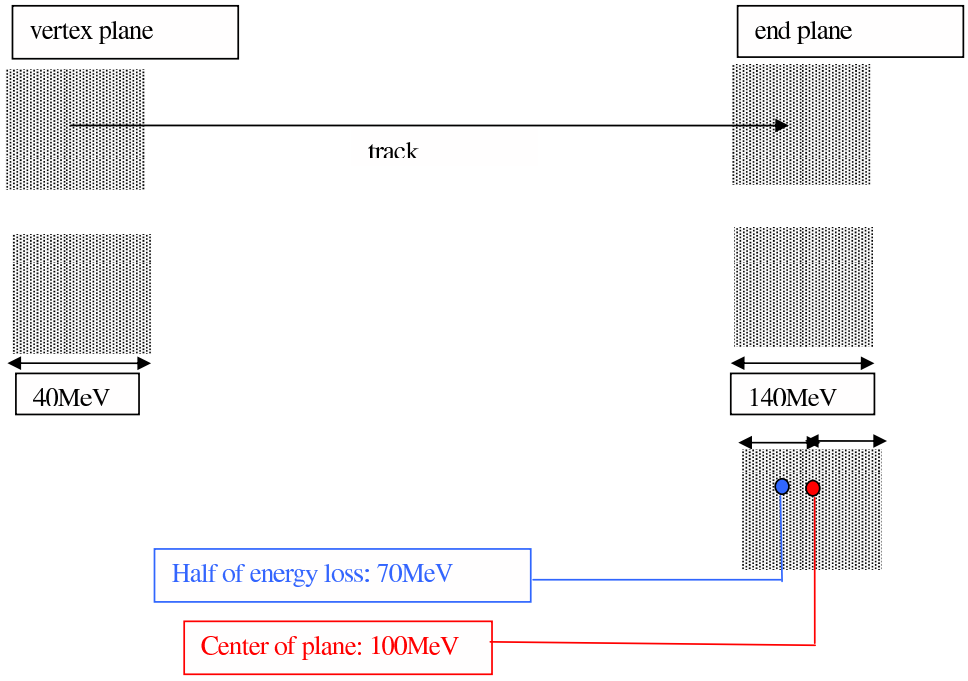

Figure 4.22: Momentum loss of muon in the vertex plane and the end plane. The muon loses a maximum 29.0 MeV (Equation 4.10) in the vertex steel plane and 140.0 MeV (Equation 4.12) in the track end plane.

$$\sigma_{vtx} = \frac{29.0\ MeV}{\sqrt{12}} \tag{4.10}$$

4.5.1.1.2 Momentum Uncertainty from Track End For the track end the muon's $\frac{dE}{dx}$ increases rapidly, so for the last plane,

$$\begin{aligned} Range &= R = 2.54cm \times 7.85\ gcm^{-3} = 20.0\ gcm^{-2} \\ \tfrac{R}{M} &= 189.0\ gcm^{-2}\ GeV^{-1} \end{aligned} \quad \text{where M is the mass of the muon} \tag{4.11}$$

A range of 189.0 gcm^{-2} corresponds to 140.0 MeV muon momentum [28]. That is a muon with less than 140 MeV will stop within a plane.

This gives uncertainty in momentum from the track end, σ_{end}

$$\sigma_{end} = \frac{140.0\ MeV}{\sqrt{12}} \tag{4.12}$$

4.5.1.1.3 Momentum Uncertainty from "straggling" For a muon of energy $0-5\ GeV$ in iron, $\frac{\sigma_s}{p_\mu(range)} \sim 3.5\%$[33] this value is fairly constant to within 1%,

4.5.1.1.4 Total Momentum Uncertainty Then from Equations 4.10 and 4.12 and Section 4.5.1.1.3, the total error for range calculations due to vertex and end offsets and straggling effect, σp;

$$\sigma^2 p = \sigma^2_{vtx} + \sigma^2_{end} + \sigma^2_s \tag{4.13}$$

The total $\frac{\sigma p}{p}$ predicted in this way, along with the individual contributions is shown in Figure 4.23. Also shown in that figure is the actually observed $\frac{\sigma p}{p}$ vs $p_\mu(reco)$ for the Far and the Near Detectors.

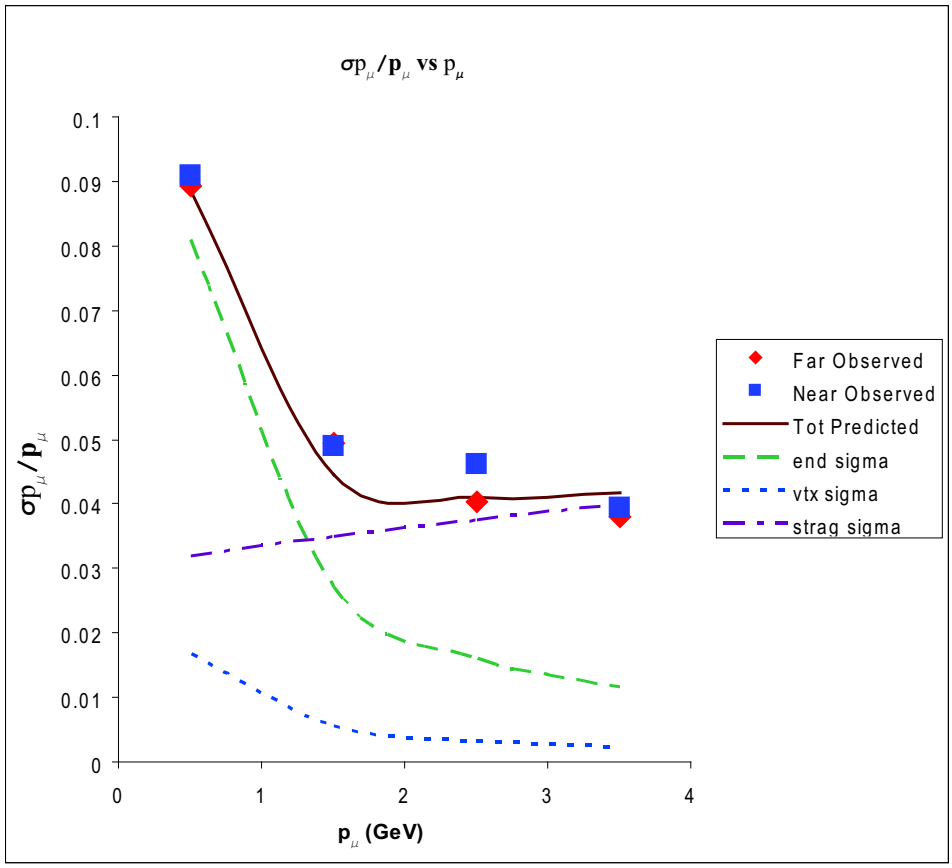

Figure 4.23: $\frac{\sigma p}{p}$ vs *Reconstructed* p_μ, predicted and observed.

4.5.2 p_ν Reconstruction for QEL-like-selected events

All Monte Carlo events that satisfy the fiducial criteria described in Section 4.3 and pass the PID cuts determined in Sections 4.4.2 and 4.4.2.1, were used in this study. The quantity $\Delta p_\nu = p_\nu(true) - p_\nu(reco)$ was plotted for all these QEL-like-selected events and this is shown in Figure 4.21. These are the same events for which p_μ was studied in Section 4.5.1.

4.5.2.1 Using QEL Kinematics

The quantity $\Delta p_\nu = p_\nu(true) - p_\nu(QELreco)$ is also plotted for all QEL-like-selected events, i.e., events selected by the PID as QEL-like, but not necessarily true QEL events. This is shown in Figure 4.24 and it shows an excessive bias in events with $p_\nu(true) > p_\nu(QELreco)$. This is due to RES events in which a low energy Δ particle is produced without a visible signature in our detector. The low energy Δ particle quickly decays into a neutron or a proton and pions. But the pions are of low energy so they do not produce tracks; the protons do not go more than two planes, as discussed before.

4.5.2.2 Using QEL Kinematics with the Δ Resonance

The RES events that produce low energy Δ's and give no hadronic shower, behave just like the QEL events that give a proton. So we should be able to treat such events similarly to the QEL scattering events and derive their parent neutrino energy from Equation 4.2, $E_\nu = \frac{2m_N E_\mu - m_\mu^2 - m_N^2 + m_X^2}{2(m_N - E_\mu + |\vec{p_\mu}| cos\theta)}$. This is essentially the QEL Equation 4.3, before the proton mass and the neutron mass cancel each other off. In RES scattering $m_N = 0.939\ GeV$ and $m_X = m_\Delta = 1.232\ GeV$.

The signatures these QEL-like-true-RES events leave in the detector are identical to the true QEL events, and thus identifying them separately is impossible. Finding

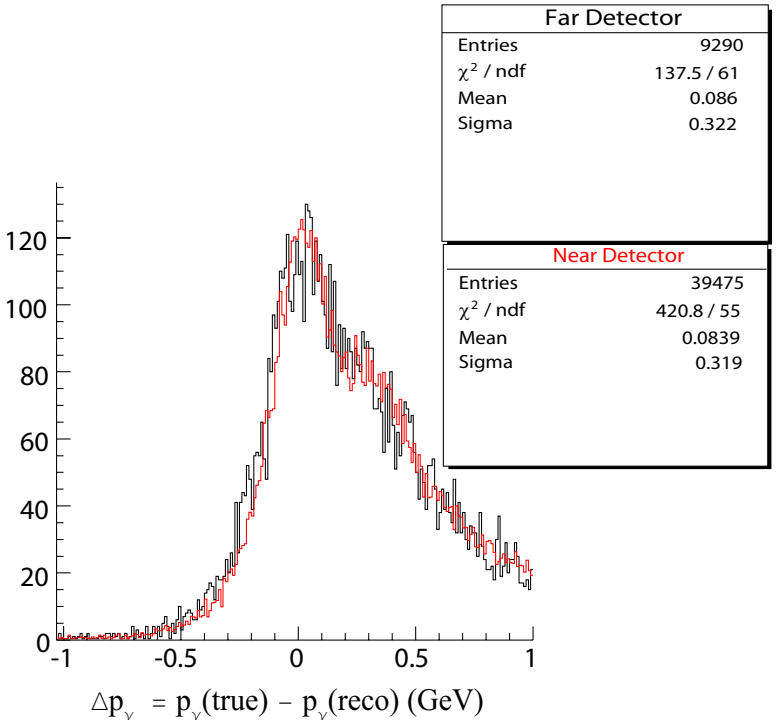

Figure 4.24: $\Delta p_\nu = p_\nu(true) - p_\nu(QELreco)$ for all QEL events filtered through the fiducial volume and the PID's discussed in Sections 4.4.2 and 4.4.2.1. Monte Carlo for the Near and Far Detectors are in red and black respectively. The Near Detector is normalized to the total number of events filtered in the Far Detector.

a PID range to apply the QEL kinematics and RES kinematics was a more practical approach. I applied a sliding PID cut to the already filtered QEL-like events to find the best PID ranges that these separate equations can be applied to. These PID ranges are shown in Table 4.1. The neutrino energy reconstructed this way is shown in Figure 4.25.

	Near Detector	Far Detector
PID range for QEL-like event selection	$PID < -6.0$	$PID < 0.0$
PID range for QEL equation 4.3	$PID < -12.0$	$PID < -10.0$
PID range for RES equation 4.2	$-12.0 \leq PID \leq -6.0$	$-10.0 \leq PID \leq 0.0$

Table 4.1: PID ranges used in selecting QEL-like events and reconstructing the parent neutrino energy either by using QEL equation (Equation 4.3) or the RES equation (Equation 4.2). So for example in the Near Detector, all events with $PID < -6.0$ will be selected as QEL-like events. Out of these events, those that have $PID < -12.0$ will be treated with the QEL equation with the proton (Equation 4.3) and the rest with $-12.0 \leq PID \leq -6.0$ will be treated with the RES equation with the Δ (Equation 4.2)

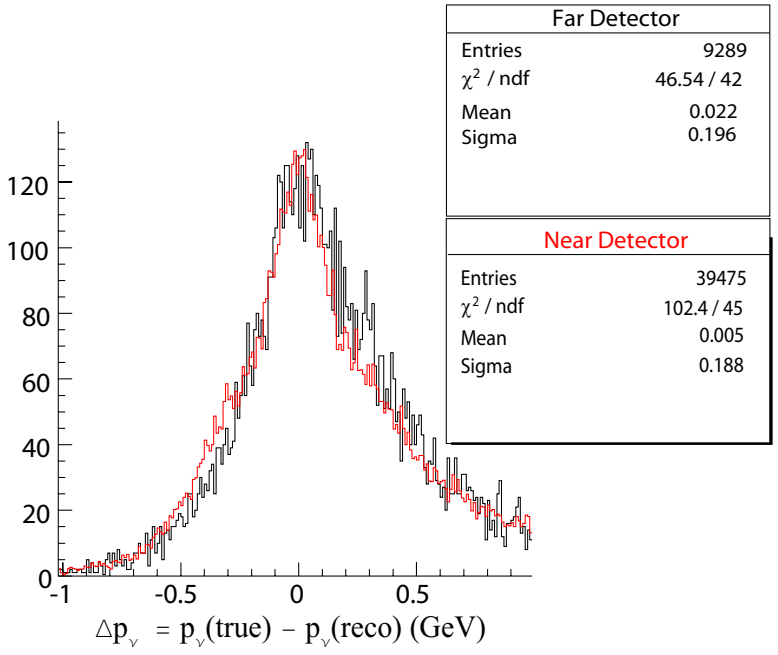

Figure 4.25: $\Delta p_\nu = p_\nu(true) - p_\nu(QELreco)$ for all QEL events filtered through the fiducial volume and the PID's discussed in Sections 4.4.2 and 4.4.2.1. $p_\nu(QELreco)$ is calculated from either Equation 4.3 or Equation 4.2, depending on the event's PID, as shown in Table 4.1. Near Detector is in red, Far Detector is in black and the Near Detector is normalized down to the total number of events filtered in the Far Detector.

4.6 Summary of Selection Cuts

1. **Basic Cuts:** Require at least one track in the event

2. **Fiducial Cuts:** Far Detector : 0.5 $m \leq$ track vertex z $\leq$ 14.5 m, 16.5 $m \leq$ track vertex z $\leq$ 29.4 m and 0.4 $m \leq$ track vertex r $\leq$ 3.5 m Near Detector : 1.0 $m \leq$ track vertex along Z $\leq$ 5.0 m track vertex along radial $\leq$ 1 m

3. **Reconstructed Muon Angle Cut:**

   For both detectors, it was required that $cos\theta > 0.7$, where θ is the angle of the muon with respect to the neutrino.

4. **Reconstructed p_μ Cuts:**

   Far Detector : if track end $<$ 481 *planes* the range was used, else if $curve \neq 0$ and $\frac{\sigma_{curve}}{curve} < 0.1$ the curvature measurement was used. Near Detector : if track end $<$ 275 *planes* the range was used, else if $curve \neq 0$ and $\frac{\sigma_{curvature}}{curvature} <$ 0.1 the curvature measurement was used.

5. **Selecting QEL-like Events:**

   All events with no showers were taken to be QEL-like-selected events. For events with one shower, the particle identification parameter (PID) described in Sections 4.4.2, 4.4.2 and 4.4.2.1 was used. The criterion for filtering in as a QEL-like-selected event is : Far Detector : $PID < 0.0$ selected as QEL-like. Near Detector : $PID < -6.0$ selected as QEL-like.

6. **p_ν Reconstruction: with Proton Mass or Resonance Mass:**

   The QEL scattering equation with the proton mass, $E_\nu = \frac{2m_N E_\mu - m_\mu^2}{2(m_p - E_\mu + |\vec{p_\mu}|cos\theta)}$, was used if the following PID criteria were satisfied. Far Detector : $PID < -10.0$ Near Detector : $PID < -12.0$

The QEL scattering equation with the Δ^{++} mass, $E_\nu = \frac{2m_N E_\mu - m_\mu^2 - m_N^2 + m_{\Delta^{++}}^2}{2(m_N - E_\mu + |\vec{p_\mu}| cos\theta)}$, was used if the following PID criteria were satisfied. Far Detector : $-10.0 \leq PID < 0.0$ Near Detector : $-12.0 \leq PID < -6.0$

7. **Reconstructed p_ν Cuts:**

   For both detectors, it was required that $0.0\ GeV \leq p_\nu(Reco) < 10.0\ GeV$.

Chapter 5

Oscillation Analysis Procedure and Mock Data Challenge

If we can predict the unoscillated neutrino flux at the Far Detector then we can compare it to the actually observed flux. If a deficit is observed in the observed spectrum, then that would be an indication of neutrino oscillations. We can in theory predict this unoscillated Far neutrino spectrum by using our knowledge of the initial neutrino beam and the neutrino-nucleon scattering cross-sections. However as previously seen in Figure 1.2, uncertainties in neutrino-nucleon scattering cross sections are high and the prediction will thus be affected by it.

As mentioned before, a good way to overcome that problem is to place two detectors in the same neutrino beam line, one detector near the neutrino source measuring the unoscillated spectrum and the other far away from the source measuring the oscillated spectrum. Then the ratio between these two spectra will show a deficit in the oscillated Far spectrum. Even then, the effects of neutrino-nucleon scattering cross section do not completely cancel, because with oscillations, the ratio between neutrino interactions and background in the Near Detector is different from that ratio in the Far Detector.

5.1 Neutrino Fluxes in the Near and Far Detectors

As discussed in Section 3.2, the neutrino beam results from the decays of pions and kaons. So the neutrino beam observed in the Near and Far Detectors are highly correlated, but not identical. The differences between the detectors arise from several effects, namely beam divergence and the decay position of the parent hadrons.

5.1.1 Beam Divergence

The neutrino beam diverges as it travels from the meson decay point to the detectors, which results in the Far Detector not intercepting the total area of the diverged beam. This is shown in Figure 5.1.

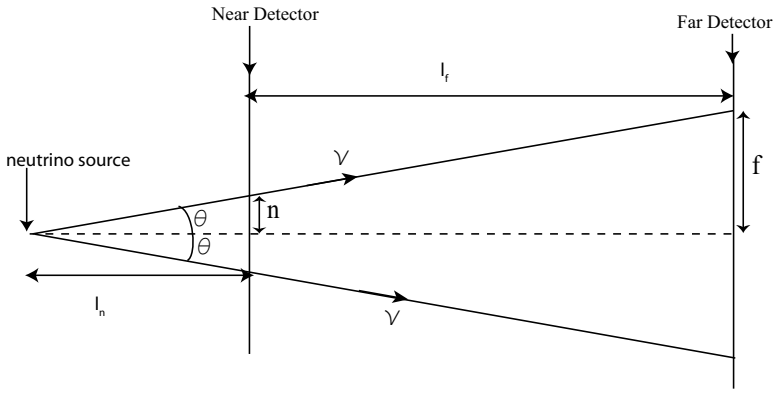

Figure 5.1: Diverging neutrino beam.

Then, for a unit area of acceptance at the center of the detectors, the flux intercepted by the Far Detector ϕ_f is given by,

$$\phi_f = \frac{l_n^2}{l_f^2}\phi_n \tag{5.1}$$

where l_n is the distance from source to Near Detector, l_f is the distance from source to Far Detector, and ϕ_n is the flux intercepted by a unit area at the center of the Near Detector.

With $l_n(mean) = 700m$ and $l_f(mean) = 734km$ the mean value of ϕ_f is $1.0 \times 10^{-6} \times \phi_n$. But the ratio of $\frac{l_n^2}{l_f^2}$ is not a constant since it depends on the decay point of the parent pion or kaon. While the Far Detector sees the neutrino source as a point source, the Near Detector sees it as a finite source due to the finite length of the decay volume where the parent hadrons decay.

5.1.2 Radial and Z Position of the Meson Decay

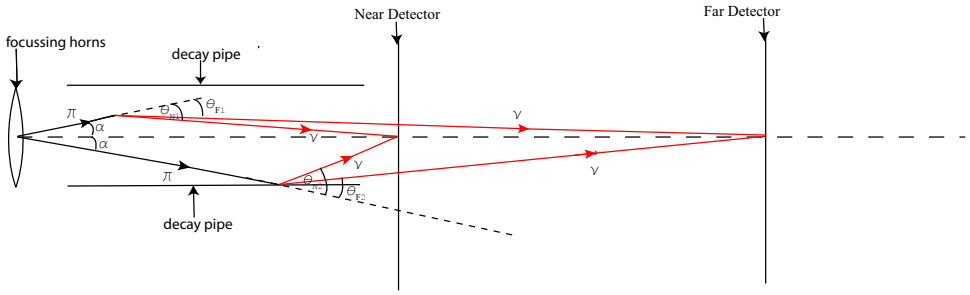

Figure 5.2: Decay angle differences that vary with the parent mesons decay point along the Z axis and the radial direction inside the decay pipe.

Because of the finite size of the decay volume, neutrinos from different ranges of decay angles hit the Near and Far Detectors. As shown in Figure 5.2, the decay angle required by a neutrino reaching the center of the Near Detector, θ_N, is different from that needed by a neutrino reaching the center of the Far Detector, θ_F. And the difference between these decay angles, $\Delta\theta = \theta_N - \theta_F$ varies depending on the decay point along the axis of the decay volume. For example $\Delta\theta_1$ from a decay upstream in the decay volume is smaller than $\Delta\theta_2$ from a decay downstream.

The difference in the angles subtended by a unit area in the center of each of

the detectors varies also with the radial decay point of the parent meson as shown in Figure 5.2.

Since the neutrino momentum itself depends on this decay angle, the neutrino momentum spectra in the Near Detector and Far Detector are affected in different ways.

Figures 5.3 and 5.4 show how the neutrino energy in the Near and Far Detectors vary with the decay point of the parent meson/muon. They also show that the difference between the detectors is not a constant in neutrino energy, so a simple energy correction is not sufficient.

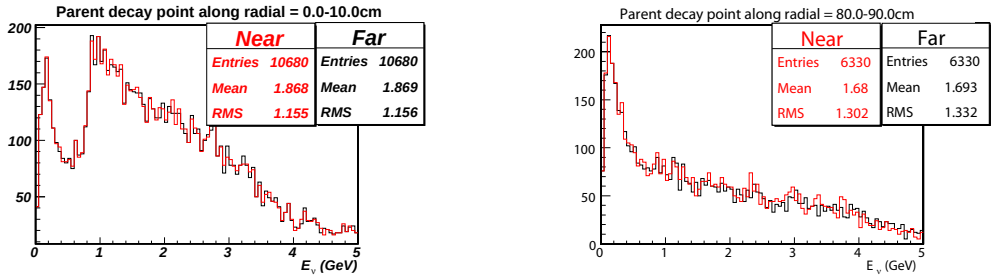

Figure 5.3: Neutrino energy in the Near (red) and Far (black) detectors for different meson/muon decay points along the radial direction of the decay pipe

5.2 Predicting the Far Detector Unoscillated Spectrum

A good way to get around the discrepancies between the Near and Far Detector neutrino energy spectra, is to use a Far/Near ratio to go from the Near Detector observed to the Far Detector predicted, as shown in Equation 5.2.

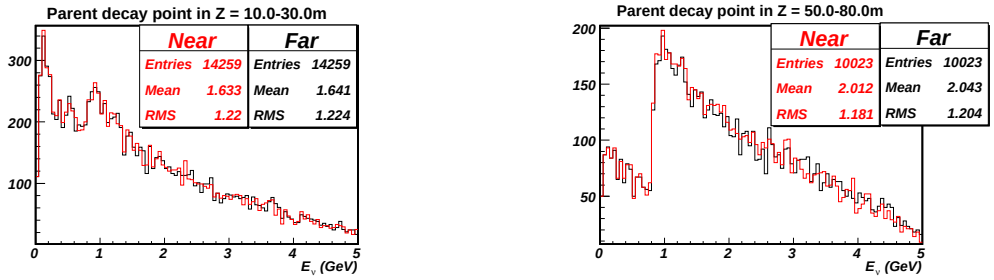

Figure 5.4: Neutrino energy in the Near (red) and Far (black) detectors for different meson/muon decay points along the Z axis of the decay pipe

$$\frac{dN_{farpred}}{dE} = \left(\frac{\frac{dN_{far}}{dE}}{\frac{dN_{near}}{dE}} \right)_{MC} * \frac{dN_{nearobs}}{dE} \tag{5.2}$$

where $\left(\frac{\frac{dN_{far}}{dE}}{\frac{dN_{near}}{dE}} \right)_{MC}$ will incorporate weights corresponding to discrepancies introduced by beam divergence, decay angle and radial position.

To get the values of $\left(\frac{\frac{dN_{far}}{dE}}{\frac{dN_{near}}{dE}} \right)_{MC}$, a Monte Carlo simulation of the beam was used. In this Monte Carlo sample the parent meson beam is modeled. The probability of the meson decaying, *hadprob*, is calculated using its energy and the mesonic life time. This gives the meson decay point in space. Kinematics is used to obtain the neutrino momentum and direction. In the simulation, these neutrinos travel downstream where they are forced to interact at the center of the Near Detector and then at the Far Detector, after being weighted for decay angles. The energies of the neutrino spectra obtained as such in the Near and Far Detectors are denoted by E_{Near} and E_{Far}. The probabilities that a neutrino interact in the Near Detector and the Far Detector after accounting for beam divergence is denoted by $Nearwt$ and $Farwt$ respectively[34].

First, a two dimensional histogram of E_{Far} vs E_{Near} was made by weighting the

bin contents by $hadprob$ and $Farwt$ and $Nearwt$. This is shown in Figure 5.5. Then for the ni^{th} and fi^{th} energy bin in the Near Detector and the Far Detector, the ratio of $\left(\frac{\frac{dN_{far}}{dE}}{\frac{dN_{near}}{dE}}\right)_{MC}$, $FNRatio_{ni,fi}$, is the corresponding cell content.

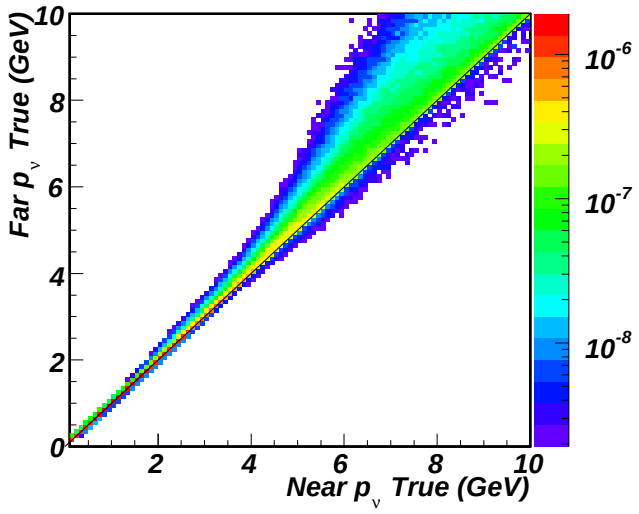

Figure 5.5: $p_\nu Far$ vs $p_\nu Near$ showing the smearing of the neutrino energy when going from the Near Detector to the Far Detector. The (ni, fi) cell content shows the probability of observing a neutrino of energy fi in the Far Detector having observed a neutrino of energy ni in the Near Detector.

Then, in theory if we have an observed spectrum of the Near Detector , we can make a bin by bin Far Detector unoscillated spectrum prediction by Equation 5.4.

$$\begin{pmatrix} \frac{dN_{farpred}}{dE_{f1}} \\ . \\ . \\ \frac{dN_{farpred}}{dE_{fb}} \end{pmatrix} = \begin{pmatrix} FNRatio_{n1,f1} & . & . & FNRatio_{nb,f1} \\ . & & & \\ . & & & \\ FNRatio_{n1,fb} & . & . & FNRatio_{nb,fb} \end{pmatrix} \begin{pmatrix} \frac{dN_{nearobs}}{dE_{n1}} \\ . \\ . \\ \frac{dN_{nearobs}}{dE_{nb}} \end{pmatrix} \tag{5.3}$$

$$\frac{dN_{farpred}}{dE_{fi}} = FNRatio_{ni,fi} \times \left(\frac{dN_{nearobs}}{dE_{ni}} \right) \tag{5.4}$$

where $\frac{dN_{nearobs}}{dE_{ni}}$ is the observed differential neutrino energy spectrum in the Near Detector.

But it is not accurate to use Equation 5.4, because $FNRatio_{ni,fi}$ is made of true neutrino energies, while $\frac{dN_{nearobs}}{dE_{ni}}$ is made of reconstructed neutrino energies. For this reason we need to introduce a second pair of matrices that relate the true neutrino energy to the reconstructed neutrino energy, in the Far and the Near Detectors. These two matrices are shown as two dimensional histograms in Figure 5.6. These $recoE \rightarrow trueE$ matrices will be denoted by $RecoTrue_{ni,ti}$, where ni and ti will be the reconstructed and true energy bins. The two dimensional matrices obtained from these two histograms would be almost diagonal, if all the true QEL events are selected. The true QEL events in the detector are selected via one dimensional purity and efficiency matrices, p_n, e_n and p_f, e_f for the Near Detector and Far Detector respectively. By correcting for the efficiency the effects due to different selection efficiencies in the Near Detector and the Far Detector will be minimized. Here the purity and efficiency matrices are defined as follows -

$$p_{ni} = \frac{(\text{\# selected true QEL events})_{ni}}{(\text{\# all QEL-like-selected events})_{ni}}$$

$$e_{ni} = \frac{(\#\text{ selected true QEL events})_{ni}}{(\#\text{ all QEL events})_{ni}}$$

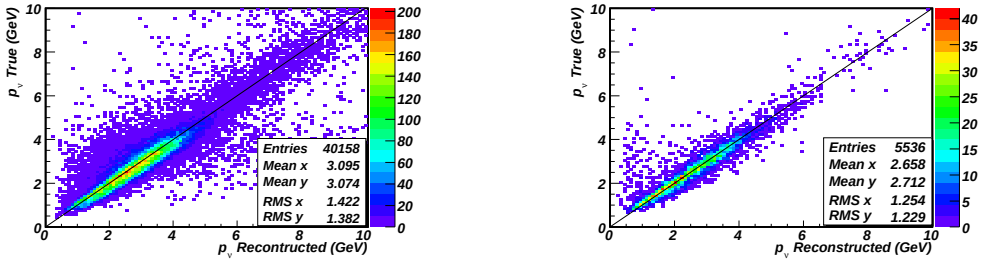

Near Detector Far Detector

Figure 5.6: $p_\nu(True)$ vs $p_\nu(Reco)$ for the Near Detector and the Far Detector showing the smearing of the neutrino energy due to reconstruction.

5.2.1 Matrix Method to Predict Unoscillated Far Spectrum

When this method of matrices is utilized, the prediction of the unoscillated Far Detector spectrum, starting from the observed Near Detector spectrum, $\frac{dN_{nearobs}}{dE_{ni}}$ can be broken into several steps as follows.

1. Obtain the reconstructed neutrino energy spectrum for QEL-like-selected events in the Near Detector , $\frac{dN_{nearobs}}{dE_{ni}}$, from the selection cuts mentioned in Section 4.6.

2. Predict the selected true QEL spectrum, $\frac{dN_{sQnear}}{dE_{ni}}$ using the purity matrix:

$$\frac{dN_{sQnear}}{dE_{ni}} = p_{ni} \times \left(\frac{dN_{nearobs}}{dE_{ni}}\right) \tag{5.5}$$

   The purity matrix, p_{ni} and the observed neutrino spectrum, $\frac{dN_{nearobs}}{dE_{ni}}$ are binned in reconstructed energy.

3. Get the corresponding true energy spectrum, $\frac{dN_{sQTnear}}{dE_{ti}}$, for the selected true QEL events:

$$\frac{dN_{sQTnear}}{dE_{ti}} = NearRecoTrue_{ni,ti} \times \left(\frac{dN_{sQ}}{dE_{ni}}\right) \tag{5.6}$$

4. Predict the total true QEL spectrum in the Near Detector , $\frac{dN_{AllQnear}}{dE_{ti}}$:

$$\frac{dN_{AllQnear}}{dE_{ti}} = \frac{1}{e_{ti}} \times \left(\frac{dN_{sQTnear}}{dE_{ti}}\right) \tag{5.7}$$

   The efficiency matrix, e_{ni} is binned in true neutrino energy. So the resulting spectrum is the true neutrino energy spectrum of all true QEL events in the Near Detector.

5. Use the $Near \rightarrow Far$ matrix, $FNRatio_{ni,fi}$, obtained from the beam Monte Carlo, to predict the true neutrino energy spectrum for all true QEL events in the Far Detector.

$$\frac{dN_{farpred}}{dE_{ti}} = FNRatio_{tni,tfi} \times \left(\frac{dN_{AllQnear}}{dE_{ti}}\right) \tag{5.8}$$

6. From here do the inverse matrix multiplication of steps 1-4 to obtain the reconstructed energy spectrum of the QEL-like-selected events in the Far Detector. So first get the true energy spectrum of the selected true QEL events in for the Far Detector, $\frac{dN_{sQTfar}}{dE_{ti}}$.

$$\frac{dN_{sQTfar}}{dE_{ti}} = e_{ti} \times \left(\frac{dN_{farpred}}{dE_{ti}}\right) \tag{5.9}$$

7. Then convert this true energy spectrum to the reconstructed energy spectrum for selected true QEL events in the Far Detector, $\frac{dN_{sQfar}}{dE_{ni}}$:

$$\frac{dN_{sQfar}}{dE_{fi}} = FarRecoTrue_{ti,ni} \times \left(\frac{dN_{sQTfar}}{dE_{ti}}\right) \tag{5.10}$$

8. Predict the unoscillated reconstructed neutrino energy spectrum of QEL-like-selected events in the Far Detector, $\frac{dN_{farpred}}{dE_{fi}}$:

$$\frac{dN_{farpred}}{dE_{fi}} = \frac{1}{p_{fi}} \times \left(\frac{dN_{sQfar}}{dE_{fi}}\right) \tag{5.11}$$

5.3 Mock Data Challenge

A mock data sample, in which the nominal unoscillated Monte Carlo sample for the Far Detector was oscillated with a specific Δm^2_{23}, $\sin^2 2\theta_{23}$ value, was used for this study. The oscillation parameters were unknown at the beginning, thereby making it a real-data-like analysis. The Δm^2_{23}, $\sin^2 2\theta_{23}$ values obtained by performing the analysis could then be compared to the actual values to give a measure of the rigorousness of the analysis method. The Near Detector Monte Carlo sample (Figure 5.7) was treated as the Near Detector mock data and the unoscillated Far Detector spectrum was predicted using the matrix method outlined in Section 5.2.1.

The Method of Maximum Likelihood [28] was used to find the best fit values of Δm^2_{23}, $\sin^2 2\theta_{23}$. For the i^{th} energy bin, if $\nu_i(j)$ is the expected number of events for oscillations at the j^{th} given (Δm^2_{23}, $\sin^2 2\theta_{23}$) value and n_i is the observed number of events, the the likelihood function is defined as shown in Equation 5.12.

$$-2ln\lambda(j) = 2\sum_{i=1}^{N}\left[\nu_i(j) - n_i + n)iln\frac{n_i}{\nu_i(j)}\right] \tag{5.12}$$

The minimum of $-2ln\lambda(j)$ follows the χ^2 distribution in the large sample limit [28]. The quantity given by Equation 5.12 was calculated for the two dimensional parameter space of Δm^2_{23}, $\sin^2 2\theta_{23}$ and a grid search was then done to find the

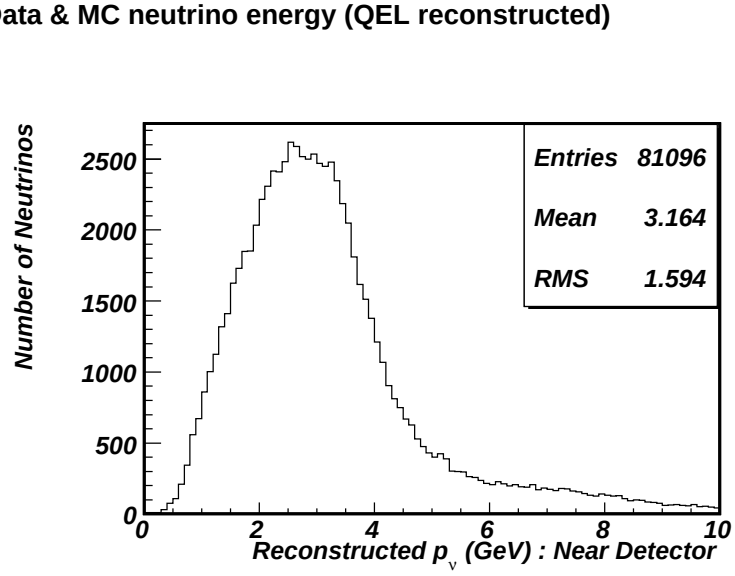

Figure 5.7: The Near Detector mock data spectrum

minimum $-2ln\lambda(j)$ value and the best fit was obtained by using the Δm^2_{23}, $\sin^2 2\theta_{23}$ values pertaining to this minimum $-2ln\lambda(j)$. The predicted Far Detector unoscillated spectrum, together with the Far Detector mock data and the best fit line is shown in Figure 5.8. Due to uncertainties in measuring the short muon resulting from a neutrino with $p_\nu < 0.5\,GeV$ and due to the low number of QEL events observed with $p_\nu > 5\,GeV$, $-2ln\lambda(j)$ was calculated using neutrinos in the energy range $0.5 - 5.0\,GeV$ only. This gave a $\frac{\chi^2_{min}}{ndof} = \frac{59}{(45-2)}$ for 45 bins of $0.1\,GeV$ energy in the two dimensional parameter space. The χ^2 contours for the 68.27% (1σ), 95.45%(2σ) and 99.73%(3σ) confidence levels, together with the actual Δm^2_{23}, $\sin^2 2\theta_{23}$ value with which the Far Detector mock data was created is shown in Figure 5.10. The minimum χ^2 is obtained for (Δm^2_{23}, $\sin^2 2\theta_{23}$) = $(0.0025\ eV^2, 0.89)$. The actual values of (Δm^2_{23}, $\sin^2 2\theta_{23}$) were $(0.0024\ eV^2, 0.93)$. As can be seen from Figure 5.10, the results lie within 2σ (i.e., 95.45% confidence level) from the actual.

Appendix C.1 shows the same mock data sample analyzed for neutrino energies of 0.5 GeV - 10.0 GeV, and the contour sizes remain comparable to that shown in Figure 5.10.

A different representation of Figure 5.8 is shown in Figure 5.9. This shows the ratio of the predicted unoscillated spectrum to the observed spectrum in the Far Detector.

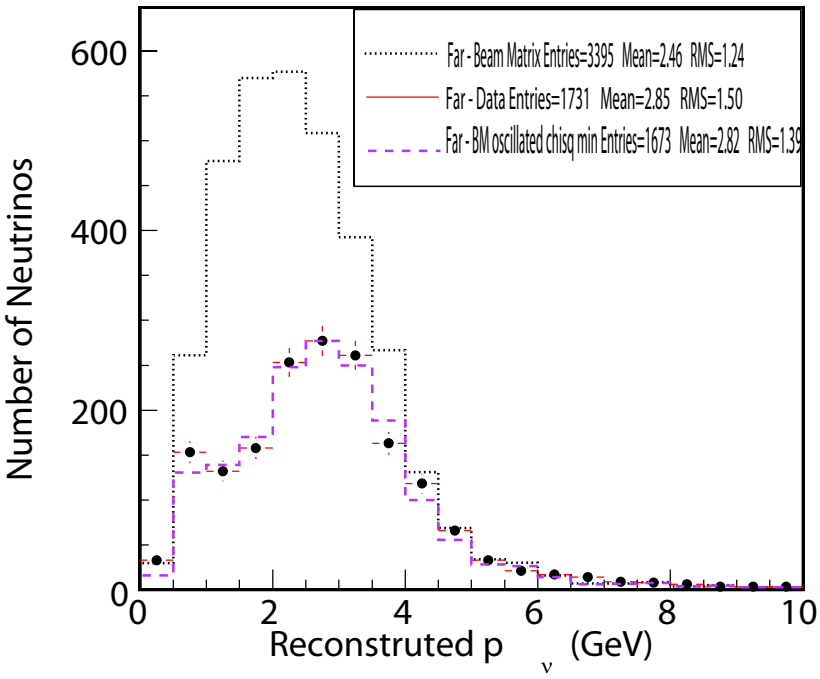

Figure 5.8: The Far Detector mock data spectrum (black data points), the Far Detector predicted unoscillated spectrum (black dotted line) and the best fit for the data(pink dashed line).

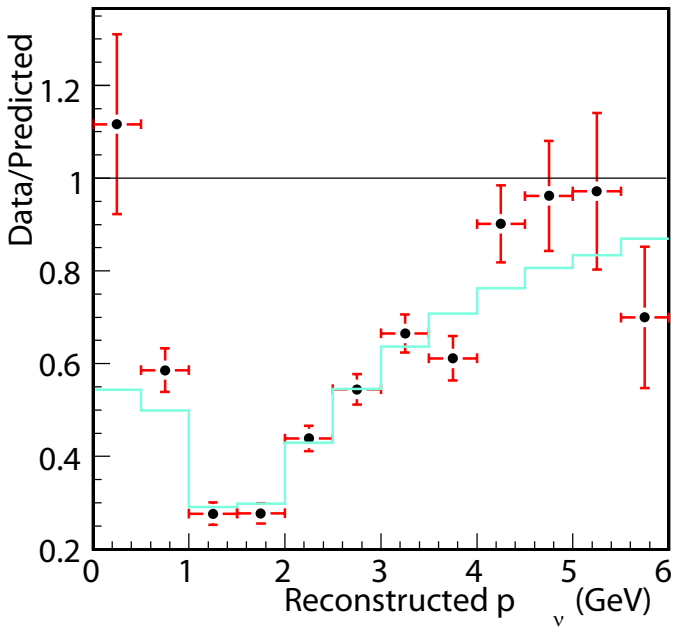

Figure 5.9: The ratio of $\frac{\text{predicted unoscillated Far Detector spectrum}}{\text{observed Far Detector spectrum}}$ for the mock data. The best fit line for the data for oscillation parameters $(\Delta m^2_{23}, \sin^2 2\theta_{23}) = (0.0025\ eV^2, 0.89)$is the blue solid line.

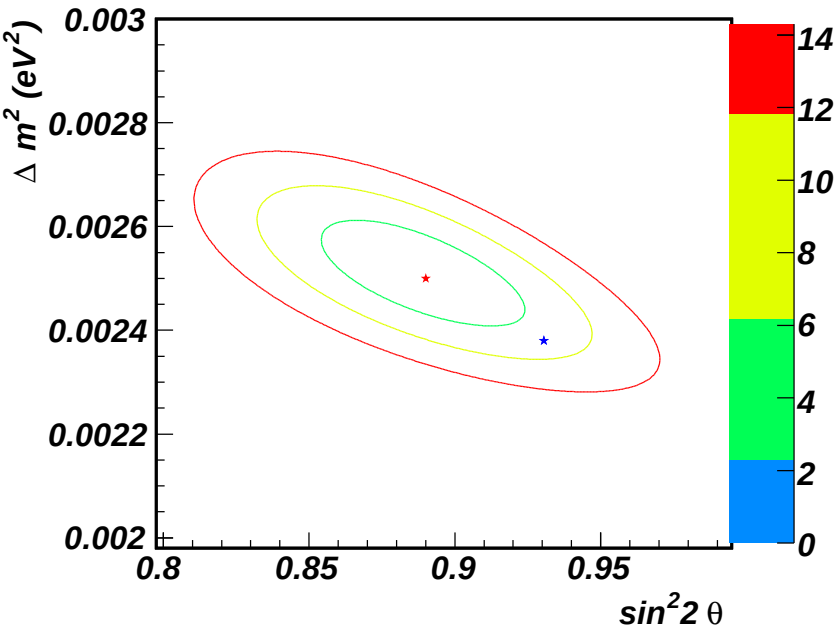

Figure 5.10: The minimum χ^2 point of $(\Delta m^2_{23}, \sin^2 2\theta_{23}) = (0.0025\ eV^2, 0.89)$ shown as the red star.The three contours correspond to the 68.27% (green), 95.45% (yellow) and 99.73% (red) confidence levels for two degrees of freedom. [28]. The actual point with which the Far Detector mock data was generated is the blue star.

Chapter 6

Data Analysis

Since satisfactory results were obtained for the mock data it was determined that the techniques used for QEL separation (Chapter 4) and oscillation analysis (Chapter 5) could now be applied to real data.

The Monte Carlo samples analyzed were for the neutrino beam only. But in reality, both Near and Far Detectors take cosmic ray data continuously, regardless of whether there was a neutrino beam or not. So it is important to separate the periods in which the neutrino beam was operational and analyze only that data. This task can be accomplished by looking at the proton beam itself and placing several cuts with respect to the beam position on target, focusing horn current, etc.

6.1 Beam Quality Cuts

The following standard beam quality cuts were applied in order to ensure that the neutrino beam was on and the the conditions of the neutrino beam were the same as those modeled in the Monte Carlo study.

- Protons on target in each spill should be at least 0.5×10^{12}. This ensures

that the proton beam was on and producing pions and kaons that in turn will decay into neutrinos.

- Having the proton beam on itself will not ensure a neutrino beam. We also have to make sure the proton beam hits the target.For this we require the horizontal, bx, and vertical, by, positions of the beam on the target be such that; $-2.00\ mm \leq bx \leq -0.01\ mm$ and $2.00mm \geq by \geq 0.01\ mm$

- As mentioned before the target can be moved to obtain different energy configurations of the neutrino beam. The Monte Carlo studied in this thesis was generated for the low energy neutrino beam. So we need to ensure that the target is in the low energy position.

- The focusing horns and their focusing power will dictate the neutrino energy spectrum, as discussed before. So the horn current Ih, is required to be such that; Ih; $-200\ kA \leq Ih \leq -155\ kA$.

- Width of proton beam be less than $2.9\ mm$. This ensures that the pions and kaons of the correct energy will reach the focusing horns and the desired neutrino energy spectrum is obtained.

- Check the time difference between neutrino beam spill and time of Far Detector snarl to make sure the selected events are actually from the beam. The Far Detector is notified via Global Positioning System (GPS) when a beam spill occurs. It then predicts the time the beam will reach the Far Detector and opens a time window roughly 40 μs before this time and writes out the detector readings until about 60 μs after this time. We pick beam induced events in the Far Detector by requiring that the time of the earliest hit in an event be between $-20\ \mu s$ and $30\ \mu s$ of the beam spill time predicted at the Far Detector. Figure 6.1 shows the time between the actual beam spill and the

time snarls occur in th Far Detector. This is the time it takes for a neutrino traveling at the speed of light to reach the Far Detector. Figure 6.2 shows the time between the Far Detector predicted beam spill time and the time of the snarl for the data events that pass all selection cuts.

- Require that the detector magnets are on to ensure momentum by curvature measurements are valid.

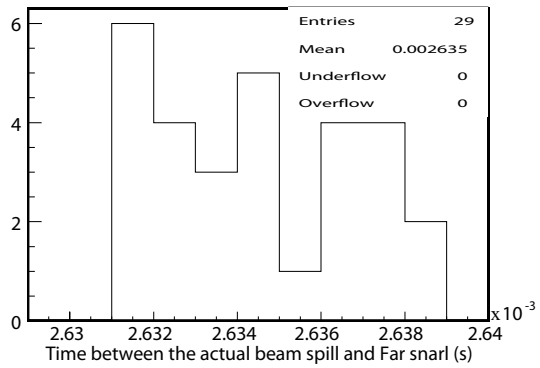

Figure 6.1: Time between the actual beam spill and the Far Detector snarls for the data that filter through all selection cuts in the Far Detector. This is the time it takes for neutrinos traveling nearly at the speed of light to go 734 km from Fermilab to Soudan.

6.2 Data and Monte Carlo Comparison

Having ensured that I was indeed looking at neutrino beam induced events, I could now compare the data and the Monte Carlo samples. Since my technique of separating QEL events and performing an oscillation analysis was based on Monte

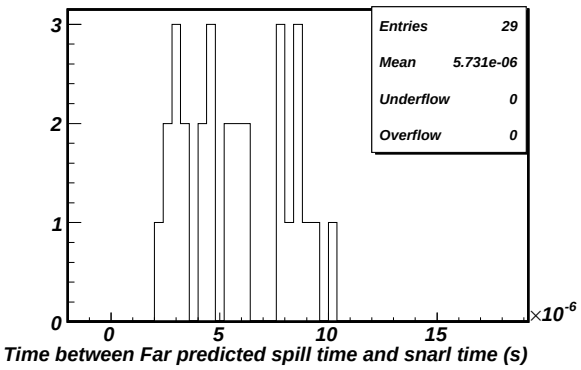

Figure 6.2: Time between the Far predicted beam spill and the Far Detector snarls for the data that filter through all selection cuts in the Far Detector. All events are well within the -20 μs and 30 μs cut. All 29 events are also clustered within a 8.5 μs window corresponding to the spill duration of 8.6 μs.

Carlo samples, it was important to see if the data behave the same way as the Monte Carlo, before I employed those methods for data analysis.

6.2.1 Near Detector

Since the Near Detector gives a measure of the unoscillated neutrinos, the data and Monte Carlo agreement should be good. This agreement is important for the PID variables I use for QEL separation, in order to justify the usage of those variables on the data. Also important is the agreement between data and Monte Carlo for the muon momentum, the angle of the muon and finally the neutrino energy spectrum.

6.2.1.1 PID Variables - Near Detector

Figure 6.3 shows the comparison between Data and Monte Carlo in the Near Detector for the variables that were used for the PID calculation as described in

Section 4.4.1. Figure 6.4, shows the comparison for the PID parameter itself in the Near Detector. Even though the data and Monte Carlo agreement is not perfect for the individual variables, the differences cancel off between them to give excellent agreement for the PID parameter itself. This agreement justifies the use of the Monte Carlo separation techniques for the data as well.

6.2.1.2 p_μ, $cos\theta_\mu$ Spectra - Near Detector

Since the neutrino momentum reconstructed from the QEL equation depends on the muon momentum and the angle of the muon with respect to the neutrino, I have studied the data and Monte Carlo agreement for those two primary reconstruction quantities in Figure 6.5. While the angle measurement shows good agreement, it can be seen that the Monte Carlo is shifted to higher energies than the data for p_μ. The exact cause for this is unknown; it is speculated that it might be that the neutrino beam is not properly modeled in the Monte Carlo and this effect is incorporated as a systematic error. The effect cannot be due to reconstruction errors, since it was shown in Figure 4.21 that the true and reconstructed muon momenta agree quite well.

6.2.1.3 p_ν Spectra - Near Detector

Figure 6.6 shows the comparison between data and Monte Carlo for the reconstructed p_ν spectra. Here, all the events are the QEL-like-selected events, selected according to the selection cuts described in Section 4.6. Additional cuts described in Section 6.1 have been imposed to ensure that the data were taken when the beam was on and the magnet was running. As can be seen the Monte Carlo is shifted to higher neutrino energies. The cause for this stems from the disagreement between data and Monte Carlo for p_μ that was seen in Figure 6.5.

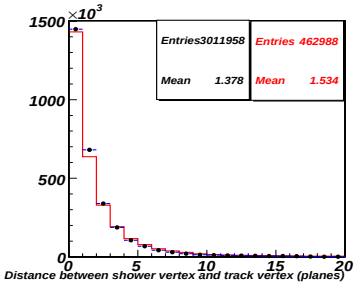

(1)

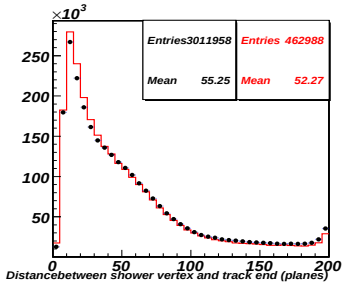

(2)

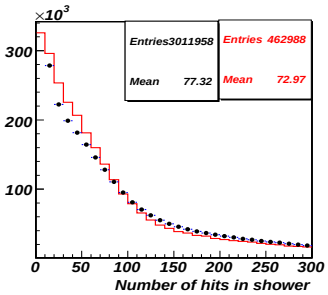

(3)

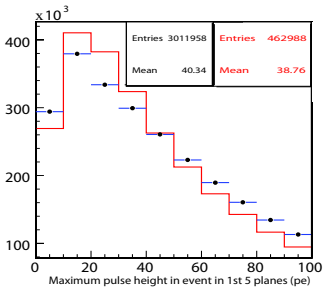

(4)

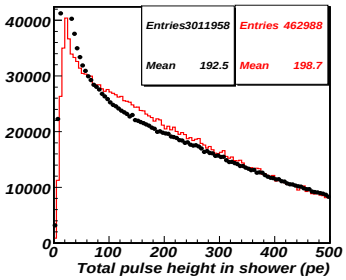

(5)

Figure 6.3: Data Monte Carlo comparison in the Near Detector for variables listed in List 4.4.1 used for Probability distribution functions. The Data is in red and the MC is in black. Also the MC has been normalized to Data (by using the integral of each histogram).

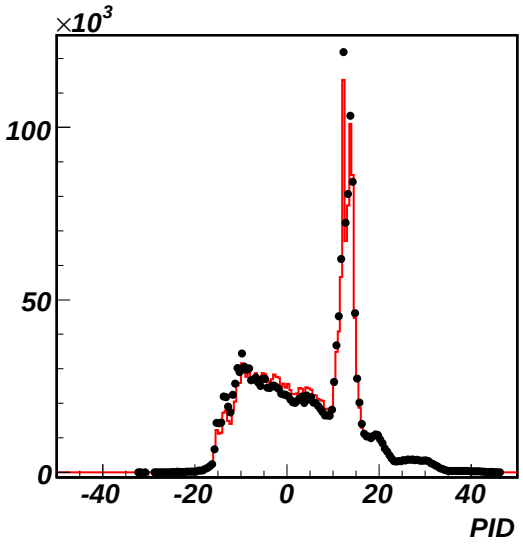

Figure 6.4: Data (black dots) and Monte Carlo (red solid line) comparison for the PID parameter (Equation 4.8 in the Near Detector.

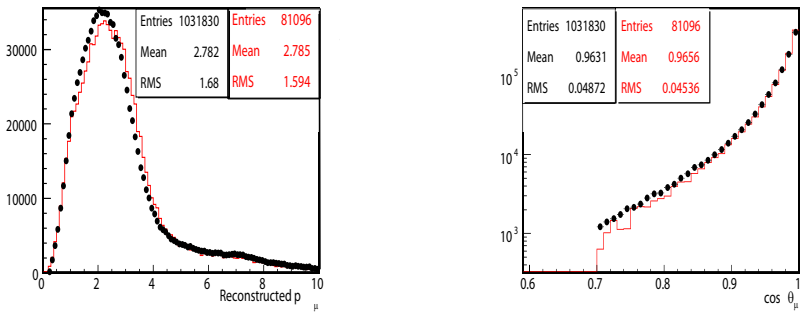

Reconstructed p_μ Reconstructed $cos\theta_\mu$

Figure 6.5: Data (black dots) and Monte Carlo (red line) comparison in the Near Detector for p_μ and $cos\theta_\mu$. Also the Monte Carlo has been normalized to Data (by using the integral of each histogram).

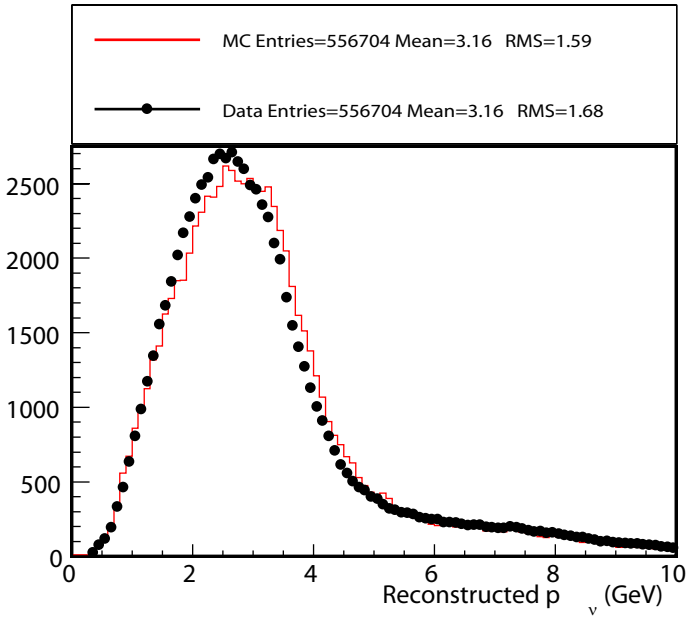

Figure 6.6: Data and Monte Carlo comparison for Reconstructed p_ν (Equation 4.8) in the Near Detector. Histograms have been normalized to areas.

6.2.2 Far Detector

Direct comparison between data and Monte Carlo in the Far Detector will not yield such good agreement as in the Near Detector. This is because the Monte Carlo is for the unoscillated neutrino energy spectrum, whereas the data will be of the oscillated one.

6.2.2.1 Reconstructed Variables -Far Detector

As discussed in Chapter 4.1 the quasi-elastically reconstructed neutrino momentum is dependent only on two variables: the reconstructed muon momentum, and the reconstructed muon angle with respect to the neutrino direction. These two quantities for QEL-like-selected events for the Far Detector are shown in Figure 6.7. Oscillations are clearly evident in the comparison of reconstructed muon momentum with that predicted.

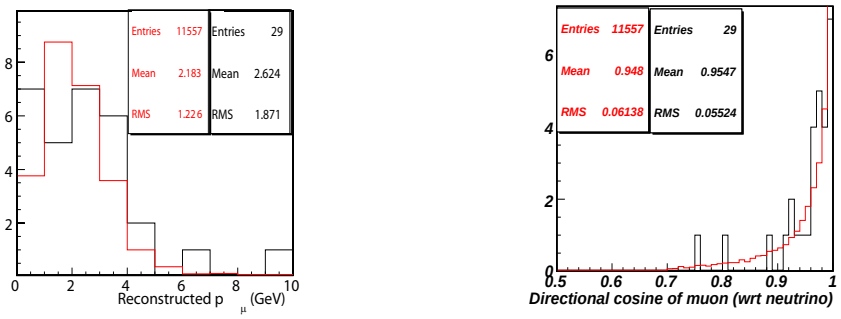

Reconstructed p_μ (GeV) Directional Cosine of Muon (wrt neutrino)

Figure 6.7: The reconstructed muon momentum spectra and the reconstructed muon angle with respect to the neutrino direction for data (black) and Monte Carlo (red) for QEL-like-selected events in the Far Detector.

The distributions of track vertices in the Far Detector are shown in Figure 6.8. When events occur close to the end, they escape the detector and the range measurement becomes invalid. The curvature measurement is used for these events. But as discussed before, because of the uncertainties in the magnetic field, very stringent cuts are placed on the curvature measurement. This means very few events that occur towards the end and escape the detector are used in the analysis. For this reason there is some non-uniformity observed in the Z distribution of the track vertices, as seen in Figure 6.8.

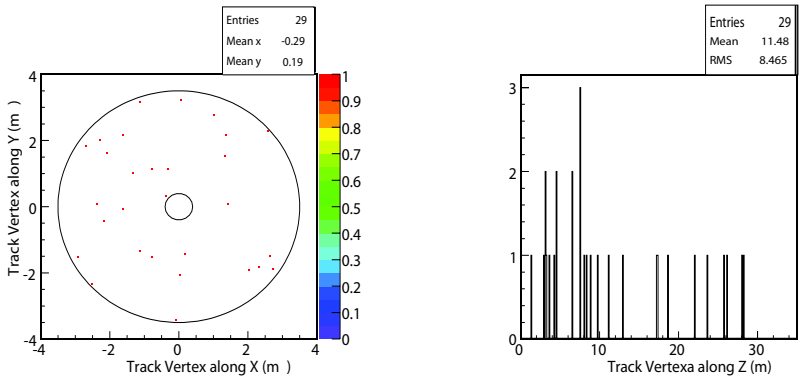

Track Vertex along X and Y axes Track Vertex along Z axis

Figure 6.8: Track Vertex (along X, Y and Z axes) distributions for QEL-like-selected events in the Far Detector.

6.3 Oscillation Analysis

Having selected QEL-like data and Monte Carlo samples in the Near and the Far Detectors, the oscillation analysis technique described in Chapter 5 was performed.

The p_ν spectrum for the QEL-like-selected Near Detector data was shown previously in Figure 6.6. The Far Detector p_ν spectrum predicted from this Near spectrum, together with the observed Far Detector p_ν spectrum, is shown in Figure 6.9. Also shown in Figure 6.9 is the best fit corresponding to the minimum χ^2, where the χ^2 equivalent of Maximum Likelihood was calculated as in Equation 5.12. The ratio between data and predicted Far p_ν spectra and the best fit line are shown in Figure 6.10.

Since the number of events in the Far Detector is very low, a bin width of 0.5 GeV was used for the p_ν spectra and the fit was done for 1.0 $GeV \leq p_\nu < 4.5$ GeV in the two dimensional parameter space of Δm^2_{23}, $\sin^2 2\theta_{23}$. The minimum χ^2 per degrees of freedom was $\frac{\chi^2_{min}}{ndof} = \frac{3.2}{7-2}$. The best fit value of Δm^2_{23}, $\sin^2 2\theta_{23}$ was 2.91×10^{-3} eV^2 and 0.990 respectively. The χ^2 contours for the 68.27% (1σ), 95.45%(2σ) and 99.73%(3σ) confidence levels, together with the best fit point are shown in Figure 6.11.

Appendix C.2 shows the same data sample analyzed for neutrino energies of 0.5 GeV - 10.0 GeV, and the 68.27% (1σ) statistical uncertainties remain comparable to that obtained here.

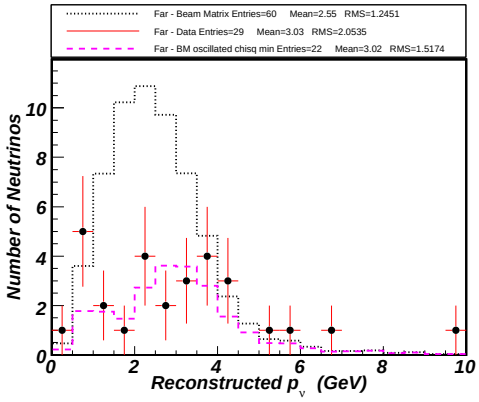

Figure 6.9: The reconstructed p_ν spectra. The Far Detector data are the black data points, the Far Detector predicted unoscillated spectrum is the black dotted line and the best fit for the data for oscillation parameters that give the minimum χ^2 is the pink dashed line.

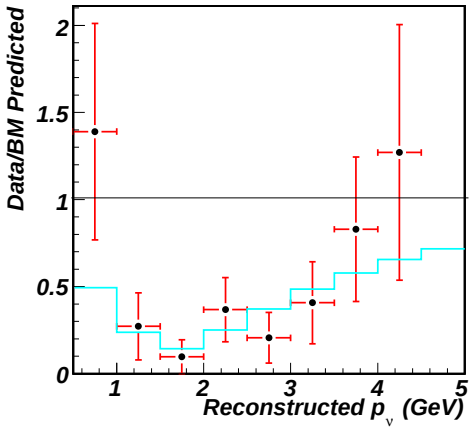

Figure 6.10: The ratio of $\frac{\text{observed Far Detector spectrum}}{\text{predicted unoscillated Far Detector spectrum}}$ for the data. The best fit for oscillation parameters $(\Delta m^2_{23}, \sin^2 2\theta_{23}) = (2.91 \times 10^{-3}\ eV^2, 0.990)$ is the blue solid line.

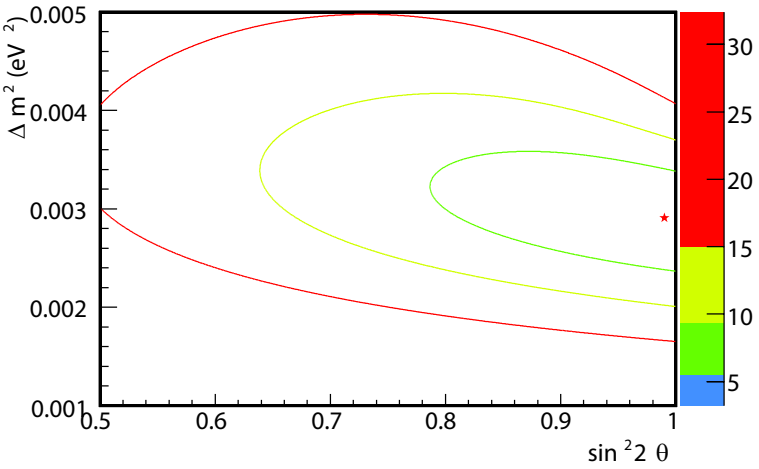

Figure 6.11: The minimum χ^2 point of $(\Delta m^2_{23}, \sin^2 2\theta_{23}) = (2.91 \times 10^{-3}\ eV^2, 0.990)$ shown as the red star, together with the reduced χ^2 contours for the data. The three contours correspond to the 68.27% (green), 95.45% (yellow) and 99.73% (red) confidence levels for two degrees of freedom. [28].

6.4 Data Check in Far Detector

In Section 6.2.2, I said that direct comparison between data and Monte Carlo will not yield as good results as in the Near Detector, because the Far Detector data is oscillated but the Far Detector Monte Carlo is unoscillated.After obtaining the oscillation parameters however, we should be able to weight the unoscillated Monte Carlo sample with the corresponding oscillation probability and compare that to the data.

Figure 6.12 shows the data and Monte Carlo comparison for the PID parameter. It should be recalled that the PID cut for the Far Detector was $PID < 0.0$. The agreement is within 2σ. Data events were hand scanned and they appeared to be equally divided between clear QEL events with the proton signature (as a high pulse height at the track vertex) and RES events with pion signatures (on average five planes of high pulse height hits that resemble tracks). These pion tracks however were not reconstructed as tracks, which is attributed to the fact that MINOS's main analysis, the charged current analysis, relies on the identification of muon tracks and thus tends to reconstruct other hits, including short tracks (as these pion tracks) as showers.

Figures 6.13 show the data and Monte Carlo comparison between the reconstructed muon momentum and the angle of the muon with respect to the neutrino. These comparisons agree to within 1σ of errors.

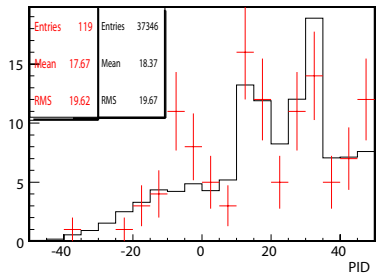

Figure 6.12: Data (red with error bars) and Monte Carlo (black) comparison for the PID parameter in the Far Detector. Here the Monte Carlo has been oscillated with $(\Delta m^2_{23}, \sin^2 2\theta_{23}) = (2.91 \times 10^{-3}\ eV^2, 0.990)$.

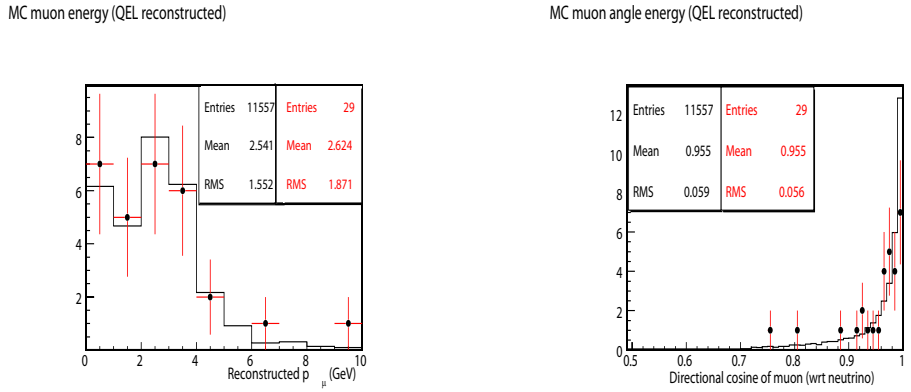

Reconstructed p_μ (GeV) Directional Cosine of Muon (wrt neutrino)

Figure 6.13: The reconstructed muon momentum spectra and the reconstructed muon angle with respect to the neutrino direction for data (red with error bars) and Monte Carlo (black) for QEL-like-selected events in the Far Detector. Here the Monte Carlo has been oscillated with $(\Delta m^2_{23}, \sin^2 2\theta_{23}) = (2.91 \times 10^{-3}\ eV^2, 0.990)$.

Chapter 7

Conclusions

7.1 Oscillation Parameters with Statistical Uncertainties

As shown in the last chapter, the QEL-like data from MINOS's first run was fit to obtain oscillation parameters of $(\Delta m^2_{23}, \sin^2 2\theta_{23}) = (2.91 \times 10^{-3}\ eV^2, 0.990)$. The low number of 29 data events obviously introduces a large statistical error to the result. Since $\sin^2 2\theta_{23}$ is close to the physical boundary of one, the errors are asymmetrical, with larger negative errors. So, for the final result I only quote this negative error on $\sin^2 2\theta_{23}$. The result with the statistical error at $\pm 1\sigma$ is $\Delta m^2_{23} = 2.91^{+0.49}_{-0.53} \times 10^{-3}\ eV^2$ and $\sin^2 2\theta_{23} = 0.990_{-0.180}$. The χ^2 projections of Δm^2_{23} and $\sin^2 2\theta_{23}$ are shown in Figure 7.1.

7.2 Systematic Uncertainties

For the systematic error study, first a mock Far Detector data sample was generated by oscillating the nominal Far Detector spectrum with (Δm^2_{23}, $\sin^2 2\theta_{23}$) =

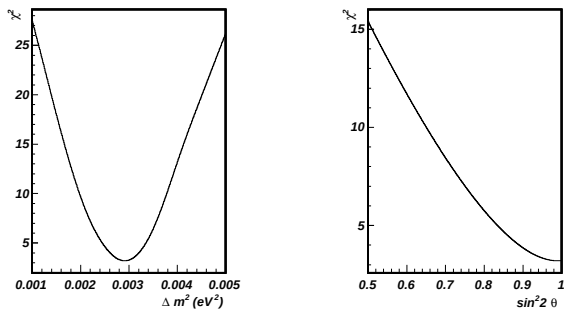

Figure 7.1: The χ^2 is plotted for the two oscillation parameters separately. The left plot is for the Δm^2_{23} projection and the right plot is for the $\sin^2 2\theta_{23}$ projection.

$(2.91 \times 10^{-3}\ eV^2, 0.990)$, the oscillation parameters obtained in the actual data fitting. Then the Near and Far spectra were weighted bin by bin according to each systematic uncertainty and the same analysis techniques were employed to estimate the shifts in Δm^2_{23} and $\sin^2 2\theta_{23}$. The different uncertainties are assumed to be uncorrelated, so they have been treated independently. This also allows to add the errors in quadrature, to get the net effect of all the sources.

The systematic uncertainties in this analysis are of several types:

1. QEL cross sectional uncertainties: $\pm 10\%$ from world data.[28, 36]

2. RES cross sectional uncertainties: $\pm 10\%$ from world data.[28, 36]

3. Neutral Current (NC) contamination: Since the NC scattering processes have low visible energy they tend to contaminate the CC sample in the crucial low energy bins. For this reason, MINOS conservatively estimates the uncertainty form the NC contamination to be 50%.[37]

4. Fermi Momentum Uncertainties: The histograms shown in Figure 4.2 were

used to generate smearing due to Fermi momentum for a given neutrino energy.

5. Muon momentum uncertainties: ±2% due to density uncertainties that affect the muon momentum by range measurement and magnetic field uncertaintes that affect the muon momentum by curvature measurement. [37]

6. Neutrino beam uncertainties: Beam tuning histograms that tune the beam in such a way that the Monte Carlo matches the data better have been produced [37]. This is an attempt to address the discrepancy seen in Figure 6.5, between data and simulated. These histograms were used to obtain shifts that were then applied to the Monte Carlo.

7. Normalization uncertainty: An overall normalization uncertainty of ±4% was applied. This results from a 2% uncertainty in the fiducial mass in both detectors, a 3% uncertainty in the relative Near Far reconstruction efficiencies and a 1% uncertainty in the detector live time.[37]

Table 7.1 shows the effects of the systematic uncertainties listed above. The net systematic uncertainty is small compared to the statistical uncertainty.

It can be seen that the cross-section uncertainties have the least impact on both Δm^2_{23} and $\sin^2 2\theta_{23}$ as is expected with the matrix method. This can be mathematically explained as follows : if E_N and E_F are the Near observed and Far predicted neutrino energy matrices, σ_{CC} is the cross-section uncertainty matrix and B is the beam matrix that relates the Near spectrum to the Far spectrum, then;

$$E_F = \sigma_{CC}^{-1} \times B \times \sigma_{CC} \times E_N \tag{7.1}$$

Here $\sigma_C C$ is a diagonal matrix. If the beam matrix was perfectly diagonal too, the B and σ_{CC} commute to give :

$$E_F = \sigma_{CC}^{-1} \times \sigma_{CC} \times B \times E_N$$
$$E_F = B \times E_N \text{ regardless of the values of } \sigma_{CC}$$

The beam matrix shown in Figure 5.5 is almost diagonal, which makes the effects due to the cross-section very small as is seen in Table 7.1. This is the main attraction of using the Matrix Method.

The position of the oscillation minimum dictates Δm^2_{23} and the depth of it dictates $\sin^2 2\theta_{23}$. So uncertainties in Fermi momentum, muon momentum, neutral current contamination and beam tuning affect both Δm^2_{23} and $\sin^2 2\theta_{23}$, because it not only shifts the oscillation minimum, but also fills it, thereby affecting the amplitude of the oscillation. Normalization uncertainties affect the depth of the oscillation minimum, thus $\sin^2 2\theta_{23}$is affected mostly.

7.3 Conclusion

This thesis presents an oscillation analysis based on the muon neutrino charged current quasi-elastic events in the MINOS experiment's initial run. The period under consideration had 1.27×10^{20} protons of 120 GeV energy incident on the NuMI target. The number of observed quasi-elastic events with energies below 10 GeV was 29, where the expected number was 60 ± 3. This observation implies that $\Delta m^2_{23} = 2.91^{+0.49}_{-0.53}(stat)^{+0.08}_{-0.09}(sys) \times 10^{-3}\ eV^2$ and $\sin^2 2\theta_{23} = 0.990_{-0.180}(stat)_{-0.030}(sys)$.

The oscillation parameters obtained by using all the charged current interactions from this same run are $\Delta m^2_{23} = 2.74^{+0.44}_{-0.26} \times 10^{-3}\ eV^2$ and $\sin^2 2\theta_{23} > 0.87$ at 68% confidence level (where statistical and systematic uncertainties are combined).[32] This full analysis had 215 observed events with 336 ± 14 predicted.[32]

Uncertainty	Shift in $\lvert\Delta m^2_{23}\rvert$ ($10^{-3}\ eV^2$)	Shift in $\sin^2 2\theta_{23}$
QEL Cross section ($\pm 10\%$)	$^{+0.00}_{-0.00}$	$^{+0.0045}_{-0.0055}$
RES Cross section ($\pm 10\%$)	$^{+0.01}_{-0.01}$	$^{+0.0015}_{-0.0015}$
Neutral Current ($\pm 50\%$)	$^{+0.06}_{-0.07}$	$^{+0.0205}_{-0.0175}$
Fermi Momentum	-0.02	-0.0170
Muon Momentum ($\pm 2\%$)	$^{+0.05}_{-0.05}$	$^{+0.0050}_{-0.0055}$
Beam Uncertainty	-0.02	-0.0195
Normalization ($\pm 4\%$)	$^{+0.01}_{-0.01}$	$^{+0.0135}_{-0.0150}$
Total	$^{+0.08}_{-0.09}$	$^{+0.0255}_{-0.0355}$

Table 7.1: Systematic Uncertainties and their sources.

The results obtained from the QEL events presented in this thesis, together with the results obtained for past experiments is shown in Figure 7.2.

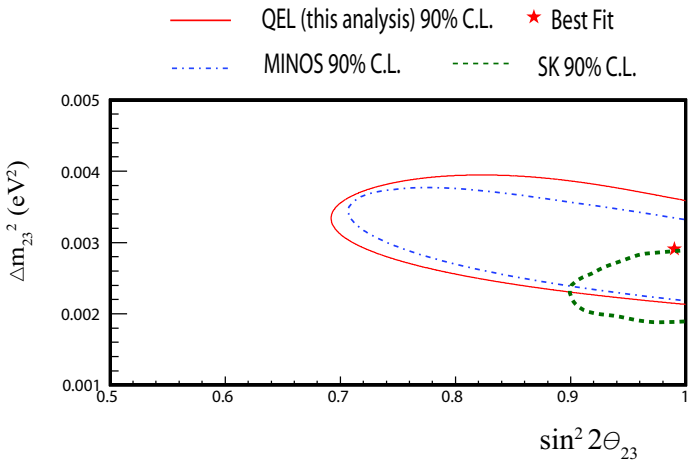

Figure 7.2: The 90% confidence level contour for the MINOS QEL events is shown in red. Also shown are the 90% contours for the MINOS[37] full data set and Super-Kamiokande[35].

MINOS has already collected more than twice the amount of data analyzed in this thesis. With MINOS's extended running, the event separation and analysis techniques employed in this thesis show promise of a higher precision on the oscillation parameters of $\nu_\mu \rightarrow \nu_\tau$.

Appendix A

Derivation of Formulae

A.1 Threshold energy for $\nu_X N$ CC scattering

For a charged current neutrino interaction given by

$$\nu_X(p_\nu) + N(p_N) \rightarrow X(p_X) + N^{'}(p_N^{'}) \tag{A.1}$$

where $X = e, \mu$ or τ and $N = p$ or n and the 4-momenta of each particle is given within parentheses).

Then if the total energy in the lab frame is $\sqrt{s}$, we can write s_{before} and s_{after}, for the before and after scattering situations,

$$\begin{aligned} s_{before} &= (p_\nu + p_N)^2 \\ &= p_\nu^2 + p_N^2 + 2p_\nu p_N \text{ where } p_\nu^2 = m_\nu^2 = 0,\ p_\nu = E_\nu \text{ and } \vec{p_N} = 0 \\ &= m_N^2 + 2E_\nu m_N \end{aligned}$$

$$\begin{aligned} s_{after} &= (p_X + p_N^{'})^2 \\ &> (m_X + m_N^{'})^2 \text{ if X and } N^{'} \text{ are made at rest} \end{aligned}$$

Then,

$$\begin{aligned} s_{before} &= s_{after} \\ E_{\nu_X}(thresh) &= \frac{m_X(m_X + 2m_N)}{2m_N} \end{aligned}$$

where m_X is the mass of the relevant charged lepton and m_N is the mass of the neutron or proton involved in the interaction.

A.2 E_ν dependence on E_π and θ

$$\begin{aligned} \pi^- &\rightarrow \nu_\mu + \mu^- \\ p_\pi &= p_\nu + p_\mu \text{ in 4-momentum} \end{aligned}$$

$$\begin{aligned} (p_\pi - p_\nu)^2 &= p_\mu^2 \\ m_\pi^2 + m_\nu^2 - 2p_\pi p_\nu &= m_\mu^2 \\ m_\pi^2 - 2(E_\pi E_\nu - \vec{p_\pi}.\vec{p_\nu}) &= m_\mu^2 \text{ (where in CM } \vec{p_\pi} = 0 \text{ and } E_\pi = m_\pi) \\ m_\pi^2 - 2m_\pi E_\nu &= m_\mu^2 \\ E_\nu &= \frac{m_\pi^2 - m_\mu^2}{2m_\pi} \\ E_\nu^{CM} = p_\nu^{CM} &= \frac{m_\pi^2 - m_\mu^2}{2m_\pi} \end{aligned}$$

Boost center of mass energy/momentum to lab energy/momentum:

$$\begin{aligned} E^l_\nu &= \gamma(E^{CM}_\nu + \beta p^{CM}_{\nu_x}) \\ p^{CM}_{\nu_x} &= E^{CM}_\nu cos\theta \\ E^l_\nu &= \gamma E^{CM}_\nu (1 + \beta cos\theta) \end{aligned}$$

Here,

$$\begin{aligned} tan\theta &= \frac{p^{CM}_{\nu_y}}{p^{CM}_{\nu_x}} \text{ for the CM frame} \\ tan\alpha &= \frac{p^l_{\nu_y}}{p^l_{\nu_x}} \text{ for the lab frame} \end{aligned}$$

and θ and α are related by,

$$\begin{aligned} p^l_{\nu_y} &= p^{CM}_{\nu_y} \\ p^l_{\nu_x} &= \gamma p^{CM}_\nu (cos\theta + \beta) \end{aligned}$$

which gives,

$$E_\nu = \frac{0.43 E_\pi}{1 + \gamma^2 \theta^2} \tag{A.2}$$

A.3 Energy Loss by Charged Particles

The rate of energy loss by ionization of charged particles is given by the Bethe-Bloch formula[28]:-

$$-\frac{dE}{dx}_{ion} = nZz^2 \frac{4\pi\alpha^2\hbar^2}{m_e\beta^2} \left[ln\frac{2m_e c^2\beta^2}{I(1-\beta^2)} - \beta^2 \right] \tag{A.3}$$

where, m_e is the electron mass, z and v are the charge (in units of e) and velocity of the particle, β=v/c, n is the atoms per unit volume of the medium, Z and A are the atomic and mass numbers of the medium, $\alpha = \frac{1}{137}$ and x is the path length in the medium measured in gcm^{-2} and I is the effective ionization potential of the atom.

Another way charged particles lose energy is through bremsstrahlung (radiation):-

$$-\frac{dE}{dx}_{rad} = \frac{4nZ^2\alpha^3\hbar^2c^2}{{m_e}^2c^4}Eln\frac{183}{Z^{1/3}} = \frac{E}{X_0} \tag{A.4}$$

$$X_0 = \left(\frac{4nZ^2\alpha^3\hbar^2c^2}{{m_e}^2c^4}ln\frac{183}{Z^{1/3}}\right)^{-1} \tag{A.5}$$

where X_0 is the radiation length. $X_0 = 13.84gcm^{-2}$ for iron.

With some approximations, $I = 16Z^{0.9}eV$ and $\beta = 0.96$ (at which minimum ionization occurs),

$$\frac{\frac{dE}{dx}_{rad}}{\frac{dE}{dx}_{ion}} \simeq \frac{ZE(MeV)}{560} \tag{A.6}$$

This ratio is 1 for electrons at what is called the critical energy of the electrons. The exact equation for this critical energy E_{crit} then is,

$$E_{crit_e} = \frac{800MeV}{Z + 1.2}[28] \tag{A.7}$$

$$E_{crit_e} = 29.4MeV \quad \text{for electrons in iron} \tag{A.8}$$

When the kinetic energy of the moving particle is below E_{crit}, energy loss by ionization dominates and when the particle's kinetic energy is above E_{crit}, energy loss by radiation dominates and grows rapidly with E.

Since the electrons that we consider with energies about $1GeV$ are well above their critical energy of $E_{crit_e} = 29.4MeV$ they lose energy by radiation mostly. The

photons radiated by the electrons create e^+e^- pairs, producing an electromagnetic shower.

The electromagnetic shower depth is given by,

$$X_{emrange} = (n+1)L_{PP} \quad \text{with } L_{PP} \simeq \tfrac{9}{7}X_0 \tag{A.9}$$

where L_{PP} is the mean free path for pair production.

On the other hand, since $(dE/dx)_{rad}$ is inversely proportional to ${m_e}^2$ as shown in equation A.4, for muons with mass m_μ,

$$E_{crit\mu} = E_{crite} \times \left(\frac{m_\mu}{m_e}\right)^2 = 1314GeV \tag{A.10}$$

Appendix B

Additional Information

B.1 Muon Momentum Reconstruction: Range or Curvature

Figures B.1 and B.2 show the agreement between the reconstructed muon momentum and the true muon momentum, for the range measurement and the curvature measurement respectively. When these are compared to Figure 4.6, it is seen that the muon momentum reconstructed with the selection cuts in Section 4.3.1.1 are in better agreement with the true value, than either the range or curvature measurements separately. Plotted are all events that are true ν_μ events that interact via the CC interaction in the Far Detector.

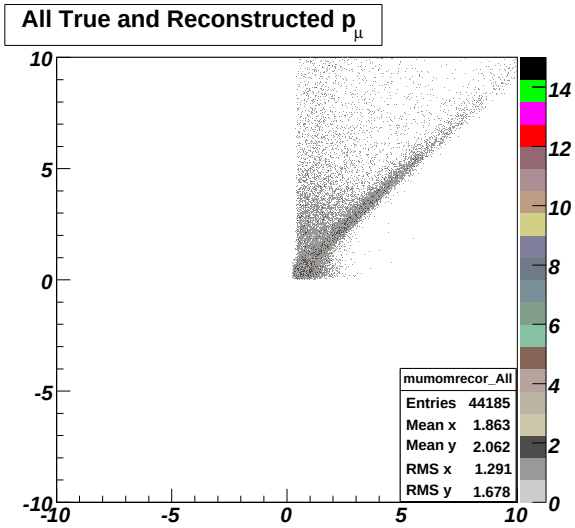

Figure B.1: $p_\mu(true)$ vs $p_\mu(range)$ for all true ν_μ events that interact via the CC interaction in the Far Detector.

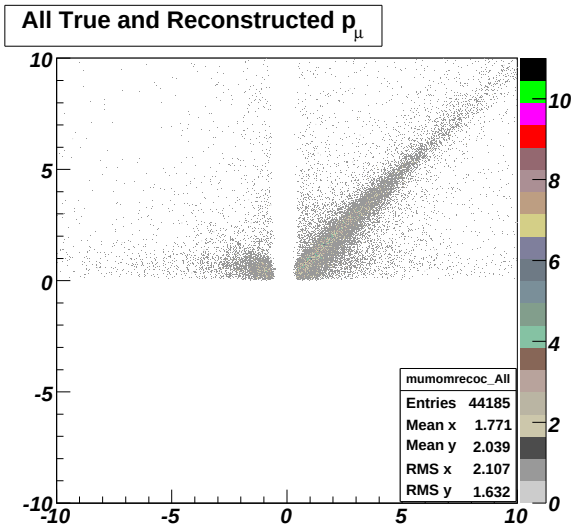

Figure B.2: $p_\mu(true)$ vs $p_\mu(curve)$ for all true ν_μ events that interact via the CC interaction. The negative momenta are from tracks with mis-reconstructed curvature, as if from a $\bar{\nu_\mu}$ in the Far Detector.

B.2 CC Event Separation in MINOS

A brief outline of the standard CC event separation in MINOS is described here. A detailed description is presented in Reference [32][37].

The technique is similar to that used for the QEL-like-event separation in Section 4.4. First three good quantities that distinguish CC from NC are identified. These are :

- Event length in planes : this identifies the muon, since the muon tracks are longer than the hadronic shower spans.
- Ratio of track pulse height to Event pulse height : again for an event with a muon track this ratio will be high
- Mean track pulse height (in GeV) per plane : this number is low for an event with a muon, but high for an event with hadron showers.

Then one-dimensional probability distribution functions are made for the above three quantities, for the CC and NC events separately, and a PID is defined as :

$$PID_{CC} = -(sqrt{-}ln(\prod_{i=1}^{3} p_{CC_i}) - sqrt{-}ln(\prod_{i=1}^{3} p_{NC_i})) \tag{B.1}$$

where, p_{CC_1}, for example is the probability that the event studied is CC like based on its event length in planes. This value is read off from the pdf of event length for the CC events.

All events with $PID_{CC} < -0.1$ and $PID_{CC} < -0.2$ are selected as CC-like events in the Near and Far Detectors respectively.

Appendix C

Oscillation Analysis Using Extended Fit

In the main text the oscillation analysis was performed by using only neutrinos of energy 0.5 GeV - 5.0 GeV. Here I will show the effects of using neutrinos of energy 0.5 GeV - 10.0 GeV for the mock data and the real data.

C.1 Mock Data Challenge

The same mock data sample that was analyzed in Chapter 5 was used, but all neutrinos with energies 0.5 GeV - 10.0 GeV were used. The predicted Far Detector unoscillated spectrum, together with the Far Detector mock data and the best fit line is shown in Figure C.1. This gave a $\frac{\chi^2_{min}}{ndof} = \frac{53}{(95-2)}$ for 95 bins of 0.1 GeV energy in the two dimensional parameter space. The χ^2 contours for the 68.27% (1σ), 95.45%(2σ) and 99.73%(3σ) confidence levels, together with the actual Δm^2_{23}, $\sin^2 2\theta_{23}$ value with which the Far Detector mock data was created is shown in Figure C.2. The minimum χ^2 is obtained for (Δm^2_{23}, $\sin^2 2\theta_{23}$) = ($0.0025\ eV^2, 0.88$). The actual values of (Δm^2_{23}, $\sin^2 2\theta_{23}$) were ($0.0024\ eV^2, 0.93$). As can be seen from

Figure C.2, the results still lie within 2σ (i.e., 95.45% confidence level) from the actual. In comparison with Figure 5.10, the size of the contours are not signifcantly altered.

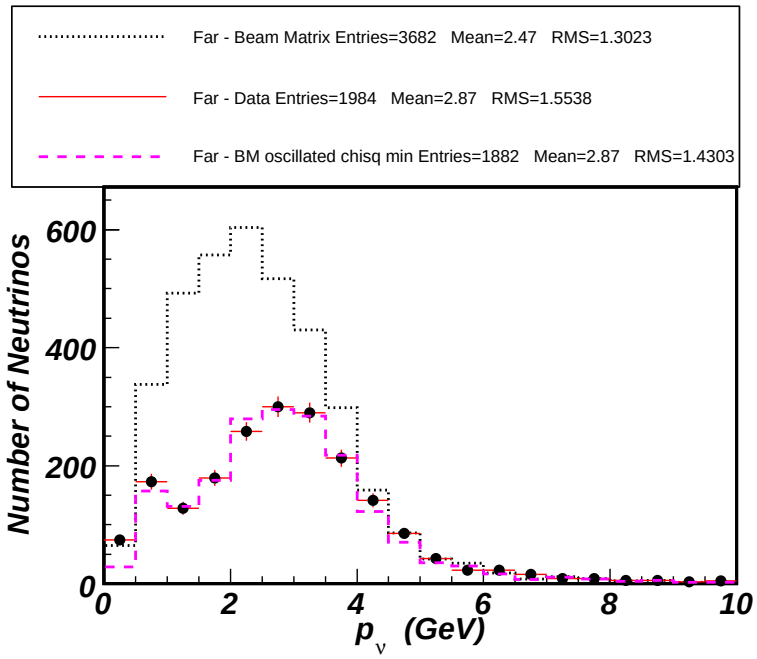

Figure C.1: The Far Detector mock data spectrum (black data points), the Far Detector predicted unoscillated spectrum (black dotted line) and the best fit for the data(pink dashed line).

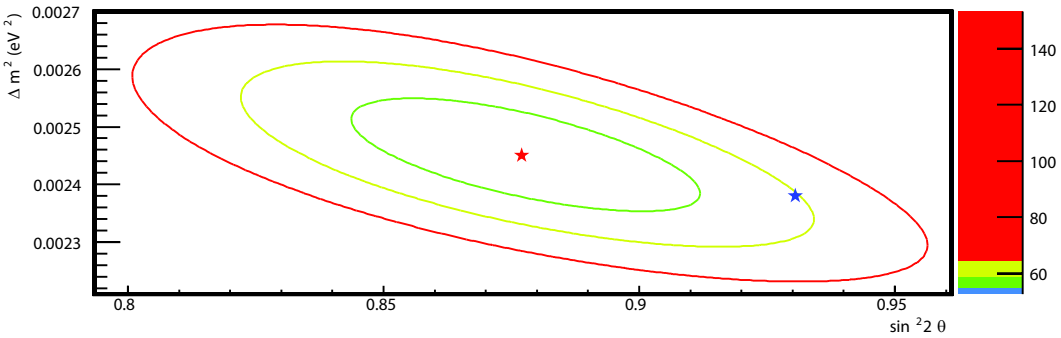

Figure C.2: The minimum χ^2 point of $(\Delta m^2_{23}, \sin^2 2\theta_{23}) = (0.0025\ eV^2, 0.88)$ shown as the red star.The three contours correspond to the 68.27% (green), 95.45% (yellow) and 99.73% (red) confidence levels for two degrees of freedom. [28]. The actual point with which the Far Detector mock data was generated is the blue star.

C.2 Real Data

The same real data sample that was analyzed in Chapter 6 was used, but all neutrinos with energies 0.5 GeV - 10.0 GeV were used. The predicted Far Detector unoscillated spectrum, together with the Far Detector mock data and the best fit line is shown in Figure C.3. This gave a $\frac{\chi^2_{min}}{ndof} = \frac{16}{(19-2)}$ for 19 bins of 0.5 GeV energy in the two dimensional parameter space. The χ^2 contour for the 90% confidence level is shown in Figure C.4. The minimum χ^2 is obtained for $(\Delta m^2_{23}, \sin^2 2\theta_{23}) = (0.0031\ eV^2, 0.92)$. In comparison with Figure 7.2, the size of the contour is not significantly altered, even though the best fit point is shifted.

This extended fit gives $\Delta m^2_{23} = 3.09^{+0.52}_{-0.51}(stat) \times 10^{-3}\ eV^2$ and $\sin^2 2\theta_{23} = 0.924_{-0.187}(stat)$ for 68.27% confidence level (1σ).

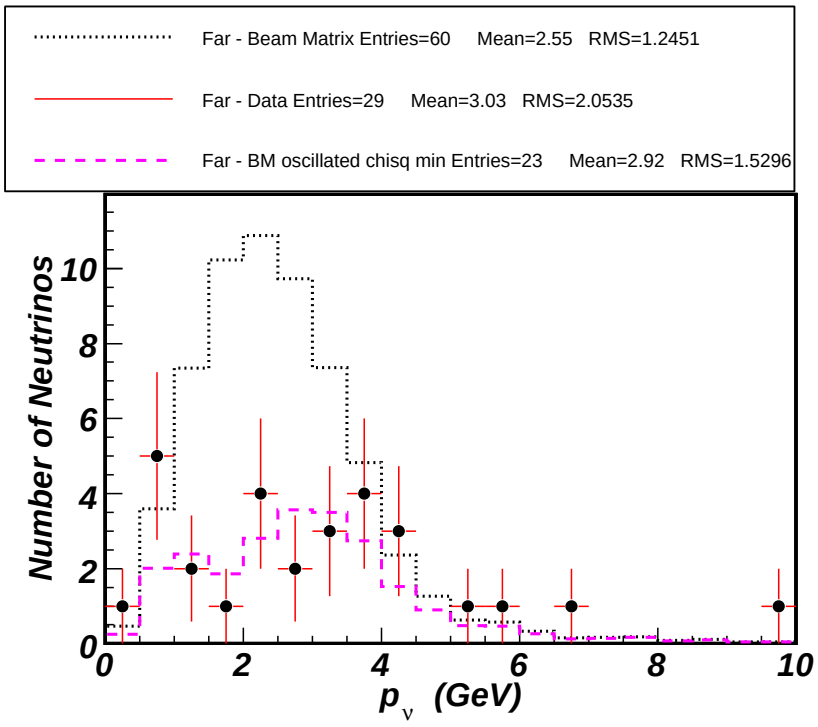

Figure C.3: The Far Detector mock data spectrum (black data points), the Far Detector predicted unoscillated spectrum (black dotted line) and the best fit for the data(pink dashed line).

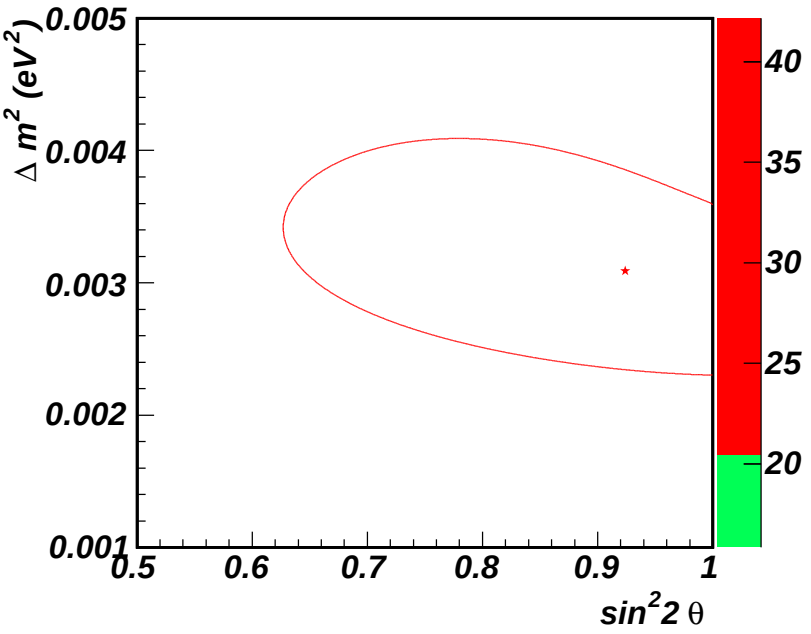

Figure C.4: The minimum χ^2 point of $(\Delta m^2_{23}, \sin^2 2\theta_{23}) = (0.0031\ eV^2, 0.92)$ shown as the red star.The contour corresponding to the 90% confidence level for two degrees of freedom. [28].

Bibliography

[1] J. Chadwick, Verh. der Deutschen Physikalischen Ges. **16**, 383 (1914)

[2] E. Fermi E Z.Phys. **88**, 161 (1934)

[3] C.L. Cowan, F. Reines et al, Science **124**, 3212 (1956)

[4] G.S. Abrams et al., Phys. Rev. Lett. **63**, 2173 (1989)

[5] G. Danby et al, Phys. Rev. Lett. **9**, 36 (1962)

[6] Donut Collaboration, Phys. Lett. **B504**, 218 (2001)

[7] R. Davis Jr., Experimental Phys. Rev. Lett. **13**, 303 (1964)

[8] B. Pontecorvo, Chalk River Laboratory Report **PD**, 2055 (1946)

[9] L.B. Okun, M.B. Voloshin, M.I. Vysotskii, Sov. Phys. JETP **64**, 3 (1986)

[10] B. Pontecorvo, J. Exptl. Theoret. Phys. **34**, 247 (1958)

[11] Z. Maki, M. Nakagawa, S. Sakata, Prog. Theor. Phys. **28**, 870 (1962)

[12] SNO Collaboration, Phys. Rev. Lett. **89**, 011301 (2002)

[13] SNO Collaboration, Phys. Rev. Lett. **89**, 011301 (2002)

[14] Super-Kamiokande Collaboration, Phys. Rev. Lett. **86**, 5651 (2001)

[15] Soudan 2 Collaboration, Physics Letters B **449**, 137 (1999)

[16] Y. Fukuda et al. (Super-Kamiokande), Phys. Lett. B **335**, 237 (1994)

[17] D. Casper et al. (IMB Collaboration), Phys. Rev. Lett. **66**, 2561 (1991).

[18] Super-Kamiokande Collaboration, Phys. Rev. Lett. **81**, 1562 (1998)

[19] Super-Kamiokande Collaboration, Phys. Rev. Lett. **93**, 101801 (2004)

[20] Walter, C.W. et al. (Super K Collaboartion), Nuclear Instruments and Methods in Physics Research Section A: Accelerators, Spectrometers, Detectors and Associated Equipment, **503**, 110 (2003)

[21] Super-Kamiokande Collaboration, Phys. Rev. D. **71**, 112005 (2005)

[22] Super-Kamiokande Collaboration, Phys. Rev. Lett. **85**, 3999 (2000)

[23] CHOOZ Collaboration, Phys. Lett. B **466**, 415 (1999)

[24] NOMAD Collaboration, CERN-PPE, **97**, 059 (1997)

[25] MINOS Collaboration, MINOS Technical Design Report, (1998)

[26] D. Petyt, NuMI Note 1680 (2006)

[27] MINOS Collaboration The MINOS Detectors preprint submitted to Elsevier Science, (2006)

[28] Particle Data Group, Physics Letters B, **592**, (2004)

[29] B.C. Choudhary, L. Mualem, NuMI Note L-589, (2000)

[30] K. Ruddick, NuMI Note L-313, (1997)

[31] A. Bodek, J.L. Ritchie, Physical Reveiw D., **23**, 5 (1981)

[32] D.G. Michael et. al. (MINOS), Phys. Rev. Lett., **97**, 191801 (2006)

[33] B. Rossi, High Energy Particles, Prentice-Hall, Inc. (1952)

[34] M. Szleper, A. Para, NuMI-B-781, (2001)

[35] Y. Ashie et. al., Phys. Rev. D **71**, 112005 (2005)

[36] C. Andreopoulos et. al., NuMI Note 2989, (2007)

[37] MINOS Collaboration, arXiv:0711, (2007)